Self-organized Pattern Formation using Engineered Bacteria

by

Stephen Payne

Department of Biomedical Engineering
Duke University

Date:_____

Approved:

_____
Lingchong You, Supervisor

_____
Nicolas Buchler

_____
Gabriel Lopez

_____
David Schaeffer

_____
Fan Yuan

Dissertation submitted in partial fulfillment of
the requirements for the degree of Doctor
of Philosophy in the Department of
Biomedical Engineering in the Graduate School
of Duke University

2013

ABSTRACT

Self-organized Pattern Formation using Engineered Bacteria

by

Stephen Payne

Department of Biomedical Engineering
Duke University

Date:_____

Approved:

_____
Lingchong You, Supervisor

_____
Nicolas Buchler

_____
Gabriel Lopez

_____
David Schaeffer

_____
Fan Yuan

An abstract of a dissertation submitted in partial fulfillment of the requirements for the degree of Doctor of Philosophy in the Department of Biomedical Engineering in the Graduate School of Duke University

2013

Abstract

Diverse mechanisms have been proposed to explain natural pattern formation processes, such as slime mold aggregation, feather branching, and tissue stratification. Regardless of the specific molecular interactions, the vast majority of these mechanisms invoke morphogen gradients, which are either predefined or generated as part of the patterning processes. However, using *E. coli* programmed by a simple synthetic gene circuit, I demonstrate here the generation of robust, self-organized ring patterns of gene expression in the absence of an apparent morphogen gradient. Interestingly, modeling and experimental tests show that the temporal dynamics of the global morphogen concentration serve as a timing mechanism to trigger formation and maintenance of these ring patterns, which are readily tunable by experimentally controllable environmental factors. This mechanism represents a novel mode of pattern formation that has implications for understanding natural developmental processes. In addition, the system can be coupled with inkjet printing technology and metabolic engineering approaches to develop future complex patterned biomaterials.

Dedication

To my friends and family who were there through the good times and the bad.

Contents

List of Tables

List of Figures

Figure 39: 3-Dimensional (3D) confocal image of a typical base-case mCherry pattern. a) Tilted (top) and side (bottom) views of a 3D reconstruction of the mCherry pattern based on a series of z-slice images 5.21 μm in depth spanning x- and y-dimensions of length 1214 μm taken by a Zeiss LSM 780 upright confocal microscope. The pattern was excited at a 561 nm wavelength, and the emission filter used collected wavelengths between 576 and 696 nm. The pattern was obtained for the base-case condition described in Figure 35. The 3D reconstruction was done using MetaMorph. b) Raw 1.7 mm X 1.4 mm composite fluorescent image of the pattern displayed in a). The color scheme is as described in Figure 30. c) Heat map displaying mCherry intensity in both the vertical (y-axis) and radial (x-axis) directions as derived from the confocal microscope image reconstructed in a). The radial intensity values are the average intensity values across angles spanning $3\pi/4$ to $7\pi/4$. Processing was carried out using a custom MATLAB code..... 119

Figure 40: Simulated and measured modulation of pattern formation by environmental factors. a) Modulation of patterns by perturbing AHL temporal dynamics. The base case occurs when a single pulse of AHL exceeds a threshold necessary to trigger ring formation (left, e.g., as in Figure 34 and Figure 37). Adding exogenous AHL allows AHL to exceed the threshold concentration faster, leading to the formation of a smaller ring (center). Increasing the domain size slows down AHL accumulation due to increased spatial dilution, leading to the formation of a larger ring (right). b) Simulated dependence of ring radius on initial, exogenously added AHL concentration. Average mCherry ring radii obtained at 25 hours and 13.3 hours for 1D simulations of microcolonies growing from initial AHL concentrations of 0-1200 molecules per Δ and 1500-4000 molecules per Δ. For each replicate, the time chosen for data analysis corresponds to the time at which only the first mCherry ring radius has emerged. All of the mCherry ring radii were calculated in the same manner as described in Figure 34. The error bars represent standard error among ten replicates. The black curve indicates a best-fit Hill function calculated using a custom MATLAB code. c) Measured dependence of ring radius on initial, exogenously added AHL concentration. Average mCherry ring radii obtained for microcolonies growing from an initial AHL concentration of 0, 10, 30, and 100 nM AHL, respectively. These values were obtained from replicates at 24-hour time points for 10, 30, and 100 nM AHL and from replicates at 36-hour time points for 0 nM AHL (no mCherry rings emerged for this condition at the 24-hour time point). All of the mCherry ring radii were calculated in the same manner as described in Figure 34. The error bars for 0, 10, 30 and 100 nM AHL represent standard error among 7, 10, 9, and 5 replicates, respectively. Cropped representative mCherry images to scale of microcolonies growing in the absence (top middle panel) or presence (bottom right panel) of an initial AHL concentration of 100 nM at 24-hour and 36-hour time points, respectively, are shown. The color scheme is defined as in Figure 34. d) Simulated

Acknowledgements

I would like to acknowledge my advisor, L. You, as well as my coauthors, M. Gray, B. Li, M. Ryser, D. Schaeffer, R. Smith, H Song, and C. Tan. I also would like to acknowledge W. Cao for her work with me on inkjet printing and K. Marusak and S. Zauscher for their work with me on bacterial synthesis of CdS. I thank J. Wong, A. Pai, J. Tabor, C. Tan, Y. Tanouchi, and You lab members for discussions or comments; Duke IGSP's DSCR for assistance with high-performance computations; B. Munsky, J. Ozaki, H. Song, and M. Wall for preliminary analysis on earlier versions of the mathematical model; K. Gonzales for discussions on the modeling framework; Y. Gao and S. Johnson for assistance with confocal microscopy; Duke Light Microscopy Core Facility (LMCF) for access to confocal microscopes and imaging software; M. Elowitz for strain MC4100Z1; F. Yuan for access to a Kodak fluorescence image station and software (Comsol Multiphysics); F. Arnold, C. Collins, and J. Keasling for sharing genetic constructs; B. Munsky, M. Wall, K. Ganguly, B. Marrone, and the National Flow Cytometry Resource (NFCR) for their assistance in my work at Los Alamos National Laboratory (LANL); Duke SMIF's assistance with TEM; and N. Buchler, G. Lopez, D. Schaeffer, and F. Yuan for their contributions as advisors on my graduate committee. Finally, I would like to thank my family, friends, and all You lab members, especially "Painouchi" and J. Wong, for their moral encouragement through the tough times.

My studies were partially supported by Office of Naval Research (N00014-12-1-0631), National Institutes of Health (LY: 1R01-GM098642, 5R01CA118486; MDR: R01-GM096190-02), a DuPont Young Professorship (LY), a National Science Foundation CAREER award (LY), a David and Lucile Packard Fellowship (LY), a Duke University Pratt Fellowship for undergraduate research (to MG), an NIH/NIGMS Biotechnology Predoctoral CBTE Fellowship (to SP), and a DHS Graduate Fellowship (to SP). The research was performed under an appointment to the Department of Homeland Security (DHS) Scholarship and Fellowship Program, administered by the Oak Ridge Institute for Science and Education (ORISE) through an interagency agreement between the US Department of Energy (DOE) and DHS. ORISE is managed by Oak Ridge Associated Universities (ORAU) under DOE contract number DE-AC05-06OR23100. All opinions expressed in this paper are the author's and do not necessarily reflect the policies and views of DHS, DOE, or ORAU/ORISE.

1. Engineering cell-cell communication and its applications

Over the past several decades, biologists have become more appreciative of the fundamental role of intercellular communication in natural systems spanning prokaryotic biofilms to eukaryotic developmental systems and neurological networks. From an engineering perspective, the use of cell-cell communication provides an opportunity to engineer more complex and robust functions using cellular components. Indeed, this strategy has been adopted in synthetic biology in the creation of diverse gene circuits that program spatiotemporal dynamics in one or multiple populations. Gene circuits, such as these, may offer insights regarding basic biological questions and motifs or serve as a basis for novel applications. The contents of this chapter have been submitted for publication: Payne S, You L. "Engineered cell-cell communication and its applications." *Productive Biofilms*. Ed. K Muffler and R Ulber. *Advances in Biochemical Engineering/Biotechnology*. Manuscript submitted February 10, 2013.

1.1 Introduction

One of the most defining achievements throughout evolutionary history was the advent of the ability of cells to communicate with one another. The obvious importance of this breakthrough was the ability of multicellular organisms to arise, with cells coordinating with one another to better survive in their respective environments [1]. Cell-cell communication then allowed for certain cells to become specialized, thus

allowing for a division of labor within a multicellular organism [2]. Eventually, this specialization gave rise to different systems (i.e. respiratory, nervous, etc.), each with their own sophisticated cell-cell communication networks [3].

Until recently, most prokaryotic organisms were thought to exist alone as individuals. However, studies over the past four decades have increasingly recognized the importance of cell-cell communication among these species. This communication is responsible for coordinating integral population-level behaviors, including biofilm formation, competence development, expression of virulence factors, sporulation, and production of bioluminescence [4]. Each of these behaviors is inefficient when only a small number of cells are present, yet can be beneficial on the population level [4]. Therefore, cell-cell communication is not only integral to the proper functioning of multicellular organisms but also to unicellular organisms, which often perish or prosper as part of a larger population.

In synthetic biology, cell-cell communication has also been recognized as an effective strategy to achieve robust system dynamics in engineered cell populations. This recognition has led to a gradual shift from a cell-centric perspective to a population-centric perspective. In early work in the synthetic biology field, devices, such as switches, oscillators, timers, and logic gates, were mostly constructed to operate at the single-cell level [5-8]. Recently, increasing emphasis has been placed on the use of cell-cell communication modules to coordinate population-level behavior in synthetic

biological systems [9-13]. There are two reasons for this shift from unicellular to multicellular programming. First, because of the broad-ranging importance of cell-cell communication in diverse natural biological systems, synthetic biologists can use engineered, communication-based systems to explore basic biological questions. By bypassing natural systems, which are often confounded with interconnected gene networks, complex environmental interactions, and interspecies relationships, engineered systems may serve as better defined models to address certain biological questions regarding ecosystem interactions, evolutionary processes, and pattern formation. Second, programming cellular behavior on a population-level can be more robust and efficient from an engineering perspective. To this end, the use of cell-cell communication may be critical in generating systems for robust pattern formation, biocomputing, and bioprocessing.

In this chapter, I will first discuss a predominant method of cell-cell communication, quorum sensing (QS), which is the basis for numerous communication modules utilized in the field of synthetic biology. I will then discuss recent synthetic-biology studies that use engineered, communication-based circuits to address basic biological questions. This will lead into a description of recent advances in engineering robust biological devices using cell-cell communication. Finally, I will discuss examples of novel engineered cell-cell communication modules, which may be the basis for future synthetic biological systems.

1.2 Quorum Sensing

QS has been identified in a large variety of both gram-positive and gram-negative bacteria [14-16]. In a QS system, bacteria synthesize a chemical signal that diffuses inside and outside of the cell. As a bacterial population grows, the concentration of signal in the environment increases as more bacteria contribute to the synthesis of the chemical signal. At a sufficiently high bacterial density, or when the population reaches a "quorum," the signal concentration reaches a threshold necessary to activate a signal cascade, leading to downstream gene expression. Fundamental to this process is that the threshold concentration is reached at the same time for all cells within a local population, and thus, activation of downstream gene expression is coordinated across that local population (Figure 1a).

A canonical QS system is the LuxR/LuxI system from *V. fischeri* [17]. In this system, LuxI synthesizes a small molecule acyl-homoserine lactone (AHL), which acts as the diffusible signal discussed above. At a sufficiently high cell density, intracellular AHL can reach a high enough concentration, such that it binds to and activates the LuxR protein, which in turn activates downstream genes [17]. Many LuxR/LuxI-type QS systems have been identified in numerous bacterial species; they control highly diverse biological functions, such as bioluminescence, biofilm formation, and virulence development [17].

1.3 Using engineered cell-cell communication to understand natural biological phenomena

Although most synthetic biological systems have been implemented as novel engineered devices, they have also been used to explore basic biological questions. Here, I focus on two major subjects explored using synthetic, communication-based systems: ecology and evolution.

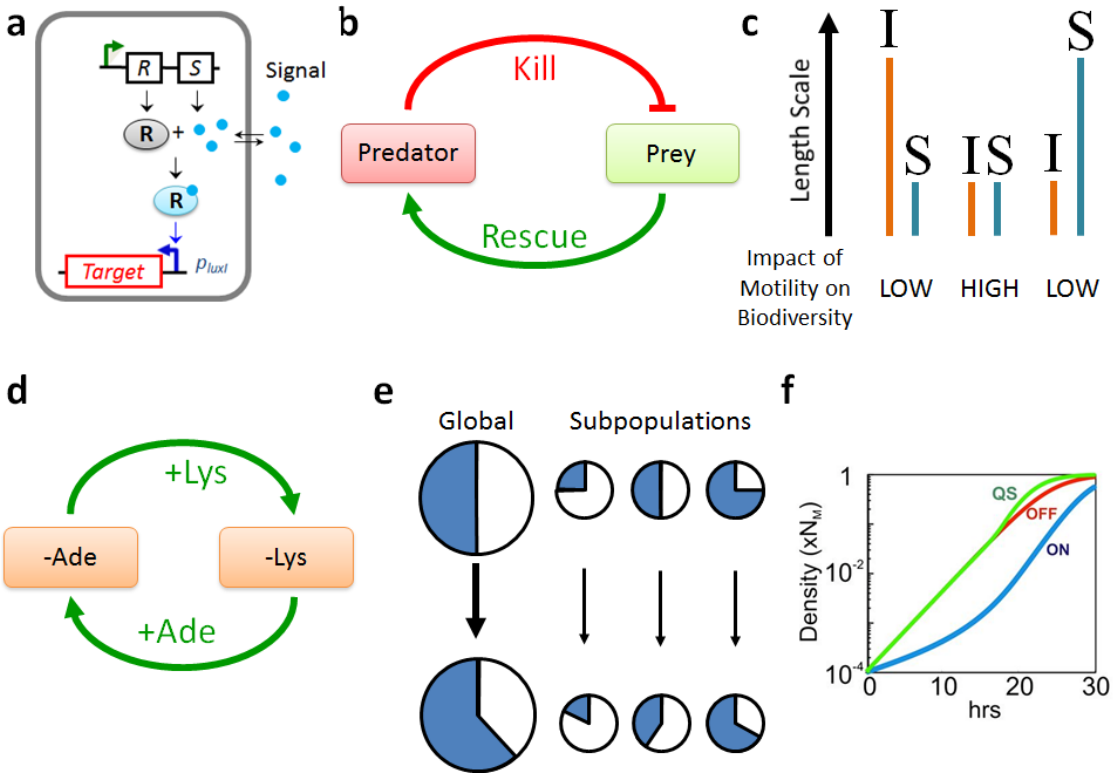

Figure 1: a) Diagram of a generic QS system. A receptor gene (R) and a synthase gene (S) encode proteins R and S. Protein R is a receptor protein, which becomes activated upon binding the QS signal. The QS signal is synthesized by protein S (a synthase). Only when enough signal has accumulated in culture is enough R protein bound to the QS signal to sufficiently activate the QS-regulated (blue) promoter. When induced, this promoter activates transcription of a downstream target gene. b) Logic of the synthetic predator-prey system. The predator kills the prey by inducing the toxin protein CcdB in the prey via the QS signal 3OC12HSL. The prey rescues the predator by inducing the antitoxin protein CcdA via the QS signal 3OC6HSL. CcdA rescues

the predator from constitutively expressed CcdB. c) The interaction and segregation length scales determine the impact of cell motility on biodiversity in the predator-prey system. If the length scale of the interaction (QS signaling) between predator and prey is large relative to the segregation distance (left) or vice versa (right), the impact of cell motility on biodiversity is low. However, if the length scales of the interaction and the segregation distance are comparable, the impact of cell motility on biodiversity is high (center). d) Logic of the synthetic mutualism system. One strain lacks the ability to produce adenine but overproduces lysine (left), while the other lacks the ability to produce lysine but overproduces adenine (right). The populations survive best in co-culture, thus mimicking a mutualistic relationship. e) Simpson's Paradox. This phenomenon occurs when the proportion of producers (blue fraction) in the global population increases (left), while the proportion of producers decreases in each of the subpopulations (right). Chuang et al. were able to implement such a scenario in a synthetic, QS-based system and quantitatively characterize this evolutionary phenomenon. f) QS as a strategy for optimizing population growth. Pai et al. constructed a system whereby public goods were secreted throughout a population. Production and secretion of the public goods incurred a metabolic cost to producer cells. For certain conditions, QS-regulated production of public goods (green curve) was found to be the best growth strategy when compared to constitutive (blue curve) and no (red curve) production.

1.3.1 Ecology

Ecologists have long been interested in the dynamics of predator-prey relationships. Balagadde et al. engineered a predator-prey gene circuit, which allows for two-way communication between two strains of *E. coli* [18]. As shown in Figure 1b, the system consists of a predator strain and a prey strain. Upon circuit induction, the predator expresses LasI, which synthesizes an AHL, 3OC12HSL; the prey expresses LuxI, which synthesizes another AHL, 3OC6HSL. Each strain produces the appropriate receptor protein (LasR and LuxR) corresponding to the AHL secreted from the other. 3OC12HSL from the predator induces downstream expression of a toxin protein, CcdB, in the prey, thereby killing it. 3OC6HSL from the prey induces downstream expression

of an antitoxin protein, CcdA, in the predator, which rescues it from constitutively expressed CcdB [18]. Therefore, the prey is killed by the predator, and the predator is rescued by the prey (Figure 1b), thus implementing the basic logic of the prototypical predator-prey relationship.

By studying the system in a microfluidic device, Balagadde et al. demonstrated complex predator-prey dynamics, including extinction, coexistence, and oscillations. Guided by modeling, the authors also examined how these dynamics would respond to experimental perturbations to specific system parameters [18]. Song et al. extended this study and used the engineered ecosystem as a model to examine the factors affecting biodiversity (as measured by relative abundance) in a solid-phase environment (see Chapter 2 for more details). The authors found that biodiversity will be sensitive to changes in cell motility if the segregation distance between the two populations is comparable to the length scale of AHL diffusion. In such a case, biodiversity is inversely correlated with cell motility. If the AHL diffusion length scale is much greater than the segregation distance or vice versa, changes in cell motility do not significantly influence the system's biodiversity (Figure 1c) [19]. In both studies, the system represented a simple, well-defined, yet non-trivial model system by which investigators could confine their analyses of the predator-prey interaction to a few well-defined parameters, bypassing natural systems that are confounded by other species interactions, environmental variation, etc. This approach allowed the authors to ask specific

questions regarding the nature of a basic predator-prey relationship and answer those questions by precise experimentation guided by mathematical modeling.

In this manner, Shou et al. examined the dynamics of a synthetic ecosystem in which two strains of *S. cerevisiae* mimic a mutualistic relationship through the cooperative production of two essential metabolites (lysine and adenine). One strain overproduces lysine and lacks the gene necessary to produce adenine, while the other strain overproduces adenine and lacks the gene necessary to produce lysine (Figure 1d). Both strains in monoculture will die because they lack either adenine or lysine. When grown in co-culture, however, the strains can grow well because each strain supplies the other with a missing essential metabolite. By combining modeling with an experimental approach, the investigators demonstrated that the total initial cell number and the initial ratio between the two strains were critical determinants of viability in the system [20].

Using a similar strategy, Hu et al. created a mutualistic system consisting of two engineered *E. coli* strains that use two-way QS communication systems to induce expression of antibiotic resistance genes in bacteria. They, too, were able to successfully model the key factors influencing the ability of the co-culture to survive under a variety of experimental conditions [21]. As with the previous study, this system was used to identify the driving forces of different dynamical behaviors possible in a mutualistic system.

Similar to the synthetic predator-prey system, the spatial population structure has been found to be an important determinant influencing the dynamics of engineered mutualistic ecosystems. By studying a synthetic community of three different bacterial species in a microfluidic device, Kim et al. demonstrated that spatial barriers between the bacterial species is necessary and sufficient for stable coexistence of the populations [22]. Similarly, Brenner and Arnold illustrated this same concept within a biofilm formed by a synthetic consortium of two engineered *E. coli* strains that communicate via QS. In the biofilm, the two populations formed defined layered structures of population aggregates, which enhanced the consortium's ability to survive [23].

1.3.2 Evolution

Simpson's paradox is an apparently paradoxical phenomenon by which two subpopulations evolve in many segmented co-cultures. In these co-cultures, one subpopulation (the producers) produces a public good that benefits the entire population, while another subpopulation (the nonproducers) does not produce anything but reaps the benefits from the producers. Given the appropriate parameters, the proportion of producers in each segmented co-culture can decrease over time, while the overall proportion of producers in the total population can increase (Figure 1e).

To better understand this phenomenon, Chuang et al. built a system of two engineered *E. coli* strains, which both contain a gene encoding antibiotic resistance downstream of a promoter sensitive to QS signaling. One strain (the producer) expresses

the QS signal, while the other (the nonproducer) does not. Thus, the producer bears the metabolic burden of producing the QS signal, while the nonproducer does not; yet both strains benefit from the producers' QS signal, which allows them to resist the antibiotic in the medium [24]. Using this system, the investigators were able to observe Simpson's paradox in action. Furthermore, by studying this system in a well-controlled environment without conflicting interactions, they were able to quantitatively characterize the phenomenon with limited confounding factors.

A synthetic system has also been utilized to determine whether QS is an optimal strategy for regulating the production of public good exoproducts. Pai et al. recently constructed a gene circuit which produces a secreted form of beta-lactamase that confers resistance to 6-aminopenicillanic acid (6-APA) by degrading it in culture. The investigators studied the circuit under three conditions: (1) production of the exoproduct is regulated by the LuxR/LuxI QS module, (2) production is regulated by an inducible promoter, and (3) production does not occur. In this system, the production and secretion of the exoproduct incurs a metabolic cost to the host cell, but once secreted, the exoproduct benefits the entire population. Therefore, it serves as a public good. By quantitative analysis, the authors identified a set of conditions whereby QS regulation of the public good protein is the optimal strategy for maximizing cell growth (Figure 1f). The authors conclude that the kinetic properties of the QS systems can be tuned to optimize bacterial survival [25], which confirms an earlier theoretic prediction [26]. This

property may explain how QS systems can be utilized by bacteria to deal with stressful conditions (i.e., antibiotic exposure).

Waddington's landscape has long been used as an analogy for phenotypic diversification within a cell lineage. The analogy invokes the image of a marble rolling down a landscape with different local minima where the marble will come to rest. In this analogy, the cell is the marble, and the different low states that the marble can settle into represent different cell fates. This analogy is often invoked to visualize how stem cells can differentiate into various tissue types depending on both intracellular gene expression and external signaling [27]. Using a synthetic circuit consisting of a QS-driven toggle switch, Sekine et al. demonstrated how cells diversify autonomously through cell-cell communication. Through experimentation and stochastic modeling, the group was able to confirm the QS-mediated bifurcation of switching from one state to another and found that this switching was critically dependent on initial cell number. The work's importance lies in the fact that, although invoked in a variety of developmental systems, cells diversifying across Waddington's landscape had never been directly confirmed experimentally. Therefore, the group's synthetic system represents a direct demonstration of Waddington's landscape in action [27].

1.4 Applications of cell-cell communication in pattern formation

Synthetic pattern-forming systems, like synthetic cell-cell communication systems in general, serve a dual use. First, they reveal minimalistic strategies for

achieving specific natural biological processes. Second, they represent a new method of engineering structures solely using biological components. The importance of pattern formation in nature cannot be understated as it is ubiquitous throughout the biosphere, driving such varied biological processes as slime mold aggregation [28, 29], feather branching [30], and tissue stratification [31, 32]. By implementing pattern formation using synthetic gene circuits, investigators can extrapolate the key components necessary for pattern formation in natural systems (see Chapter 7). This exercise can provide insights as to how these processes occur in more complex systems. In addition, synthetic pattern-forming systems could become the basis of next-generation biomaterials (see Chapter 7 and Appendix B), which self-organize into precise patterns of biological entities (i.e., proteins, metabolites, etc.).

Basu et al. constructed the first synthetic pattern-forming system, which utilizes a population mixture of sender and receiver cells. Here, sender cells express LuxI, which synthesizes the AHL 3OC6HSL. Receiver cells express the receptor protein, LuxR. Upon binding 3OC6HSL from the sender cells, activated LuxR stimulates expression of a LacI mutant and cI, which inhibits expression of another LacI protein. LacI, in turn, inhibits GFP expression. Thus, the receiver cells contain a gene network constituting an incoherent feed-forward loop (Figure 2a), where too much or too little AHL results in repression of GFP expression. This lack of expression occurs at high AHL concentrations since the LacI mutant represses GFP expression, while expression is also blocked at low

AHL concentrations since there is not enough cI expressed to inhibit wild-type LacI from inhibiting GFP. Thus, the receiver cells constitute a band-detector, which only express GFP at intermediate AHL concentrations [33].

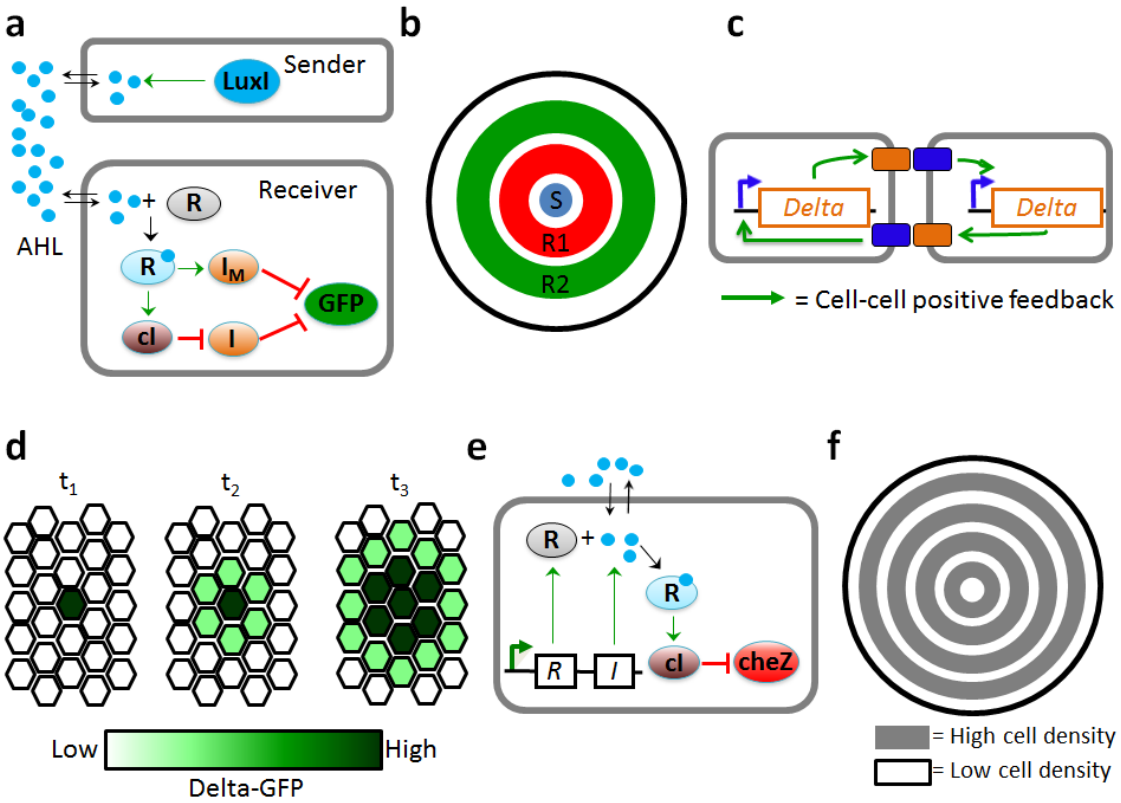

Figure 2: a) Circuit diagram for a synthetic sender-receiver system. A sender cell constitutively expresses LuxI, which synthesizes the AHL 3OC6HSL. Receiver cells express LuxR (R), which binds AHL and activates cI and a mutant LacI (I_M). cI inhibits another LacI (I). Both versions of LacI inhibit GFP. Thus, the receiver cell's gene network can be viewed as an incoherent feed-forward loop, where only mid-range concentrations of AHL activate high levels of GFP. b) Spatial patterns generated via the circuits in a). By constructing two versions of the receiver circuit in a) with varying sensitivities and different fluorescent proteins (red and green), a lawn of cells containing two receiver circuits (R1 and R2) can generate concentric circles about a small population of sender cells (S) at the center of an agar plate. c) Delta-Notch synthetic gene circuit. A Delta-GFP fusion protein is placed downstream of the Delta-Notch pathway. Upon cell-cell contact mediated by Delta-Notch, the gene circuits constitute a positive feedback loop. d) Circuit in c) generates signal propagation in a

field of cells. Cells containing the gene circuit are placed in a field surrounding a "trigger" cell (center dark green cell), which constitutively activates the Delta-Notch pathway. Activation of Delta-GFP is then propagated from the trigger cells to proximate cells and finally to distance cells over time. e) Synthetic circuit coupling cell density and motility. Activated LuxR induces expression of cI when a high cell density is detected. cI then inhibits cheZ, which in turn results in low cell motility. f) Alternating low and high cell density rings result in a field of expanding cells containing the circuit in e). The oscillatory nature of the circuit in e) gives rise to alternating ring patterns of low and high cell density.

On a plate containing an undifferentiated lawn of receiver cells surrounding sender cells placed at the center, the receiver cells only express GFP in ring patterns at intermediate radii about the center. This pattern formation occurs since cells expressing GFP experience intermediate AHL concentrations, while cells closer to the center experience higher AHL concentrations and cells towards the edge of the plate experience lower AHL concentrations. By combining receiver gene circuits with varying sensitivities to AHL and different fluorescent proteins, Basu et al. were able to obtain multiple concentric rings, which constituted bullseye patterns (Figure 2b). Furthermore, modifying the position(s) of the sender cells allowed the investigators to achieve more complex patterns. This system resembles the circuit underlying *D. melanogaster* blastoderm segmentation and can lead to the deduction of design principles in natural pattern-forming systems [33].

Another interesting synthetic system implementing pattern formation involves direct cell-cell interactions between mammalian cells using the Delta-Notch signaling pathway [34]. Instead of using QS, this system utilizes contact-based interactions

mediated by surface proteins. Specifically, a gene encoding a Delta-GFP fusion protein is placed downstream of the Delta-Notch signaling pathway. The Delta-Notch signaling pathway is activated when a cell surface makes physical contact with another cell expressing Delta-Notch on the surface. In this manner, an effective positive-feedback loop driving Delta-GFP fusion protein expression operates when a cell comes into close physical contact with other cells in a field (Figure 2c). When these engineered cells are placed around cells constitutively expressing Delta ("trigger" cells), the system leads to signal propagation of GFP reporter expression in the spatial domain (Figure 2d). The investigators in the study speculate that the system could be used to investigate the mechanistic bases for pattern formation in various mammalian developmental systems. Furthermore, such a system could be used to control differentiation pathways for tissue engineering applications [34].

However, a limitation of this mammalian system and Basu et al.'s system is that the patterns are determined by a pre-defined location that the trigger or sender cells occupy. This leads us to an important biological question that scientists have been pondering since Alan Turing first examined it in the 1950s [35]: How can biological patterns self-organize without any predetermined spatial configuration or external stimulus? Liu et al. addressed this question with their own synthetic circuit that programs self-organized pattern formation by regulating cell motility using the LuxR/LuxI QS module (Figure 2e). At high cell densities, the QS module triggers

expression of cI, which inhibits CheZ expression. Repression of CheZ reduces cell motility. When placed on a soft agar plate, cells containing this circuit grew outward from a small initial population at the center and formed concentric rings of alternating high and low densities (Figure 2f) [36]. This pattern was the direct result of an oscillatory dynamic between high and low population states being translated spatially in the radial direction. Interestingly, the synthetic system demonstrates how a spatially periodic pattern can be generated without an external clock, which is thought to be necessary in vertebrate development [36]. In addition, the system has potential for engineering spatially periodic biomaterials.

Another method for generating precise patterns is to combine synthetic gene networks with inkjet printing technology. Inkjet printing technology has been used in several previous studies to precisely print bacterial and mammalian cells onto surfaces at high resolution [37-39]. In addition, Choi et al. recently applied this technology to engineered *E. coli* cells containing synthetic QS components. Briefly, the investigators examined the spatiotemporal dynamics of precisely printed microcolonies of cells producing AHL (senders), cells expressing GFP in response to AHL (receivers), and cells that inhibit GFP expression in response to AHL (inverse receivers). Interestingly, neighboring microcolonies placed in large arrays communicated with one another efficiently, giving rise to synchronization of microcolonies within local spatial regions. Experiments indicated that this communication between cells could be tuned effectively

with this framework by changing microcolony size, spacing distance, printing timing, and cell seeding number [40]. Thus, the system offers a high-throughput platform for analyzing cell-cell communication quantitatively. In addition, the precision of inkjet printing coupled with cell-cell communication could lead to a future generation of high-resolution spatial patterns (see Chapter 7 and Appendix A).

1.5 Applications of cell-cell communication in biocomputation and bioengineering

Cell-cell communication modules have also been adopted to construct biological systems, which perform computations or represent novel engineering feats. In biocomputing, scientists have long marveled at cells' capacities for informational storage and rapid processing. Likewise, many attributes of biological components (a wide array of functions, the potential for adaptability and modularity, etc.) make synthetic biological systems attractive to engineers. For these reasons, there have been several recent advances in the areas of biocomputing and bioengineering using synthetic systems that contain cell-cell communication modules.

1.5.1 Biocomputation

Logic gates are fundamental components of modern computers, which have been utilized by computer scientists and electrical engineers for many decades. Thus, it is not surprising that synthetic biologists hoping to make cells compute have primarily concentrated on developing diverse biological logic gates. A large amount of progress in this area has occurred over the last several years, culminating in recent studies in which

many logic gates have been integrated to achieve complex computational functions [41-44].

Many of these logic gates have utilized QS systems to synchronize logic signals across a cell population. For example, Brenner et al. developed a system in which two co-localized *E. coli* populations could converse with each other bidirectionally using two interlocked QS systems, the RhlR/RhlI and the LasR/LasI systems. Briefly, one cell population produces the RhlI signal, C4HSL, while the other population produces the LasI signal, 3OC12HSL. Each population only reads the QS signal from the other population by expressing the corresponding receptor protein. Once the complex between the receptor protein and the diffused QS signal (3OC12HSL or C4HSL) forms, it activates the promoter driving production of the other QS signal (C4HSL or 3OC12HSL, respectively), along with a GFP reporter. Thus, the two populations constitute a logical AND gate in which GFP activation only occurs when both QS signals are present. The authors demonstrate that the AND gate is indeed activated when the populations are spatially co-localized in agar and in a biofilm consortium [45].

AND gates can also be utilized to perform complex biocomputing tasks. Tabor et al. accomplished such a task by executing a synthetic genetic edge detection program using a logical AND gate. The goal of the project was to shine a projected image onto a field of engineered *E. coli* cells and to have the *E. coli* release a black pigment at the boundaries where light and dark regions meet (the edges of the image). This task was

accomplished using an engineered device, consisting of a dark sensor, an AND gate, a NOT gate, and a black pigment producer [41].

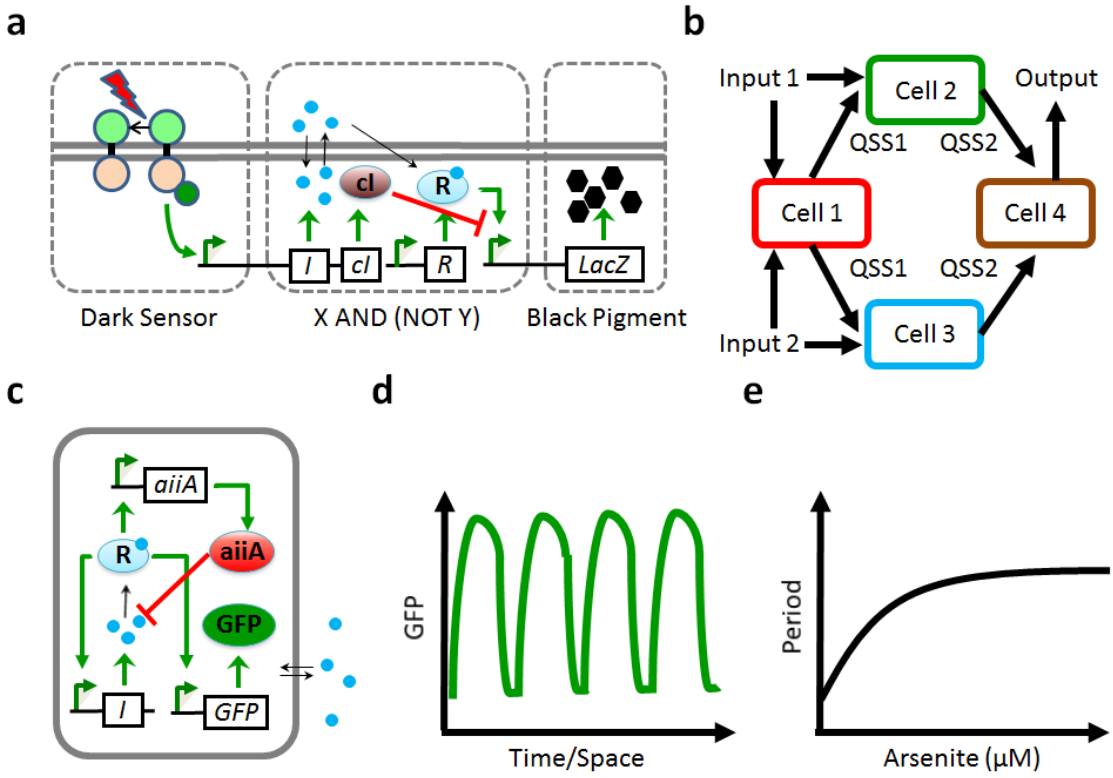

Figure 3: a) Synthetic genetic edge detector. In the absence of light, a light-sensitive surface protein is phosphorylated and activates a promoter via a signal transduction pathway (dark sensor). This promoter drives the expression of LuxI (I) and cI. When enough AHL is synthesized in the vicinity, enough activated LuxR can induce the $P_{lux-\lambda}$ promoter. Conversely, if enough cI is translated, it will repress the $P_{lux-\lambda}$ promoter. This part of the gene network constitutes an X AND (NOT Y) logic gate. The $P_{lux-\lambda}$ promoter then activates LacZ, which gives rise to a black pigment. The logic of the gene circuit dictates that black pigment will only be produced at the edges of a projected image, where cells are exposed to enough light such that cI levels are low and enough AHL from neighboring dark cells. b) QS systems as virtual wires linking logic gates. By growing isolated cell colonies containing single logic gates in a particular spatial configuration, complex computational functions can be carried out by linking colonies in close proximity via QS. For example, by adding two inputs (typically diffusible chemicals) to one side of a plate, one cell processor can connect with two other cell processors in parallel via a QS system. Then, these two cell

processors can connect to a final cell processor in parallel via a second QS system. The final cell processor can then generate an output in the form of expression of a fluorescent protein. c) Synthetic gene circuit with interlocking positive- and negative-feedback loops. Genes encoding LuxI, AiiA, and yemGFP are all downstream of the P_{luxI} promoter, which is activated by LuxR-AHL complex. LuxR is expressed constitutively. AiiA is an enzyme, which degrades intracellular AHL. Self-activation of LuxI constitutes a positive-feedback loop, while inhibition via AiiA constitutes an interlocking negative-feedback loop. d) Synchronized oscillations arise from the circuit in c). The architecture of the circuit in c) can synchronize oscillations of GFP signal throughout a population harboring it in both the temporal and spatial domains. For a constant cell density in a microfluidic device, bulk fluorescence oscillations are observed over time. In addition, traveling waves emerge for growing colonies and densely packed monolayers. e) Modified version of the circuit in c) can detect different arsenite concentrations. By further synchronizing the gene circuit in c) through gaseous H_2O_2 signaling and by putting LuxI downstream of an arsenite detecting pathway, Prindle et al. were able to detect statistically significant changes in oscillation period in response to varying arsenite concentrations.

Briefly, the dark sensor is a modified version of a previously characterized switch [46], which contains a surface protein that activates a signaling cascade in the engineered bacteria when light is not present. When activated in the dark, this switch induces expression of LuxI, which produces the AHL 3OC6HSL, and cI. 3OC6HSL binds to and activates LuxR, which in turn activates a $P_{lux\text{-}\lambda}$ promoter. Meanwhile, the $P_{lux\text{-}\lambda}$ promoter is also repressed by cI. When the $P_{lux\text{-}\lambda}$ promoter is activated, it triggers expression of β-galactosidase (the protein encoded by LacZ), which mediates production of a black pigment (Figure 3a). Thus, in the presence of abundant light, neither LuxI nor cI is activated, and black pigment is not produced. In the absence of light, both LuxI and cI are expressed abundantly, and cI effectively inhibits the production of black pigment. However, along the edges of the image, enough 3OC6HSL is produced from

neighboring dark regions such that it activates $P_{lux\text{-}\lambda}$, while cI is not present in high enough concentrations to inhibit $P_{lux\text{-}\lambda}$. In this case, the engineered bacteria produce a black pigment. Therefore, the bacteria act as edge detectors due to the effective linking of AND and NOT gates, consisting of luxI, cI, luxR, and $P_{lux\text{-}\lambda}$, with the dark sensor and black pigment generator [41].

Another strategy to accomplish complex logic functions is to have separate *E. coli* strains perform different simple computations and link these logic functions using engineered communication between the different strains. By arranging these specialized cell colonies in different configurations and using QS molecules as virtual wires between the cells (Figure 3b), Tamsir et al. constructed all sixteen possible two-input Boolean logic gates, including the very complex XOR and EQUALS functions. The group obtained 5- to >300-fold higher gene expression when transitioning from the OFF to the ON states for each of these logic networks [42]. Regot et al. used a similar strategy to perform complex logic functions in engineered yeast cells. In this study, two communication molecules (α-factor from *S. cerevisiae* and α-factor from *C. albicans*) were used to link single colonies, which performed simple logic functions. Using these elements, the authors implemented several basic logic gates, including AND, NOR, OR, NAND, XNOR, and XOR gates, as well as more complex devices, such as a multiplexer and a 1-bit adder with carry [43]. Obviously, the computational capacity of these devices is nowhere near that of their electronic counterparts. However, examples, such as these,

represent the beginning of new methods in computation using biological substrates, which may improve with future advances in modularity, scalability, and reduction in cross-talk and noise.

1.5.2 Bioengineering

Cell-cell communication modules can also be used as critical components to aid in the engineering of circuits with practical applications. Along this line, an interesting problem that synthetic biologists encounter is that after their engineered cells perform a specific task, the cells are still present and capable of causing environmental harm or infections to human subjects. Furthermore, for specific tasks, it would be beneficial to control population size precisely if the task is sensitive to small fluctuations in gene expression. As a step towards addressing these issues, You et al. implemented a "population control" circuit, again using the LuxR/LuxI QS module. Upon circuit activation, LuxR and LuxI are both expressed. Once the population reaches a critical density, AHL can reach a high enough concentration to activate LuxR, thus inducing expression of a killer protein (CcdB) driven by a P_{luxI} promoter. An engineered cell population containing this circuit could maintain a constant population size well below carrying capacity for several days [47]. Depending on environmental conditions, the circuit could also generate robust, sustained population oscillations [48] (see below for further discussion on applications of QS in programming oscillatory dynamics).

Another application of QS-based communication modules is to coordinate the function of engineered tumor-killing bacteria [49, 50]. Several systems, constructed by Anderson et al., utilize sensor components in *E. coli* to target and kill cancer cell lines. Specifically, the systems consist of a sensor, which is activated when programmed *E. coli* cells detect high cell density (QS is activated), hypoxia conditions, or arabinose in the environment. When this switch is turned ON, it activates expression of an invasion protein, derived from *Y. pseudotuberculosis*, which enables the bacteria to invade cancer cells and then release a cytotoxic agent. Interestingly, for the communication-based sensor, the group was able to demonstrate controlled invasion of cancer cells only at a high *E. coli* cell density. The authors speculate that by coupling this component with another sensor, which responds only in the presence of cancer cells (i.e., their hypoxia sensor), they can further improve specificity in targeting cancer cells [49]. This work is still ongoing and provides a useful and ambitious direction for synthetic biologists to pursue.

Cell-cell communication modules have also been used to coordinate more complex population-level dynamics, such as oscillations. Although a synthetic oscillator acting on the single-cell level was first developed over a decade ago [5], its oscillations were noisy and exhibited tremendous cell-cell variability within a population. Since then, cell-cell communication has been adopted to better control such oscillations in two ways. One approach is exemplified by the synthetic population control circuit

mentioned above. In this circuit, the intracellular gene expression is directly integrated with population dynamics, leading to an integrated, population-level negative feedback. This circuit has been shown to generate robust, sustained oscillations for up to several hundred hours in a microchemostat [48]. In this case, it is important to note that cell-cell variability is critical for the generation of oscillations; otherwise, the population would completely crash if all cells simultaneously commit suicide at a high enough cell density.

In contrast to the previous example, another approach is to use cell-cell communication to synchronize a population of cells, within which each cell contains its own oscillator [51]. Synthetic biologists familiar with physics and engineering are particularly excited about this development given the usefulness of the Huygens paradigm of coupled pendulum clocks, which has been applied in the development of lasers, superconductor junctions, and the Global Positioning System (GPS) [51]. In addition, the role of synchronized clocks in cardiac function as well as a wide variety of developmental processes makes the advance an interesting toy system for biologists. In Danino et al.'s system, *luxI*, *aiiA*, and *yemGFP* are all placed under the P_{luxI} promoter. Each component is activated when the cell density is sufficiently high, upon which activated LuxR-AHL complex induces AiiA expression. AiiA then catalyzes AHL degradation. Thus, the system consists of interlocked positive-feedback (AHL-mediated activation of LuxI) and negative-feedback (AiiA-mediated AHL degradation) loops (Figure 3c). In a microfluidic device, the authors were able to demonstrate that this

synthetic gene circuit produced spatiotemporal oscillations in GFP fluorescence. Importantly, the oscillatory signal was coordinated among a localized population of engineered cells via the cell-cell communication module utilized (Figure 3d) [51].

Perhaps a population-level oscillator, by itself, does not constitute a practical application of synthetic biology. However, the same group took their system a step further by expanding on it to act as an arsenic detector. First, cells containing the modified gene circuit were arranged on a sensing array containing 500 "biopixels". Each biopixel contained ~5,000 *E. coli* cells. Within each biopixel, the oscillations were synchronized as described earlier via AHL signaling. In addition, the authors coordinated the oscillations among 500 biopixels using gas-phase redox signaling. The group then coupled this gene circuit to an arsenic sensor component by putting a supplementary *luxI* gene downstream of an arsenic-responsive promoter. Amazingly, when supplied with varying amounts of exogenously added arsenite, the device's GFP oscillatory period was directly proportional to arsenite concentration (Figure 3e). By reading the GFP oscillatory period among the many biopixels in their system, the investigators could effectively monitor arsenite concentration. They were able to quantify arsenite concentrations reliably down to 0.2 μM, which is below the 0.5 μM level recommended by the World Health Organization (WHO) for developing nations. Given this sensitivity, the authors put forth a design for integrating the system with a light-emitting diode (LED), photodetector, onboard processor, and graphic display in a

handheld sensor to effectively detect arsenite concentration. They estimated that excluding the cost of biological components, the whole device would cost less than $50 [52].

1.6 Disrupting cell-cell communication for potential therapeutic applications

Given the role of QS systems in virulence and in biofilm formation [4], efforts have been made to disrupt QS-mediated communication in pathogenic bacteria. Indeed, the development of QS inhibitors has been pursued aggressively in recent years, and various QS inhibitors have been the subject of clinical trials [53, 54]. In this section, we will discuss some general strategies for inhibiting QS in pathogenic bacteria as well as a small sample of a few innovative applications of these strategies.

A common method for disrupting QS is the use of small molecules. Using this method, one can target three different steps of QS signal processing: 1) signal generation, 2) signal secretion, and 3) signal reception (Figure 4a) [55]. Signal generation can be disrupted by inhibiting the synthase for the QS signal. Signal secretion can be interrupted by disrupting the membrane protein responsible for secretion (if it exists) or by increasing the degradation of the signal in extracellular space. Finally, signal reception can be inhibited by introducing analog QS signals (competitive inhibition), by inactivating receptor proteins (noncompetitive inhibition), or by disrupting the signal transduction cascade leading to downstream gene activation.

One of the more common QS inhibition strategies to date is the disruption of signal reception and transduction using small molecules. As mentioned above, competitive inhibition and noncompetitive inhibition can be utilized to interfere with signal processing. Competitive inhibition is achieved through the use of analog small molecules that resemble the QS signal of interest. The goal is for the analog small molecules to saturate the receptor proteins such that the actual QS signal cannot effectively bind the receptor proteins and activate downstream gene expression. This type of competitive inhibition was introduced by Gamby et al., who synthesized a diverse set of analogs to the QS signal AI-2, which is utilized by over 70 bacterial species. Gamby et al. demonstrated that these analogs successfully disrupted AI-2 signaling in *E. coli*, *S. typhimurium*, and *P. aeruginosa* [56]. Another strategy for disrupting signal processing is noncompetitive inhibition in which a small molecule is designed to bind to the receptor protein, rendering it inactive. For example, Chen et al. engineered a small molecule that stabilized a closed conformation of the *C. violaceum* LuxR-type protein CviR, which was unable to bind the QS signal C6-HSL [57].

Another strategy to inhibit QS involves the use of enzymatic modification of the QS signal such that it can no longer bind to its receptor protein. For example, Roy et al. introduced a protein kinase LsrK that phospohorylates and inactivates AI-2. This strategy was shown to be effective in inhibiting the QS response in *E. coli*, *S. typhimurium*, and *V. harveyi* [58].

Inhibition of QS need not be restricted to the use of small molecules or proteins. Recently, investigators have developed some cell-based strategies, where microbes are engineered to interfere with the QS capabilities of potentially harmful bacteria. For example, Saeidi et al. engineered *E. coli* to detect AHLs produced by pathogenic *P. aeruginosa* and then produce pyocin S5 and lysis E7 in response. The lysis protein lyses the engineered *E. coli* cells, thereby releasing pyocin S5, a bactericidal agent that kills the *P. aeruginosa* population. This method led to a 99% reduction in viable *P. aeruginosa* cells as well as a 90% reduction of *P. aeruginosa* biofilm formation [59]. In another example of cell-based QS inhibition, Hong et al. engineered an *E. coli* strain to produce the protein Hha13D6, which activates proteases that disperse biofilms, while communicating with other cell strains via QS. This cell strain was able to disperse an existing biofilm formed by another engineered *E. coli* strain via QS and then replace it with its own biofilm [60]. In the future, this strategy could perhaps be utilized to replace a biofilm of a pathogenic cell strain with a biofilm of a relatively innocuous strain, which could then be removed more easily.

Both studies discussed above were carried out *in vitro* and thus were not subject to the many complicating factors that are present physiologically. However, Duan and March provided a proof-of-concept demonstration of the efficacy of QS inhibition *in vivo* using an infant mouse model. Briefly, the *E. coli* Nissle 1917 strain was engineered to produce cholera autoinducer 1 (CAI-1), which was aimed at disrupting the proper

timing of *V. cholerae* virulence expression and colonization. Indeed, 8-hr pretreatment with the *E. coli* strain increased the mice's survival 92% after ingestion of *V. cholerae*, while co-ingestion of the *E. coli* with *V. cholerae* increased survival 27% [61]. Such a strategy may have implications for treating cholera and other infections that plague human health.

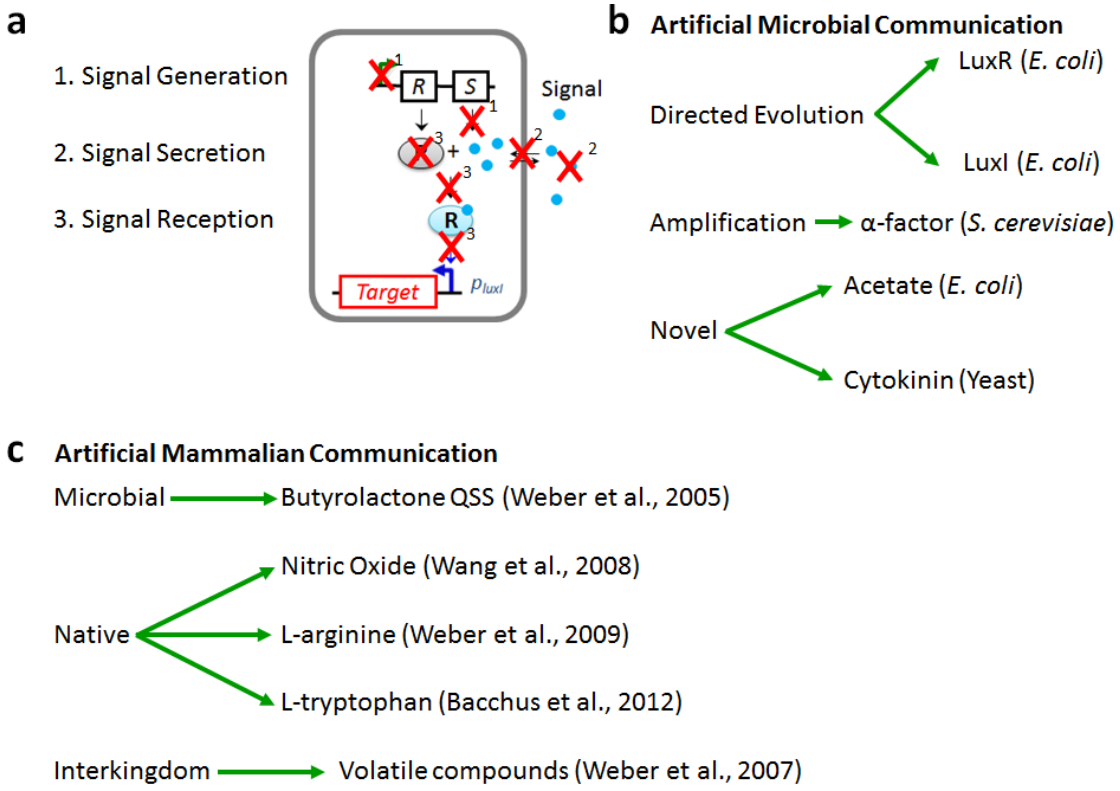

Figure 4: a) Targets for disrupting QS. There are three targets for disrupting QSSs: 1) signal generation, 2) signal secretion, and 3) signal reception. Signal generation can be disrupted by inhibiting transcription or translation of the protein synthesizing the signal. Signal secretion can be disrupted by interfering with the secretion of the signal itself or by degrading the signal. Signal reception can be disrupted by interfering with the receptor protein or the ability of the receptor protein to activate downstream processes. b) Artificial microbial cell-cell communication channels. Directed evolution was utilized to change the responsiveness of LuxR to varying chemical signals and the synthesis rate of AHL by LuxI in *E. coli*. Amplification of the

α-factor signal increased system responsiveness in *S. cerevisiae*. Recent novel artificial communication systems include acetate in *E. coli* and cytokinin in various yeast strains. c) Artificial mammalian cell-cell communication channels. These channels have three origins: microbial, native, and interkingdom. The QS system involving butyrolactone was ported from the microbe *S. coelicolor* and retrofitted to mammalian cells. Native signals NO, L-arginine, and L-tryptophan have all been used as communication signals in synthetic mammalian systems. Finally, various volatile compounds from many kingdoms have been used to mediate communication between synthetic mammalian cells and cells from other kingdoms.

1.7 Engineering artificial cell-cell communication modules

Most of the systems we have described previously rely on existing QS systems from closely related species to implement synthetic communication in bacteria and yeast pheromones to implement synthetic communication in yeast. However, improvements to these existing communication modules as well as the development of new communication modules are likely to expedite the advancement of synthetic systems which communicate on a population-level. Improvements to existing QS modules make components more malleable to mesh with other design specifications. Novel communication modules provide more options when constructing synthetic systems and alleviate various concerns regarding modularity, scalability, and cross-talk between closely related QS modules.

1.7.1 Improvements to existing cell-cell communication modules

A common approach to improve naturally existing QS modules is to utilized directed evolution to evolve such modules toward desired functions (Figure 4b). Briefly, the goal of directed evolution is to engineer a specific protein function through several

rounds of mutation and selection. The process starts with a parent protein, which performs a task close to that which is desired for a specific component in the designed system. A large library of DNA encoding mutant versions of the parent protein can be generated via a number of methods, including error-prone PCR, recombination, and computer-guided mutagenesis. The library of mutants is then tested for functionality via a functional assay, which generally consists of a high-throughput screen or selection. After multiple rounds of mutation and selection, a mutant version of the parent protein is identified which best fits the design criteria of the engineered system [62].

This process of directed evolution has been applied to a number of QS components. For example, Collins et al. were able to change the signaling specificity of a version of LuxR using a dual selection assay. Specifically, they wanted to take an initial version of LuxR which responded to a broad range of acyl-HSLs, including straight-chain acyl-HSLs, and derive from it a mutant version which no longer responds to its native cognate signal 3OC6HSL, while retaining its response to straight-chain acyl-HSLs. The assay consists of two rounds of random mutagenesis and selection. For rounds of ON selection, a library of mutagenized *luxR* genes was cotransformed with a construct containing a chloramphenicol-resistance gene downstream of the P_{luxI} promoter. The colonies were exposed to alternate straight-chain acyl-HSLs in plates containing chloramphenicol. Thus, only those mutants that could effectively respond to the alternate acyl-HSLs were selected after several rounds. Similarly, for each round of OFF

selection, the library of mutagenized *luxR* genes were cotransformed with a construct containing β-lactamase inhibitory protein (Bli) downsteam of the P_{luxI} promoter along with constitutively expressed β-lactamase. Here, β-lactamase confers resistance to carbenicillin, and Bli can inhibit β-lactamase. In this manner, in the presence of 3OC6HSL and carbenicillin, only the mutagenized LuxR proteins that do not respond to 3OC6HSL are selected. Multiple rounds of ON and OFF selection identified a LuxR mutant that responds to straight-chain acyl-HSLs but not 3OC6HSL [63]. This novel selection method can theoretically be applied to achieve LuxR specificity for any number of QS signals, while eliminating responses to other QS signals. Therefore, the method can be applied to eliminate or greatly reduce cross-talk in synthetic systems requiring multiple modes of communication.

Selection can also be applied to obtain mutants of LuxI, which synthesize more 3OC6HSL. Kambam et al. accomplished this by cotransforming a plasmid that constitutively expressed LuxR and LuxI mutants with a plasmid containing the P_{luxI} promoter driving expression of β-lactamase. By selecting for colonies that grew in the presence of very high concentrations of ampicillin (an analog of carbenicillin), the investigators obtained LuxI mutants that synthesize 80-fold more 3OC6HSL than the wild-type version [64]. From an engineering perspective, the ability to modulate 3OC6HSL synthesis capacity is useful as it may be necessary to tune such a parameter to fit the design of a given system.

Enhancement of the production of a communication signal can also be accomplished without the need for genetic selection. For example, using the *S. cerevisiae* pheromone α-factor as a cell-cell communication module, Gross et al. introduced amplifier strains, which would respond to environmental α-factor by producing more α-factor themselves. In this fashion, the group achieved a more sensitive response to α-factor within a mixed population of yeast cells (Figure 4b) [65]. Again, this strategy could be utilized by synthetic biologists constructing systems that require a highly sensitive response to cell-cell signaling.

1.7.2 Novel microbial cell-cell communication modules

Bulter et al. engineered an artificial cell-cell communication system in *E. coli* by rewiring its metabolic pathway. The group knocked out the main production pathway of acetate from AcCoA to make acetate a function of cell growth, rather than a function of metabolic state or environmental conditions (Figure 4b). Furthermore, by knocking out the histidine kinase NR_{II}, the group simplified the intake process of acetate such that a signaling cascade initiated in proportion to acetate concentration induced the promoter $glnAp_2$ [66]. Similarly, Chen and Weiss effectively integrated a modified plant hormone communication system in yeast (Figure 4b). In their system, the plant hormone cytokinin is synthesized in proportion to cell density and subsequently activates a phosphorylation pathway that induces an SSRE promoter [67]. Because both of these modules are synthetic, their signaling is highly specific and unlikely to initiate

undesirable cross-talk. Furthermore, the modules provide synthetic biologists with more communication pathways to utilize when engineering systems that require many channels of communication.

1.7.3 Engineered mammalian cell-cell communication modules

In general, engineering of mammalian cells has lagged behind engineering of bacteria or even yeast. This is primarily due to the mammalian cell's greater complexity and a poorer understanding of the cellular processes in the mammalian cell. However, the last several years has witnessed some rapid progress in the engineering of synthetic gene circuits in mammalian cells, including the creation of artificial cell-cell communication (Figure 4c).

One method of accomplishing artificial mammalian cell-cell communication is to port a well-studied communication module into mammalian cells. Weber et al. did precisely this by porting a QS module from the bacterium *S. coelicolor* into several mammalian (including human) cell lines. Briefly, this process was done in two steps: 1) the QS receptor protein was fused to a human transsilencing domain; 2) the QS-inducible promoter was constructed using eight tandem transilencer-specific operator modules derived from a viral promoter. Thus, the QS module was "retrofitted" to be effective in mammalian cells. Weber et al. suggested several desirable features that this retrofitted system offers, including a high sensitivity to low doses of the QS signal butyrolactone and low basal expression in the absence of butyrolactone [68].

Another method for introducing artificial cell-cell communication in mammalian cells is to rely on natural cell-cell signaling molecules. For example, Wang et al. used nitric oxide (NO) as an effective QS signal in A549 human lung carcinoma cells. In their system, the QS signal NO was produced when NO synthase (NOS) catalyzed the conversion of L-arginine to L-citrulline, leaving behind NO, which is secreted outside of the cell membrane. By inducing a signaling cascade, sufficient concentrations of NO activate the *c-fos* promoter. The authors suggest that this cell-cell communication module is advantageous to the previous portable QS network since NO is more compatible with mammalian cells. In addition, NO diffuses across cellular membranes without the need for specific membrane channels [69].

Another natural cell signaling molecule utilized to enable mammalian cell-cell communication is L-arginine. Weber et al. synthesized this molecule using a human liver-type arginase in a human sender cell. Meanwhile, a Chinese hamster ovary (CHO) cell line, equipped with a transgene expression system, which converts L-arginine concentrations into transcription of GFP in a dose-dependent manner, constituted the receiver cell [70]. In this manner, Weber et al. successfully implemented a communication system in mammalian cells that was activated at high cell densities. Similarly, the same group recently implemented mammalian cell-cell communication with another amino acid, L-tryptophan [71]. However, for the L-tryptophan, L-arginine, and NO communication modules, given their widespread importance in mammalian

cell signaling, those wishing to use these modules must be mindful of cross-talk with other natural gene networks.

1.7.4 Engineered inter- and intrakingdom communication

Weber et al. also designed synthetic cell-cell communication among different species and kingdoms. Specifically, airborne communication was introduced between and within populations of mammalian cells, yeast, plants, and bacteria. The basis of this communication was volatile acetaldehyde. One potential advantage of airborne communication is that it affords the opportunity of communication between sender and receiver cells that do not occupy the same liquid-phase environment [72]. Furthermore, this mode of communication allows for synchronization of very different organisms with specific capabilities or specialties and therefore can aid in activating a consortium of varying organisms assigned to different tasks.

1.8 Conclusion

Here, we have discussed recent studies of synthetic biological systems which utilize cell-cell communication. These systems span a wide variety of implementations and applications. Although the number and quality of studies on such systems is impressive, it is important to remember that synthetic biology is still quite new. The field has started as more of an art form than an engineering discipline with many rounds of trial and error before a suitable system is identified which is sufficient to achieve the initial design goals (see Chapter 3). However, the field is now transitioning towards the

engineering of well-defined components which behave as predicted. As the field reaches this transition point, synthetic biologists will likely be spared from the frustrating trial and error process and be free to better tackle new challenges. These challenges will include biological challenges, such as the unintended consequences of host-circuit interactions [73, 74], the impact of stochastic gene expression [75-77], and the limits of the metabolic capacity of the cell, as well as technical challenges, such as the real-time monitoring of gene circuit components, the development of high-throughput functional assays to test new biological devices, and the limits of high-fidelity DNA synthesis technologies. Although these problems may seem daunting, one can take comfort in the fact that incremental improvement in dealing with each of these challenges exponentially improves our capacity to generate useful biological parts faster, cheaper, and more predictably.

2. Case study in pattern formation: A synthetic predator-prey system

As mentioned previously, a synthetic system was engineered to mimic the prototypical predator-prey relationship in which a predator cell kills a prey cell and the prey cell rescues the predator cell (Figure 1b). I was directly involved in the solid-phase characterization of this system and performed many critical experiments validating several of the main points. In this chapter, I will first discuss the crux of the study and then discuss some of the supplemental experiments I conducted in conjunction with Dr. Hao Song to prove some of the supporting claims necessary to confirm some of the study's critical assumptions. The work described in this chapter is published: Song H, Payne S, Gray M, You L (2009). "Spatiotemporal modulation of biodiversity in a synthetic chemical-medicated ecosystem." *Nature Chemical Biology* **5**(12): 929-935; Payne S, Smith RP, You L. "Quantitative analysis of the spatiotemporal dynamics of a synthetic predator-prey ecosystem." *Synthetic Gene Networks*. Ed. W Weber and M Fussenegger. *Methods in Molecular Biology.* (New York: Humana Press, 2012). Vol. 813, Part 4, p. 315-330.

2.1 Main points of the study

Biodiversity, or the relative abundance of species, measures the persistence of an ecosystem. To better understand its modulation, we analyzed the spatiotemporal dynamics of a synthetic, chemical-mediated ecosystem that consisted of two engineered

Escherichia coli populations. Depending on the specific experimental conditions implemented, the dominant interaction between the two populations could be competition for nutrients or predation due to engineered communication. While the two types of interactions resulted in different spatial patterns, they demonstrated a common trend in terms of the modulation of biodiversity. Specifically, biodiversity decreased with increasing cellular motility if the segregation distance between the two populations was comparable to the length scale of the chemical-mediated interaction. Otherwise, biodiversity was insensitive to cellular motility. Our results revealed a critical difference between contact- and chemical-mediated ecosystems and suggested a simple criterion for predicting the modulation of biodiversity by habitat partitioning and cellular motility.

2.1.1 Motivation

Microbial ecosystems play fundamental roles in a wide variety of biological processes, including biogeochemical cycles in the biosphere [78-80], immunological defense against pathogens by gut microbiota [81, 82], and engineered microbial consortia for biotechnological applications [83]. One important characteristic of microbial ecosystems is biodiversity, which represents species richness and relative abundance in relation to one another [84]. A central challenge in microbial ecology is to elucidate the mechanisms underlying the maintenance of biodiversity, a vital element in determining the persistence and functionality of ecological communities [85-93].

There are two types of cell-to-cell interactions in microbial ecosystems [94, 95]. The first type occurs locally and requires cell-cell contact. One microbial species, for example, may kill another by contact. This contact may occur by epibiotic means (e.g., *Vampirococcus* attaches to the outer surface of *Chromatium* to induce killing [96, 97]), by periplasmic invasion (e.g. *Bdellovibrio* upon gram-negative prokaryotes [98]), or by invasion into the cytoplasm (e.g., *Daptobacter* upon *Chromatium minus* [96]). Another example is a three-species rock-paper-scissors microbial community [99, 100], where cell-cell interactions occur locally; that is, the bacteria only kill or inhibit their immediate neighbors.

The second type occurs via diffusible chemicals. This can happen when microbes compete for shared, diffusible nutrients or chemoattractants, when each species excretes an essential metabolite for the survival of the other, forming a mutualistic relationship [20], or when predator cells excrete diffusible hydrolytic enzymes that degrade and digest prey cells to generate diffusible nutrient molecules, which contribute to the predator's survival (e.g., both *Myxococcus* and *Lysobacter* use lytic enzymes to prey upon other bacteria [101-103]). Such chemical-mediated interactions play essential roles in determining many behavioral responses of microbes, such as sex, alarm and aggregation as well as predation [14, 104-111].

Studies have highlighted the importance of cellular motility in determining biodiversity in contact-based ecosystems: reducing motility promotes biodiversity [99,

100]. However, it is unclear if and how motility can impact biodiversity in chemical-mediated ecosystems. Specifically, how does the combination of cellular motility and long-range interactions via diffusible chemicals affect biodiversity?

To address this question, we employed a synthetic chemical-mediated predator-prey ecosystem [18] (Figure 5). This system consists of two engineered *E. coli* populations mediated by quorum-sensing (QS). The predator kills the prey by inducing expression of a killer protein (CcdB), whereas the prey rescues the predator by inducing expression of an antidote (CcdA) in the predator. The two populations also compete for shared resources in co-culture (Figure 6a). Thereby, the programmed predation and the competition for nutrients occur through chemical diffusion. Overall, this synthetic system resembles many natural chemical-mediated predator-prey ecosystems in terms of their interaction characteristics, both of which involve diffusion-mediated interactions.

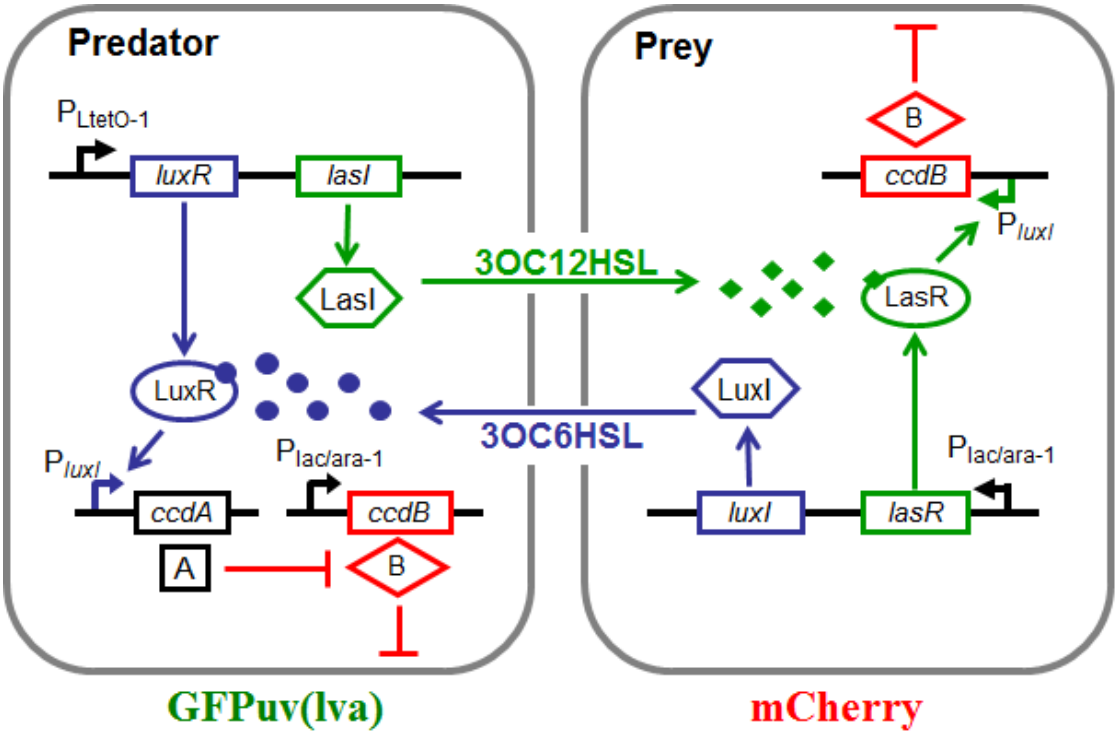

Figure 5: Schematic of the synthetic predator-prey ecosystem. Two engineered *E. coli* strains regulated each other's survival or death through QS. Upon IPTG induction, the predator produced 3OC12HSL to induce CcdB (a killer protein) expression in the prey. The prey produced 3OC6HSL to induce CcdA (an antidote protein) expression to rescue the predator. The predator and the prey constitutively expressed GFPuv(lva) and mCherry, respectively.

2.1.2 Central findings

2.1.2.1 Reduced motility could promote biodiversity in partitioned habitats

Studies on the metapopulation dynamics in ecosystems suggested that habitat partitioning might affect biodiversity [112-116]. We thus sought to examine how habitat configuration, in conjunction with motility, could affect biodiversity in our system. To simulate habitat partitioning, we seeded the predator and the prey separately at two focal points with varying distance in between, leaving the other locations with zero

density. Our model predicted that increasing the segregation distance between the seeding points would promote biodiversity (Figure 7a). If the predator and prey were seeded together (d = 0), the predator would disperse outward at a faster speed than the prey due to its growth advantage gained from the prey's rescue. The outward dispersion of the predator would deplete chemoattractants in its path (Figure 8), which would trap the prey at the inoculation point. Increasing the segregation distance between the two populations (e.g., d = 1 and 2 cm) would reduce the strength of long-range interactions, including killing and rescuing by the diffusible AHL signals and competition for chemoattractants and nutrients. This reduction would lead to less killing, faster growth, and more chemotaxis of the prey, resulting in a larger prey territory and density. To test the prediction experimentally, we seeded 10 μl predator cells and 10μl prey cells at two separate locations with increasing distances (d = 0, 1, or 2cm) on pH-buffered soft (0.2%) M9 agar plates, which were incubated at 37^{o}C for 20 hrs. We then measured the cell densities by fluorescence imaging (see details in 2.2.1). Figure 7b showed that the biodiversity indeed increased with increasing segregation distance, consistent with the model prediction (Figure 7a). In particular, increasing initial partitioning distance from 0cm to 2cm increased the BI from ~0.07 to ~0.37 (0.3% agar).

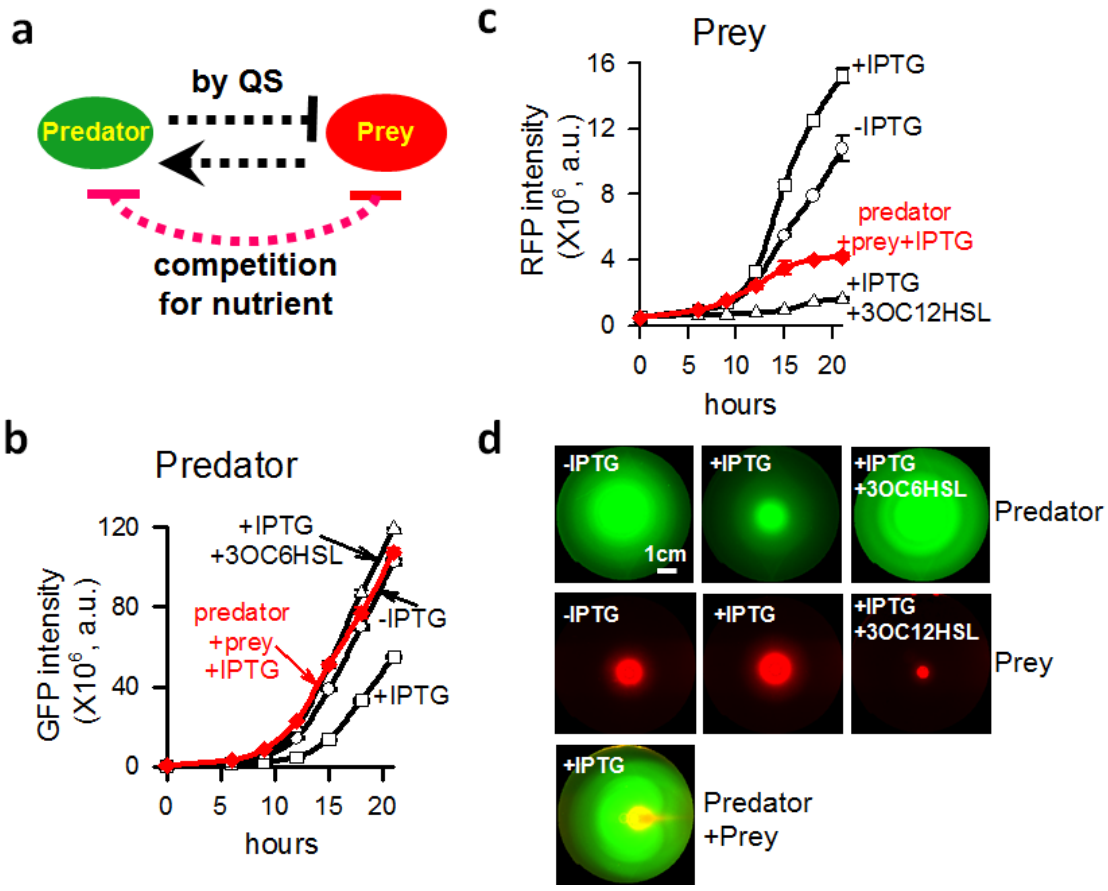

Figure 6: Spatiotemporal dynamics of the predator and the prey in response to IPTG and AHLs in solid phase. The experiments were performed on 0.2% M9 (pH=7) soft agar at 37°C. a) The interaction logic of the chemical-mediated synthetic predator-prey ecosystem. The two populations competed for nutrients and followed the programmed predator-prey interaction *via* QS. b) Predator dynamics without IPTG, with IPTG, and with IPTG and 3OC6HSL. The GFP intensity was proportional to the predator density. Each bar indicated the range of GFP intensity measured in duplicate experiments. Unless noted otherwise, IPTG was applied at 1mM and AHLs were applied at 100nM. c) Prey dynamics without IPTG, with IPTG, and with IPTG and 3OC12HSL. The RFP intensity was proportional to the prey density. Each bar indicated the range of RFP intensity measured in duplicate experiments. d) Predator patterns (at 18hr) without IPTG, with IPTG, and with IPTG and 3OC6HSL indicated that the predator expansion was significantly reduced by IPTG, but rescued by 3OC6HSL. Prey patterns (at 18 hr) without IPTG, with IPTG, and with IPTG and 3OC12HSL indicated a drastic reduction in prey expansion by 3OC12HSL and IPTG. A composite GFP and RFP image of a plate seeded with 10μl predator overnight culture (~10^6 cells) and 10μl prey overnight culture (~10^6 cells) 0.5cm apart and

incubated for 18 hours. The patterns from duplicate measurements were similar; only one was shown.

Our model further predicted that decreasing motility would increase biodiversity when the populations were sufficiently segregated (Figure 7a, d = 1cm or 2cm). This was mainly because motility affected the spatiotemporal interaction strengths between the predator and the prey under this condition. At a higher motility, the predator and the prey would approach each other at a faster speed; in turn, the prey would experience a higher level of 3OC12HSL secreted and diffused from the predator, thereby exhibiting a stronger predation effect. However, at a lower motility, the two populations would approach each other slowly; in turn, the prey would experience less killing, leading to faster prey growth and higher biodiversity. Again, this prediction was validated by experiments: at d= 1cm or 2cm, decreasing motility by reducing the agar density from 0.2% to 0.3% increased the BI by about 2~3 fold (Figure 7b).

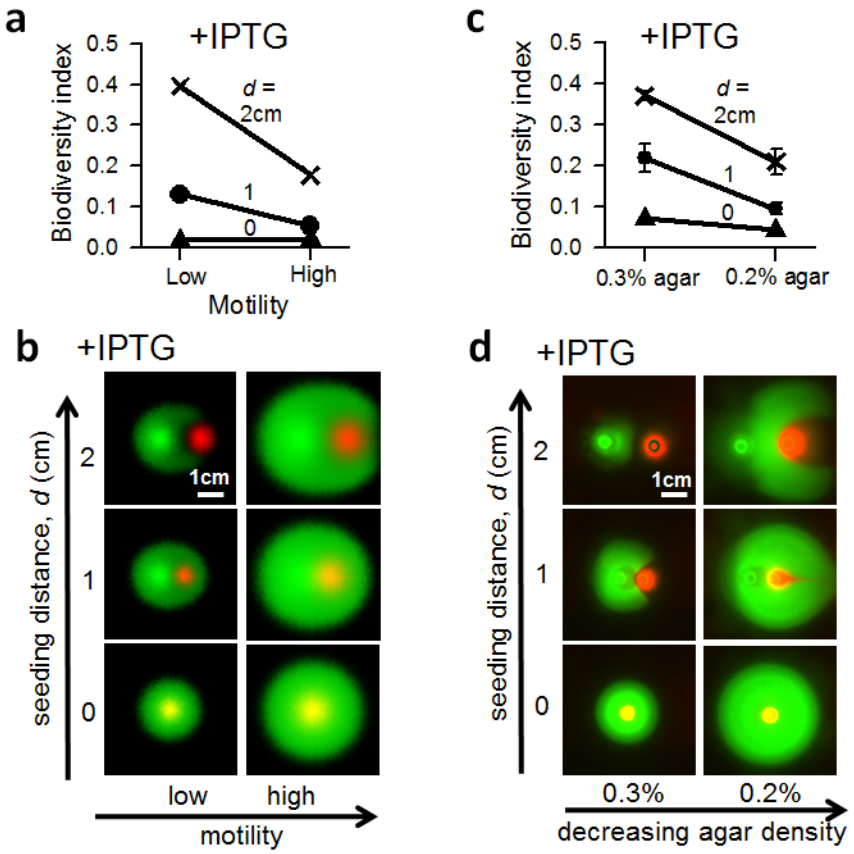

Figure 7: Reduced motility promoted biodiversity if seeding habitats were partitioned. a) Modeling showed that decreasing motility increased BI for a sufficient segregation distance (d = 1 or 2 cm), but not for d = 0. To reduce motility in modeling, we decreased the values of the cellular diffusivities (D_{p1}, D_{p2}) and chemotaxis constants (α_1, α_2) by four-fold from those of the high motility. The BIs were computed based on the predator-prey patterns at 20hr (b). b) Simulated predator-prey patterns at high and low motility with different seeding segregation distances, corresponding to the conditions in (a). Snapshots were taken at 20hr after the simulation initiation. c) Experiments validated the model prediction in (a) by using agar density to control motility: 0.2% M9 agar (high motility) and 0.3% M9 agar (low motility). Snapshots were taken at 20hr after seeding the predator and the prey. Each error bar indicated the range of biodiversity index measured in duplicate experiments. d) Experimentally measured predator-prey patterns (at 20hr) in 0.2% and 0.3% agar plates with varying seeding segregation distances (0cm, 1cm and 2cm), corresponding to the conditions in (c). The patterns from duplicate experiments were similar; one set was shown.

We further noticed that the promotion of biodiversity by motility with sufficient habitat partitioning did not require induced predation. For instance, without IPTG induction, the dominant interaction in our system was competition for nutrients (Figure 6a). For the pair implemented in MG1655 cells, the uninduced predator had a significant growth advantage over the uninduced prey (Figure 6b). Our results revealed two salient points. First, the spatial patterns and the biodiversity indices resulting from competition (see 2.2.2 and Figure 9) were significantly different from those due to induced predation (Figure 7), as highlighted by the detailed comparison of the predator's spatial patterns (Figure 10). Second, similar to the case with induced predation (Figure 7), reduced motility also increased biodiversity when the two populations were sufficiently segregated (Figure 9, d = 1cm or 2cm). Furthermore, the latter conclusion did not depend on chemotaxis either. In Top10F' cells, which can diffuse in thin agar but are impaired in their ability to chemotax, reduced motility also promoted biodiversity with sufficient segregation distance, as revealed by both modeling and experiments (Figure 11b, d, f). However, this motility-mediated biodiversity modulation became negligible when competing populations had similar growth rates: neither motility nor segregation distance impacted biodiversity (see 2.2.2, Figure 11c, e, g (Top10F'), and Figure 12 (MG1655)).

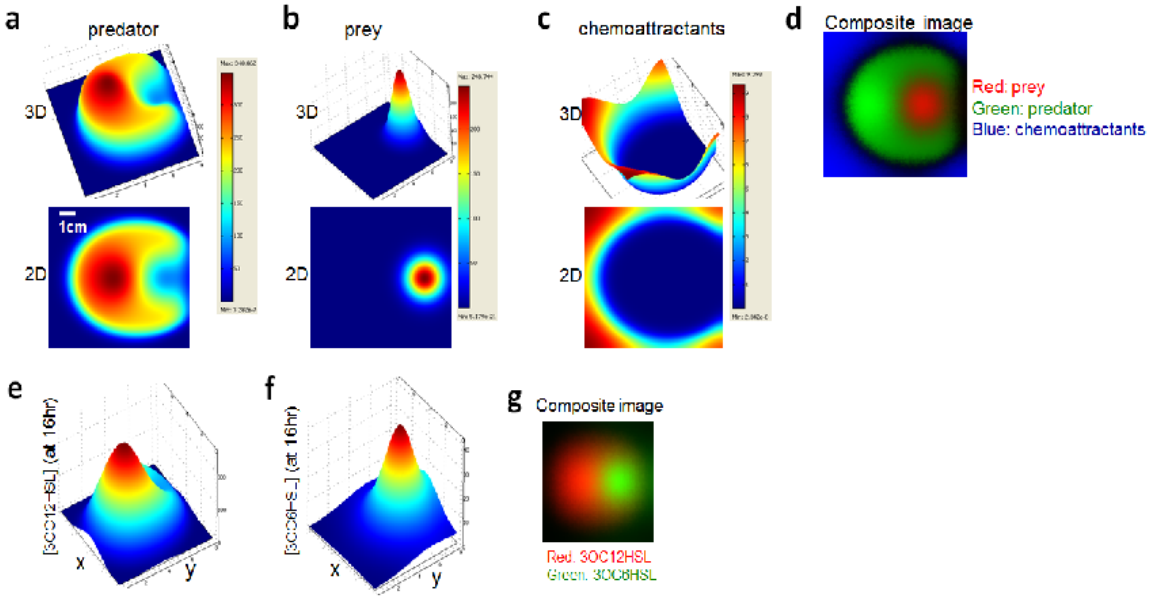

Figure 8: Our computational results showed that (1) the affinity of the predator for growing is higher in the vicinity of the prey and that (2) chemoattractants were exhausted in the wake of the populations' migration. a) The 3-D and 2-D distributions of the predator cell density (at t=20hr). The predator had a higher cell density in the vicinity of the prey because the rescuing signal (3OC6HSL) concentration produced by the prey was higher in this region; thus, the rescuing of the predator was more significant in the vicinity of the prey than at a distance. b) The 3D and 2-D distributions of the prey cell density (at t=20hr). c) The corresponding 3-D and 2-D distributions of chemoattractants concentration (at t=20hr). The chemoattractants were almost exhausted in the path of dispersion of the predator and prey from the inoculation point. d) The composite image that demonstrates the distribution of the predator density (green), the prey density (red), and the chemoattractants concentration (blue). e) Simulated 3-dimensional (3-D) distribution of the 3OC12HSL corresponding to the predator-prey pattern shown in (a) and (b). f) Simulated 3-dimensional (3-D) distribution of the 3OC6HSL corresponding to the predator-prey pattern shown in (a) and (b). The distributions of 3OC12HSL (e) and 3OC6HSL signals showed that the predator and prey fully interacted in the spatial domain. g) The composite images of the distribution of the two AHLs signals were shown in (e) and (f), where the red represented 3OC12HSL and the green represented 3OC6HSL.

These analyses also revealed a potential limitation of the biodiversity index. As a lumped metric, it is convenient to use for summarizing system dynamics and has

revealed a commonality between predation and competition in terms of the contributions of motility and population segregation to biodiversity. However, the metric can mask important differences in the spatiotemporal patterns resulting from different interactions. When predation was induced by IPTG, cell distribution patterns revealed a growth preference of the predator in the vicinity of the prey (Figure 10a). Without IPTG induction, the uninduced predator population expanded almost uniformly from the seeding point toward all directions except near the uninduced prey population (Figure 10b). This difference in pattern formation was also qualitatively captured by our model (Figure 10c-d). However, since our model is drastically simplified, some fine details of the experimental patterns were not quantitatively captured by our model. Together, a combination of biodiversity index and population distribution patterns would provide a comprehensive picture of the commonality and difference in the system dynamics, with or without induced predation.

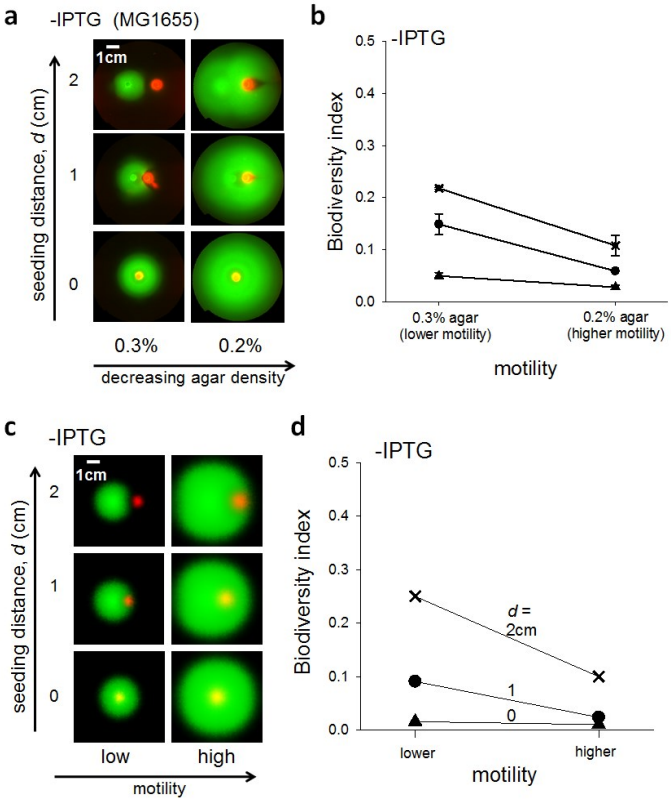

Figure 9: Spatiotemporal dynamics of the ecosystem in the absence of IPTG, where the circuit was OFF and the dominant interaction between the two populations was competition for diffusible, shared nutrients. a) Snapshots of predator (GFPuv) and prey (mCherry) patterns on soft M9 agar plates. The agar plates were seeded with 10μl MG1655 predator and prey cells at varying initial seeding distances and agar densities and incubated for 20 hrs. b) Dependence of biodiversity index on motility, calculated from the data in (a). c) Simulated pattern formation of the two competitive populations. These patterns agreed well with the experimental data (a). e) Simulated dependence of biodiversity index on motility, calculated from data in (C). Again, these results agreed well with the experimental data (B).

2.1.2.2 Effects of motility as constrained by two critical segregation distances

Our results appeared to suggest a conflicting role of motility in modulating biodiversity. When the predator and the prey were seeded in close proximity, motility had a negligible impact on biodiversity; when they were seeded separately, motility had

a drastic impact on biodiversity. To resolve this apparent paradox, Dr. Hao Song examined the interplay between segregation distance and motility by simulation. He initiated each simulation by seeding individual cells in random patches separated by barren zones containing no cells (Figure 13a). Also, the predator and the prey were not seeded in the same patch. By modifying the area of the barren zones, he could modulate the average segregation distance between the two populations. A typical result is shown in Figure 13b, where he examined the dependence of biodiversity on the segregation distance at a fixed cellular motility (D_{cell} = 10^{-3} cm^2/hr). It showed that an increasing segregation distance (d) had little impact on biodiversity until d exceeded a critical value (d_{c1}), where the dependence of the BI on d went through a distinct transition. When $d>d_{c1}$, the BI increased almost proportionally with increasing d until d reached another critical distance d_{c2}. When $d > d_{c2}$, the BI again was independent of the furthering increment of d (Figure 13b).

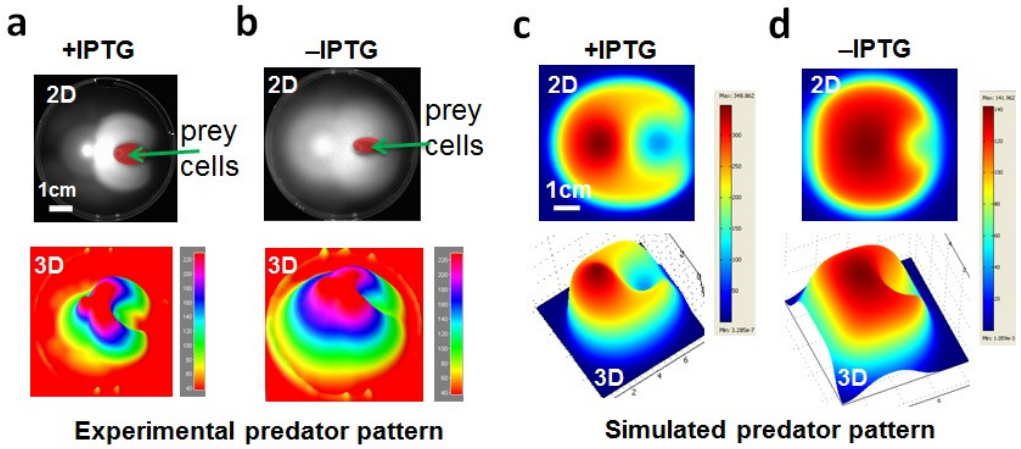

Figure 10: Detailed comparison of the spatial patterns resulting from the system (a, c) with induced predation, and (b, d) without induced predation. a) 2D and 3D

distribution patterns of the predator in the system induced by IPTG, where the dominant interaction was predation. In the 2D snapshot, the cell density distribution was captured by the grey level. The brighter the area, the higher the cell density. Both patterns illustrated the growth preference of the predator in the vicinity of the prey. These patterns were regenerated from the result in Figure 7d (upper-right panel: 0.2% agar, *d*=2cm). The predator and prey cells were seeded with a segregation distance *d*=2cm and incubated on 0.2% M9 agar (pH=7) for 20hrs. Snapshots were taken by the Kodak image station. b) 2D and 3D distribution patterns of the predator in a system not induced with IPTG, where the dominant interaction was competition. These patterns were regenerated from the result in Figure 9a (upper-right panel: 0.2% agar, *d*=2cm). c) and d) were simulation results that qualitatively captured the salient features of the predator distribution patterns in the experimental results in (a) and (b), respectively. The induced predation patterns (c) were regenerated from the computational result in Figure 7c (upper-right panel: high motility, *d*=2cm). The uninduced competition patterns (d) were regenerated from computational result in Figure 9c (upper-right panel: high motility, *d*=2cm).

The same trend relating segregation distance to biodiversity could be captured by 1-D simulations, which were much more efficient computationally. Dr. Hao Song initiated each simulation by seeding the predator and the prey at two focal points with a distance d, while setting the other places empty (Figure 14a). Similar to the 2D simulations (Figure 13), he could then determine the BI from the resulting predator and prey distributions (Figure 14a). Under the same conditions, similar to the 2D results (Figure 13b), 1D simulations also identified two critical transition points (d_{c1} and d_{c2}) in the dependence of the BI on d (Figure 14b). After the system reached stationary phase upon nutrient depletion, the dependence of the BI on d was approximately invariant with time.

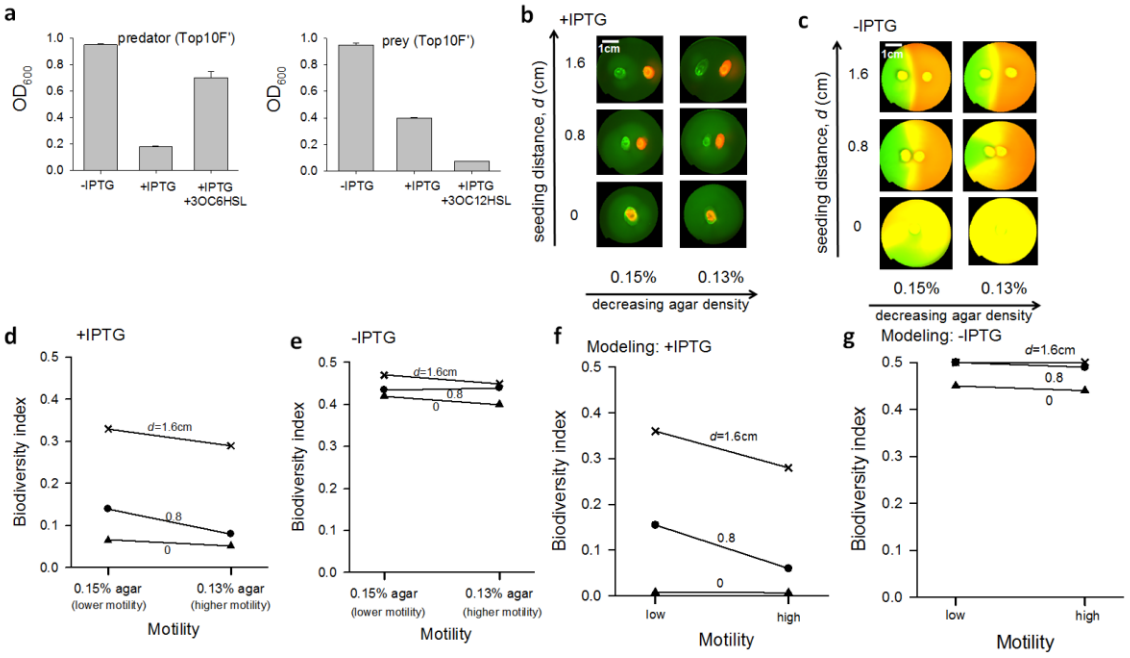

Figure 11: Dynamics of the ecosystem implemented in Top10F′ cells, which can diffuse in thin agar but with impaired chemotax. Because of the much slower growth rate and motility of Top10F′ cells in comparison to MG1655 cells, we used a very rich medium (2xYT) for these experiments. Also, because of the impaired ability of these cells to chemotax towards chemoattractants, we used much softer agar (0.13 – 0.15%) for the spatial experiments. a) Comparison of Top10F′ predator (left panel) and prey (right panel) OD_{600} after 9 hrs of growth in liquid 2xYT media supplemented with 0.1 μg/ml anhydrotetracycline (aTc) and without IPTG, with 1 mM IPTG, and with 1 mM IPTG and 100 nM appropriate AHL. b) Snapshots of the predator (GFPuv) and prey (mCherry) patterns formed on pH-buffered 2xYT soft agar (pH=7). With IPTG induction, the circuits were ON. The soft agars were seeded with 10 μl Top10F′ predator and prey at varying initial seeding distances (0cm, 0.8cm and 1.6cm) and agar densities (0.13%, and 0.15%) after 36 hrs of growth in the presence of 1 mM IPTG. c) Snapshots of the patterns of the two populations after 36hrs of growth in the absence of IPTG induction, where the dominant interaction was competition. These patterns were also performed on pH-buffered 2xYT soft agar (pH=7). d) Dependence of biodiversity index on cell motility for the plates seen in (b), i.e., in the presence of IPTG. e) Dependence of biodiversity index on cell motility for the plates seen in (c), i.e., in the absence of IPTG. f) Simulated biodiversity index versus cellular motility (only diffusion, in the absence of chemotaxis) in the predator-prey ecosystem. This result agreed well with the experimental data in (d). g) Simulated biodiversity index versus cellular motility (only diffusion, in the absence of chemotaxis) in the

ecosystem with only competition interaction. This result agreed well with the experimental data in (e).

These transitions could be attributed to varying coupling strength by the diffusible nutrients and QS signals. When $d < d_{c1}$, the chemical-mediated interactions were dominant, sufficiently strong, and did not depend significantly on small variations of the cells' positions. Therefore, cell motility would not influence the strength of cell-cell communication and the biodiversity in this ecosystem (Figure 14c, red line). When $d_{c1} < d < d_{c2}$, however, the concentrations of chemicals (AHLs and nutrients) experienced by cells varied significantly with their positions, which in turn could be affected by their motility. This effect led to a drastically reduced biodiversity with increasing cellular motility (Figure 14c, blue line). When $d > d_{c2}$, the interaction between the populations was extremely weak and cellular movement would have a negligible contribution to the interaction and biodiversity (Figure 14c, green line). When induced, the dominant interaction in our system was programmed predation by QS. Dr. Hao Song thus examined how the critical segregation distances (d_{c1}, d_{c2}) would change with diffusivity of the QS signals (D_{AHL}), and found that both d_{c1} and d_{c2} increased with the length scale of the chemical diffusion (d_L) (Figure 14d). The dependence curves divided the phase diagram in the "d_c–d_L"-parameter plane into three regions. In the upper and lower regions, motility had a negligible influence on biodiversity; in contrast, in the middle region, motility drastically influenced biodiversity (Figure 14d).

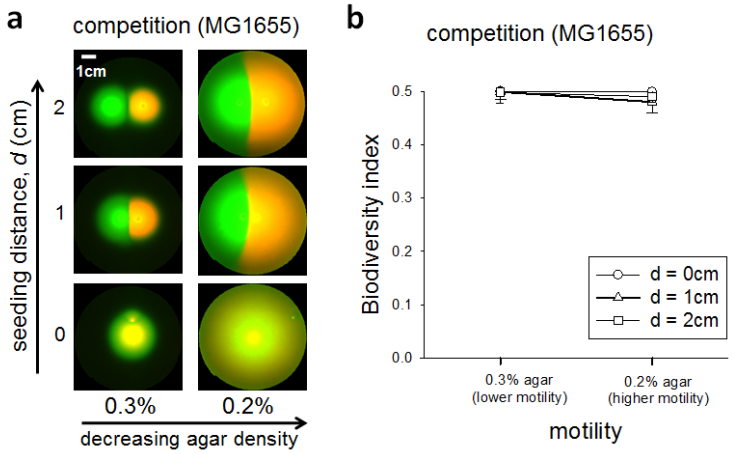

Figure 12: Spatial patterns and the corresponding biodiversity index resulting from the competition between two populations with similar growth rates and motilities. One population was MG1655 cells carrying Ptet-GFPuv(lva); the other was MG1655 cells carrying Ptet-mCherry. The experimental procedure was identical to that of Figure 7d. a) Typical patterns at varying segregation distances and in different agar densities. b) The BI was nearly independent of the segregation distance and agar density.

2.1.3 Significance

While chemical communication is widespread and central to many microbial ecosystems, it has been largely neglected in studies on the maintenance of biodiversity. It has been suggested that decreasing motility increases biodiversity in an ecosystem with contact-based interactions [99, 100]. However, our results suggested a more complex picture in a chemical-mediated system, where the biodiversity critically depended on the interplay between cellular motility (by diffusion and chemotaxis), chemical diffusion (of QS signaling chemicals and nutrients), and habitat configuration. Dr. Hao Song further developed a highly simplified, conceptual model to delineate how motility impacts cellular response at different segregation distances (Figure 15). The "R-

d" dependence revealed two critical segregation distances, d_{c1} and d_{c2} (logically similar to Figure 14b). When $d<d_{c1}$ or $d>d_{c2}$, motility had a negligible influence on the response. When $d_{c1}<d<d_{c2}$, however, motility drastically influenced the response.

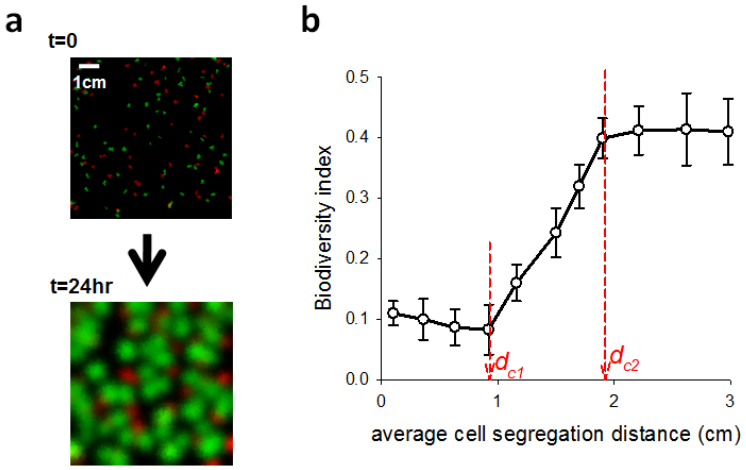

Figure 13: Two critical segregation distances (d_{c1}, d_{c2}) in determining the impact of motility on biodiversity, obtained from numerical simulation of the 2-D PDE model. a) Two-dimensional (2-D) snapshots of the predator (green) and the prey (red) density distributions at time zero and 24hr. b) The 2-D PDE model revealed two sharp transitions in the dependence of the BI on d, defining d_{c1} and d_{c2}. Below d_{c1} or above d_{c2}, d had a negligible influence on the BI. For $d_{c1}<d<d_{c2}$, the BI increased almost linearly with d. The spatially averaged BI was calculated at 24hr. The error bar was the standard deviation of three computations with different random number seeds.

In summary, motility's impact on biodiversity was determined by the relative magnitudes of the interaction length scale and the segregation distance between populations, as schematized in Figure 1c. If the interaction length scale was much longer or much shorter than the segregation distance, motility had little impact on biodiversity. Otherwise, motility would significantly impact biodiversity. In our system, the interactions were mediated by chemical diffusion, which had a longer length scale than

motility. The populations thus needed to be segregated sufficiently, but not too far, to manifest the effects of motility (Figure 14c). In contact-based ecosystems, however, interactions occurred by physical contact and their length scale was that of cellular motility, which was comparable to the segregation distance between cells. In this scenario, motility had a significant impact on biodiversity, which provided an intuitive interpretation of past studies on contact-based systems [99, 100]. Our conclusion held for other chemical-based interactions between two populations, including competition (Figure 9). It would be interesting to explore if this conclusion would also hold for ecosystems with many populations in further studies. If so, Figure 1c would represent a general, qualitative criterion that outlined the contribution of the three factors to biodiversity in a wide variety of ecosystems and that allowed for the classification of ecosystems based on the length scale of their interactions.

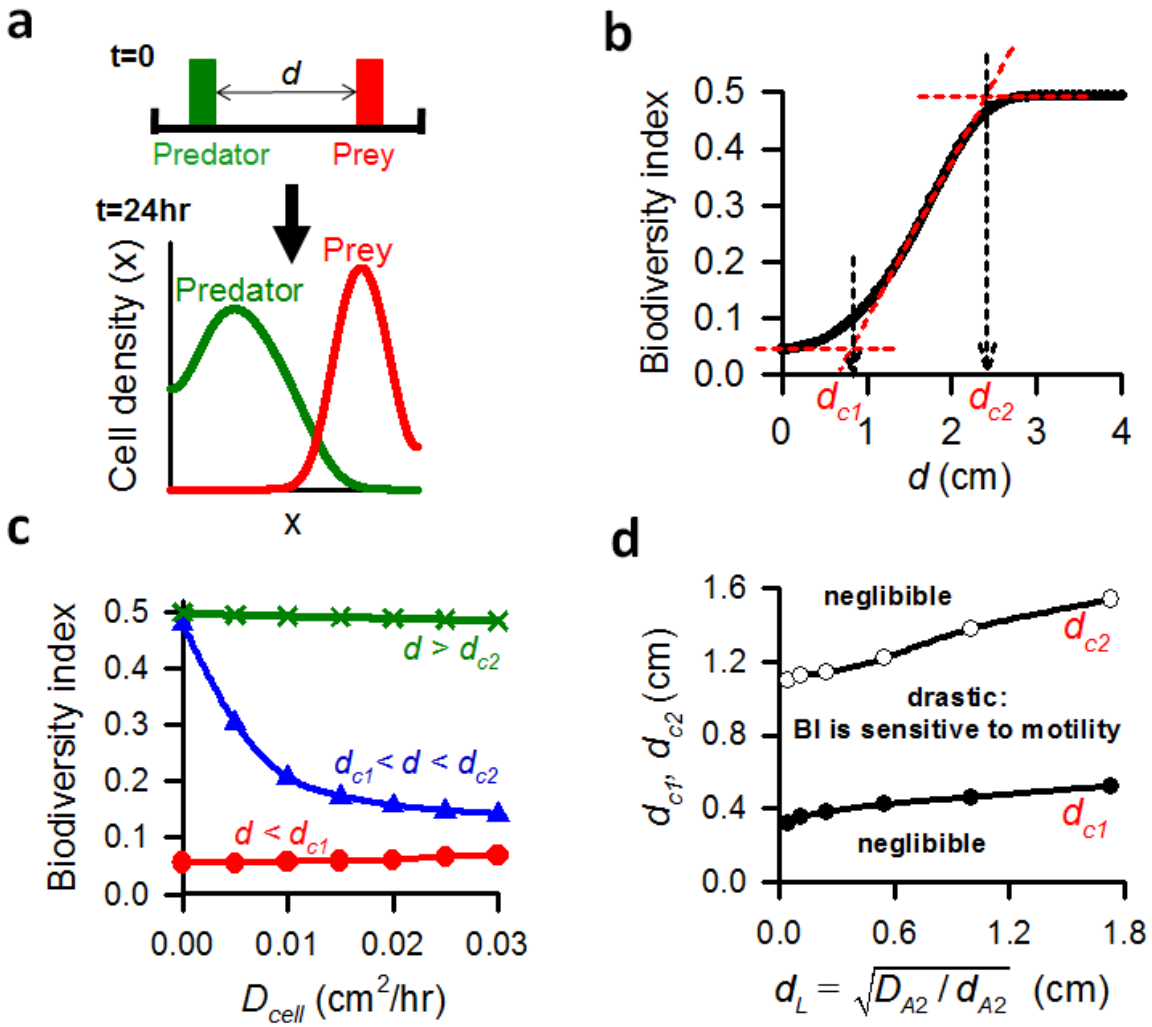

Figure 14: Two critical segregation distances (d_{c1}, d_{c2}) in determining the impact of motility on biodiversity. a) One-dimensional (1D) distribution of the predator (green) and the prey (red), which were seeded at two focal points with a distance d (upper panel). The bottom panel showed their density distributions after 24hrs, obtained from numerical simulation of the 1-D PDE model. b) The 1-D PDE model revealed two sharp transitions in the dependence of the BI on d, defining d_{c1} and d_{c2}. Below d_{c1} or above d_{c2}, d had a negligible influence on the BI. For $d_{c1} < d < d_{c2}$, the BI increased almost linearly with d. The spatially averaged BI was calculated at 24hr. c) For $d < d_{c1}$ or $d > d_{c2}$, cellular motility had a negligible effect on the BI. For $d_{c1} < d < d_{c2}$, the BI decreased almost exponentially with cellular motility. d) Both d_{c1} and d_{c2} increased with the characteristic length scale of the QS signal diffusion (d_L). d_L was defined by $\sqrt{D_{A2} / d_{A2}}$, where D_{A2} was the diffusivity of 3OC6HSL, and d_{A2} is the degradation rate of 3OC6HSL. The phase diagram was divided by the "$d_{c1, 2} \sim d_L$" curves into three

regions. In the middle region, the cellular motility would drastically influence biodiversity. In the upper and lower regions, cellular motility would have a negligible influence on biodiversity.

Efforts in engineering gene circuits have focused on pushing the limit in the ability to create systems with increasing complexity. The design of synthetic ecosystems represents a new frontier [83] and involves programming different types of cell-cell interactions, such as mutualism [20, 72], consensus [45], and predation [18, 72]. Consisting of well-characterized parts, these systems offer unprecedented flexibility to manipulate and analyze interactions between populations, as has been done in this work. The knowledge gained from such investigations may provide novel insights into naturally occurring ecosystem interactions. However, most studies in synthetic ecology have been confined to mimicking basic ecological interactions. Our study represents a significant advance in exploring ecological questions with a synthetic ecosystem.

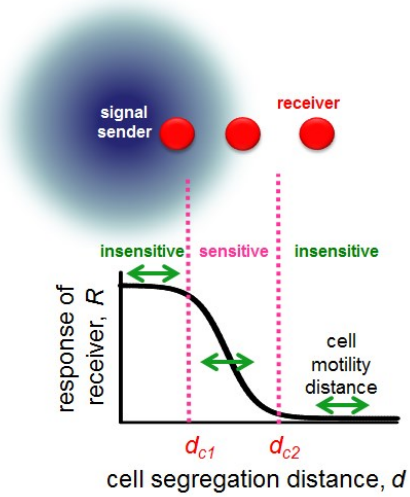

Figure 15: An abstract model delineated how cellular response (*R*) depends on the cellular segregation distance (*d*) in chemical-mediated ecosystems. The steady-state distribution of a chemical *A* satisfied a 1-D PDE: $D_A \partial^2 A/\partial x^2 - d_A A = 0$, with boundary conditions $A(0) = A_0$, $A(\infty) = 0$; where D_A was the diffusivity, and d_A was the degradation rate constant of *A*. The analytical solution to this equation was $A = A_0 e^{-\sqrt{d_A/D_A}\,x}$. The response of cells to *A* would be $R = A/(K_A+A)$, where K_A was the half maximum response. The double-headed arrow, labeled "cell motility distance," schematically represented a cell spreading distance (not to scale) by cell motility.

2.2 Supporting experiments

2.2.1 Supporting methods

2.2.1.1 Reagents and formula

***Liquid medium*:** The M9 liquid medium was made by following the protocols in reference [117], i.e., M9 salts were supplemented with the following components (concentration): dextrose (w/v, 0.5%, Fisher Biotech, ≥99.8%), 1 mM $MgSO_4$ (Sigma), 100 μM $CaCl_2$ (Sigma, granular, anhydrous, ≥93%), vitamin B1 (i.e., 1 μg/ml thiamine,

Carbiochem, hydrochloride), and 0.1% casamino acids (Teknova). The 2xYT medium was also made by following the protocols in reference [117]: 16 g tryptone (Difco Laboratories), 10 g yeast extract (Difco Laboratories), and 5 g NaCl (Sigma, ≥99.5%) were added to 1 L deionized H_2O. Both types of medium were buffered to pH=7 using 20.92 g/L MOPS (OmniPur, ≥99.0%) and KOH (EMD Chemicals) solution. To maintain the plasmids in the predator and prey cells, 50 μg/ml kanamycin (OmniPur, potency=750μg/mg) and 50 μg/ml chloramphenicol (Calbiochem) were added to the medium. Unless noted otherwise, Isopropyl β-D-1-thiogalactopyranoside (IPTG **1**, Omega Bio-tek) was applied at 1 mM and AHLs were applied at 100 nM when applicable.

***Solid medium*:** M9 and 2xYT (pH=7) agar were prepared by adding a certain amount of agar (Difco Laboraties) into M9 and 2xYT (pH=7) medium (above). The mixture was boiled by microwave and cooled at room temperature to ~50°C. 50 μg/ml kanamycin, 50 μg/ml chloramphenicol, 1 mM IPTG (when applicable), and 100nM AHL (when applicable) were then added to the molten agar. After vigorous mixing, 9 ml agar was poured into an 8cm-diameter Petri dish (BD Falcon). The agar was then kept on an even desk at room temperature for one hour for full solidification before use.

2.2.1.2 Solid-phase experiments and analysis

We performed the solid-phase experiments described in Figure 7d on 0.2% or 0.3% pH-buffered M9 soft agar. Upon melting and boiling agar by microwave and

cooling it down to ~50°C, 1mM IPTG and appropriate antibiotics were added into the molten agar and spread onto an 8cm-diameter Petri dish. Meanwhile, single colonies of the predator and the prey were inoculated respectively in 3ml liquid LB medium (with appropriate antibiotics, in 14ml test tube) and incubated in the shaker (250 rpm) at 37°C overnight until both cultures reached stationary phase. The cultures were then diluted to approximately the same optical densities (OD_{600} (200μl) ~ 0.55). After solidification of the M9 agar, 10μl of the prepared cultures of the predator and the prey cells were inoculated on the M9 agar surface with varying distance: 0 cm, 1 cm, or 2 cm. These agar plates were then incubated at 37 °C within a closed box with a small amount of water on the bottom (to keep moisture) for 20 hrs. We then used a fluorescent imager (Kodak Image Station 2000MM, Carestream Health) to measure the green and red fluorescence intensities (GFP emission filter was 465nm, RFP emission filter 555nm), which were approximately proportional to the predator density and the prey density, respectively. ImageJ (National Institutes of Health) [118] was used for data processing of the images. A calibration curve was used to relate the GFPuv and mCherry intensity signals to the predator and prey densities. The exposure times and maximum saturation levels for GFPuv and mCherry were 1 min and 2500 and 1 min and 1500, respectively. Figure 9a shows the pattern obtained using the same methods in the absence of IPTG. We observed that the pH of the solid culture did not vary significantly with position or time over the course of the experiment.

The plates in Figure 6b-d were prepared as described above for Figure 7d with 0.2% M9 (pH=7) soft agar without IPTG, with 1 mM IPTG, or with 1mM IPTG and 100 nM 3-oxohexanoyl-homoserine lactone (3OC6HSL) or 3-oxododecanoyl-homoserine lactone (3OC12HSL). Single colonies of the predator and the prey were inoculated as described above. The overnight cultures were diluted to OD_{600} (200μl) ~ 0.55, and 10 μl of each culture was added to the center of the appropriate plates. In addition, 10 μl of each culture were seeded 0.5 cm apart on a plate containing 1 mM IPTG. The exposure times and maximum saturation levels for GFPuv and mCherry were 1 min and 1000 and 1 min and 2500, respectively.

We performed the solid-phase experiments described in Figure 11b on 0.13% or 0.15% 2xYT (pH=7) soft agar. Upon melting and boiling agar by microwave and cooling to ~50°C, 1mM IPTG and appropriate antibiotics were added into the molten agar and spread onto a 4cm-diameter Petri dish. In addition, the molten agar was supplemented with 0.1 μg/ml anhydrotetracycline (aTc) to induce expression from the *tet* promoter in the predator. Meanwhile, single colonies of the predator and the prey (each in the Top10F′ strain) were inoculated respectively in 3ml LB medium (with appropriate antibiotics, in 14ml test tube) and incubated in the shaker (250 rpm) at 37°C overnight until both cultures reached stationary phase. The cultures were then diluted to approximately the same optical densities (OD_{600} (200μl) ~ 0.9). After solidification of the agar, 10 μl of the prepared cultures of the predator and the prey cells were inoculated on

the 2xYT agar surface with varying distance: 0 cm, 0.8 cm, or 1.6 cm. The agar plates were then incubated at 37 °C within a closed box with a small amount of water on the bottom (to keep moisture) for 36 hrs. The GFPuv and mCherry fluorescence measurements were then taken as above with an exposure time and maximum saturation of 1 min and 2500 and 0.2 min and 800, respectively. A calibration curve was used to relate the GFPuv and mCherry signals to the predator and prey densities. Figure 11c shows the pattern obtained using the same methods in the absence of IPTG.

2.2.2 Supporting Results

2.2.2.1 Spatiotemporal patterns resulting from competition

As noted in 2.1.2.1, when induced with IPTG, our system represents a combination of predation and competition (Figure 6a). Without IPTG induction, the dominant mode of interaction was competition. In this case, the qualitative aspects of biodiversity modulation depended on whether the two populations had similar growth rates.

2.2.2.2 Competition between two populations with significantly different growth rates

This corresponded to the case of the MG1655 pairs (Figure 6b-d) without IPTG induction, where the uninduced predator had a significant growth advantage over the uninduced prey (see lines labeled with –IPTG). Our experiments (Figure 9a-b) showed that, with sufficient habitat segregation (1cm or 2cm), the biodiversity increased with reduced motility. Motility was reduced by increasing agar density from 0.2% to 0.3% in

our experiments. As illustrated in Figure 9c-d, the simulated spatiotemporal patterns and the corresponding biodiversity indices matched well with the experimental results (Figure 9a-b).

2.2.2.3 Competition between two populations with similar growth rates

This feature was realized in the system consisting of two MG1655 strains, each constitutively expressing two different fluorescence proteins. One strain beared the plasmid Ptet-GFPuv(lva); the other Ptet-mCherry. These strains had similar growth rates in the liquid phase and similar spreading rates on soft agar. Without carrying the predator or prey circuits, the two strains only competed for nutrients in a co-culture. Similarly, for the predator-prey system implemented in Top10F' cells, the uninduced predator and the uninduced prey had similar growth rates (Figure 11a).

For these configurations, neither motility nor segregation distance had a significant impact on biodiversity (Figure 11c, e, and g (Top10F') and Figure 12 (MG1655)).

2.2.2.4 Diffusion and response of the AHLs in soft M9 agar

To estimate the diffusivities of the two AHLs (3OC6HSL and 3OC12HSL), we constructed two reporter strains, respectively. The 3OC12HSL reporter strain carried two plasmids: plac-lasRluxI (p15A, Kan^R) and plux-mCherry (ColE1, Cm^R). We noticed that the synthesis of the 3OC6HSL in this strain did not interfere with detection of 3OC12HSL. The 3OC6HSL reporter strain carried two other plasmids: plac-luxR (p15A,

Kan^R) and p*lux*-GFPuv (ColE1, Cm^R). The two detector cells were all implemented in the Top10 *E. coli* strain.

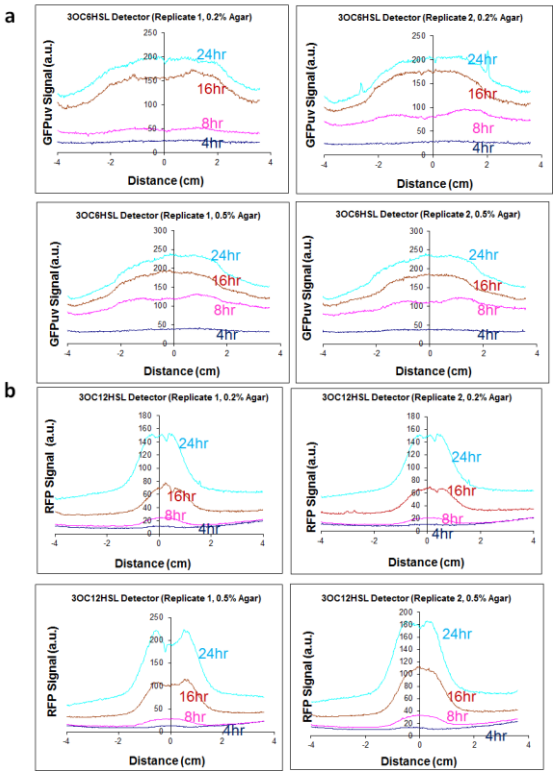

Figure 16: Diffusion of AHLs and response of reporter cells to the AHL gradient. a) GFPuv signal of 3OC6HSL-reporter cells in 0.2% (two replicates, top panels) and 0.5% (two replicates, bottom panels) M9 (pH=7) soft agar. b) mCherry signal of 3OC12HSL-reporter cells in 0.2% (two replicates, top panel) and 0.5% (two replicates, bottom panel) M9 (pH=7) soft agar.

We performed the solid-phase experiments described in Figure 16 on 0.2% or 0.5% M9 (pH=7) soft agar. Single colonies of 3OC6HSL and 3OC12HSL reporter cells were inoculated separately in 3ml liquid LB medium (with appropriate antibiotics, in 14ml test tube). For each AHL/reporter strain pair, upon melting and boiling agar by microwave and cooling to ~50^{o}C, appropriate antibiotics and 50 μl overnight culture of

the reporter strain was mixed with the molten agar and spread onto an 8-cm Petri dish. After solidification of the agar, 10 µl of 10 µM AHL solution was added at the center of the plate. At 4-, 8-, 16-, and 24-hour time points, green or red fluorescence images were taken using the Kodak Image Station 2000MM as described previously. The exposure times and maximum saturation levels for GFPuv and mCherry were 1 min and 1000 and 1 min and 3500, respectively. ImageJ (National Institutes of Health) was used for data processing of the images. For each image, a representative line was drawn across the diameter of the plate, and a plot depicting the green and red fluorescence intensities for each pixel along the line was developed.

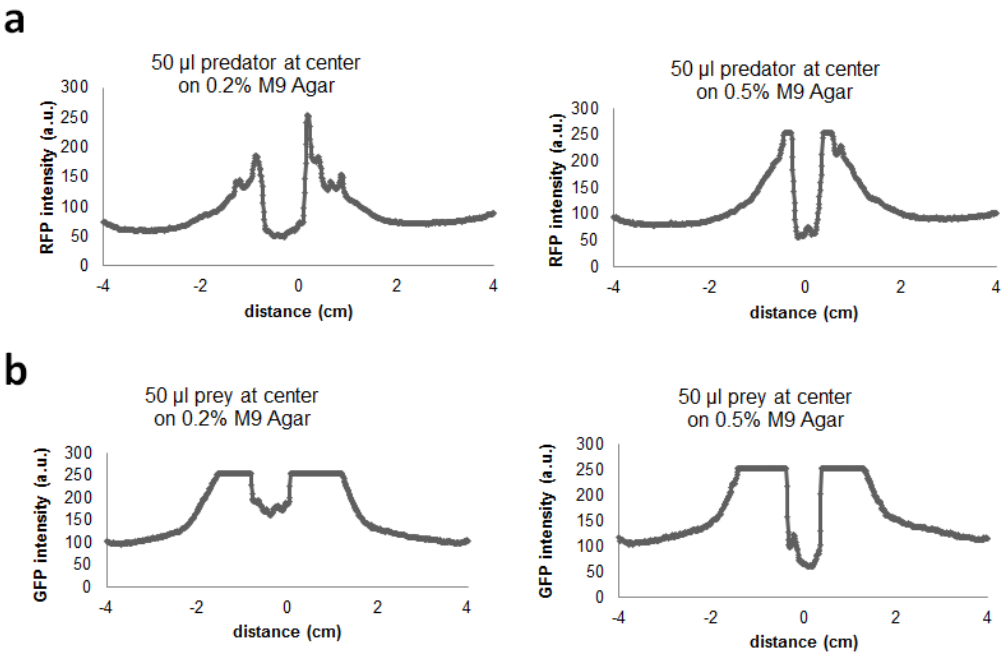

Figure 17: Response of AHL-reporter cells to the diffusion of AHLs produced by the MG1655 predator and prey cells. a) mCherry signal of 3OC12HSL-reporter cells in 0.2% (left panel) and 0.5% (right panel) M9 (pH=7) soft agar with 50 µl predator cells seeded in a small well at the center of the plate. The gradient in mCherry signal was

measured after 16 hrs of incubation. b) GFPuv signal of 3OC6HSL-reporter cells in 0.2% (left panel) and 0.5% (right panel) M9 (pH=7) soft agar with 50 µl prey cells seeded in a small well at the center of the plate. The gradient in GFPuv signal was measured after 16 hrs of incubation.

Using these reporter strains, we further characterized the diffusion of the signals produced by the predator or the prey (Figure 17) following similar protocols to those described above. Instead of AHL solutions, 50µl overnight culture of the predator or the prey was added to a small well at the center of the plate. The predator (or the prey) overnight culture was prepared by incubating a single colony of the predator (or the prey) in 3ml LB medium (with appropriate antibiotics, in 14ml test tube).

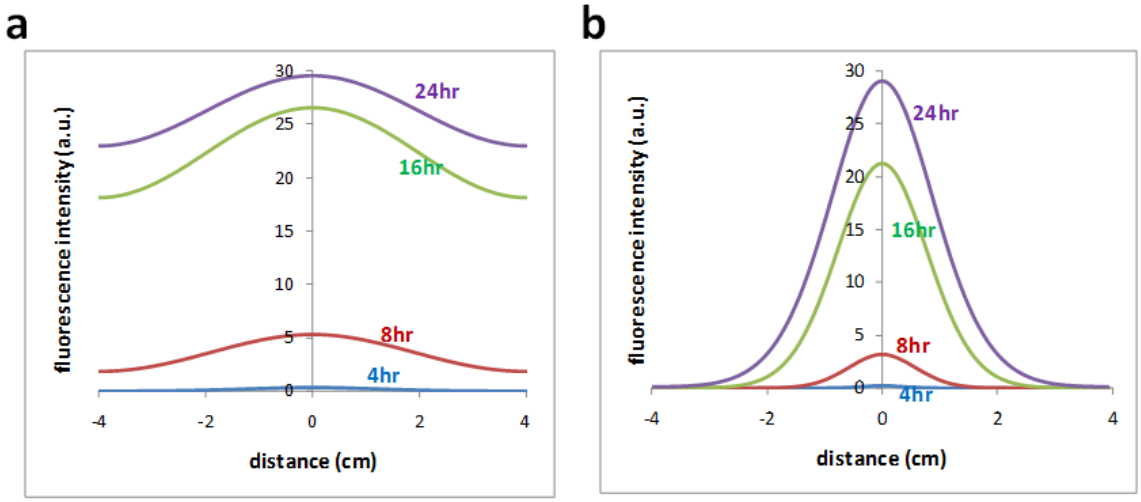

Figure 18: Estimating AHL diffusivities from the data in Figure 16. a) Simulated fluorescence intensity of the 3OC6HSL-reporter cells. The simulated profiles were consistent with the experimental data (Figure 16a). The estimated diffusivity of 3OC6HSL: $D_{3OC6HSL}$ = 0.4 cm²/hr. b) Simulated fluorescence intensity of the 3OC12HSL-reporter cells. The simulated profiles were consistent with the experimental data (Figure 16b). The estimated diffusivity of 3OC12HSL: $D_{3OC12HSL}$ = 0.03cm²/hr.

To simulate these experimental conditions (Figure 16), Dr. Hao Song built a simple mathematical model and ran simulations using biologically feasible parameters. By fitting the experimental measurement of the detector fluorescence profiles (comparing profiles in Figure 16a-b and Figure 18a-b, respectively), he estimated the diffusivities of the two AHL molecules: $D_{3OC6HSL}$ = 0.4 cm^2/hr and $D_{3OC12HSL}$ = 0.03 cm^2/hr.

3. Preliminary experiments targeting self-organized pattern formation

The goal of my main project was to implement self-organized pattern formation using bacteria containing a synthetic gene circuit. Such an endeavor, like any other in engineering, requires multiple designs, implementations, and characterization experiments. Understanding the importance of these processes in gaining valuable insights as to how to generate self-organized patterns, I will discuss some of the most critical preliminary experiments I conducted in this chapter. This chapter does not capture the entirety of the incredible amount of tinkering of experimental conditions and gene circuit designs as well as the sheer volume of preliminary data generated. However, it does demonstrate how I arrived at the final gene circuit design and experimental conditions which eventually gave rise to robust and reproducible self-organized patterns.

3.1 Motivation

From limb bud outgrowth [119] and feather development [30, 120] to hair follicle formation [121], pattern formation is a fundamental driver in the development of living organisms. A commonly invoked model to explain this phenomenon is the Turing model [122]. At the core of the model is the notion of local activation and long-range inhibition mediated by two diffusible molecules (morphogens): a slow-diffusing activator stimulates production of itself and a fast-diffusing inhibitor. Since its

conception, numerous computational studies have applied the Turing model to different biological pattern-formation processes. These studies have demonstrated the ability of this mechanism to generate highly versatile patterns in different contexts [123-129].

Despite its conceptual elegance, the relevance of the Turing model has been questioned since its initial proposal, due to the difficulty in identifying the specific underlying reaction mechanisms, particularly the morphogens. This issue has been alleviated as an increasing number of experimental studies have identified candidate morphogens that underlie vertebrate limb development [119, 130-132], skin pigmentation [127], and hair follicle spacing [121]. Yet, even in these well studied systems, the mapping between experiment and modeling is often vague. As such, the model in each context is largely used as a framework for a general demonstration of plausibility instead of offering specific predictions that can guide molecular-level experiments.

Furthermore, the formulation of the Turing model and its variants focuses on the characteristics of the synthesis and diffusion of the morphogens. In fact, the transport of morphogens has been mostly modeled as Fickian diffusion. Also, in this framework, the role of cell growth and movement has been largely neglected. In a general modeling framework, such simplifications are useful, but they are likely at odds with the specific mechanisms underlying development when pattern formation is often coupled with cell

proliferation [133, 134]. Recent studies in chicken and mice have shown that the morphogen responsible for specifying digit identity in the embryonic limb bud also regulates proliferation of limb mesenchymal cells, thereby controlling the number of digits that form [130-132]. In addition, since pattern formation is often coupled with cell fate determination [133], transient dynamics can have important consequences on spatial patterning. Due to the profound potential effect of transient temporal dynamics on cell fate, its contribution can be perpetuated into permanent spatial patterns as in the cases of limb patterning and somite segmentation [130, 135]. This process is fundamentally different from the steady-state patterns resulting from diffusive instability.

My goal was to take a synthetic-biology approach to examine the pattern-formation dynamics in engineered bacteria. This approach is advantageous due to its clear mapping between modeling and experiment, which facilitates the investigation of how circuit dynamics are modulated by experimentally tractable parameters. My hypothesis was that this approach will reveal the feasibility of biological pattern formation resulting from a mechanism analogous to the classical Turing mechanism but including unique features reliant on prolonged transient dynamics and regulated cell growth and movement.

3.2 Work flow for debugging biological systems

The work flow for this system, like the system itself, was highly nonlinear. There were not neatly ordered construction, testing, and assembly steps on the way to a

finished product akin to Henry Ford's assembly line. Instead, the project consisted of many rounds of repeated design and testing steps on the way to a finished product. On an abstract level, the work flow of the project can be summarized by the flow chart illustrated in Figure 19.

For each component of the system, I started with an initial design. I then went about constructing the designed component and testing it. If the test was a success, I moved on to the next step in the construction process on the way to system completion. However, if the test was not a success, I needed to go back to the drawing board and implement another design. While this latter process is arduous and tedious, it is absolutely essential in the programming of gene circuits at the current time, given the relative nascence of the synthetic biology field (see 1.8). In addition, the efforts put toward initial failed designs were never wasted because, upon witnessing these design failures, I was able to bring with me all of the lessons learned during the process to the next round of designing and testing, as well as all of the additional steps on the way to completion of the final system. Specifically, through the debugging process, I was able to develop data analysis tools (e.g., scripts to analyze movies, images, flow cytometry data, etc.), new skills (e.g., experimental protocols, mathematical expertise, etc.), biological insights (e.g., selective pressure on circuit components, metabolic nuances among growing populations, the dynamic interaction between the host organism and the gene circuit, etc.), and improved design goals (e.g., increased sensitivity of the gene circuit,

increased driving of the inhibition module, regular and reproducible microcolony growth, etc.). Each one of these lessons learned not only accelerated my progress in subsequent rounds of designing and testing of the system component in question but also in all other steps leading to the final system. In this manner, I viewed the green debugging feedback loop (Figure 19) as a positive feedback loop, which accelerated later progress on the system, rather than a negative feedback loop, which merely slowed down system development. I believe that the workflow of this system, which was applied to my system, can be generally applied to all synthetic biological systems at the present time.

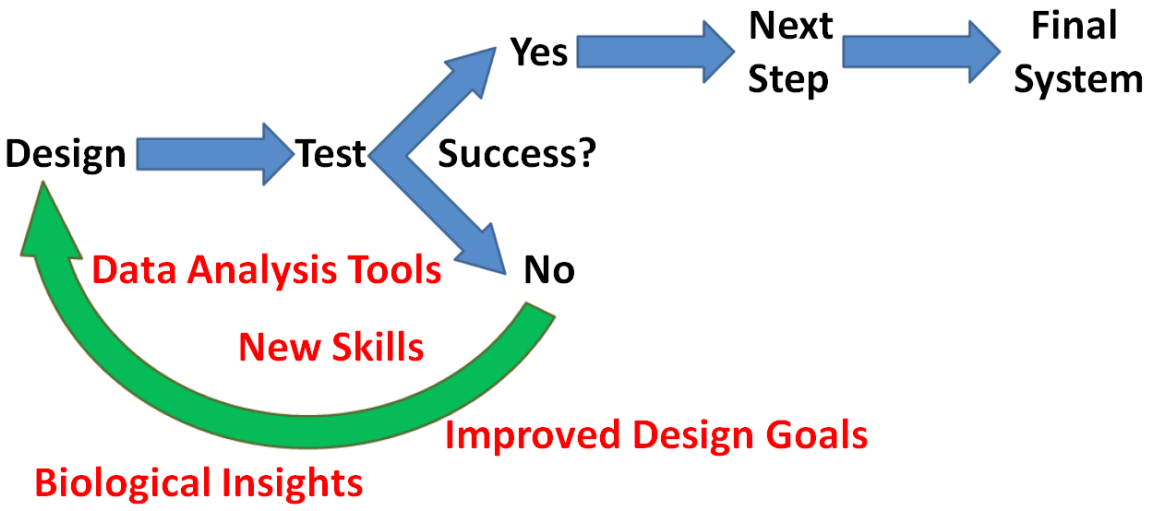

Figure 19: Work flow for the production of synthetic biological systems.

3.3 Gene circuit 1.0

3.3.1 Design

As shown in Figure 20a, our original gene circuit consisted of a mutant T7 RNA polymerase (T7 RNAP) activating its own expression via a T7 promoter carrying a *lac*

operator, as well as that of a quorum sensing system. T7-activated expression of LuxI leads to the synthesis of acyl-homoserine lactone (AHL), which can diffuse freely through the cell membrane and throughout extracellular space. When AHL binds to LuxR, the resulting complex can activate LacI expression. Sufficiently high concentrations of LacI can inhibit expression of T7 RNAP by binding to the *lac* operator. The design can thus be divided into two modules: an activation module consisting of the T7 RNAP positive feedback and an inhibition module consisting of QS-mediated LacI expression. Also, to report the circuit dynamics, a cyan fluorescent protein (CFP) and an mCherry protein are co-expressed with T7 RNAP and LacI, respectively.

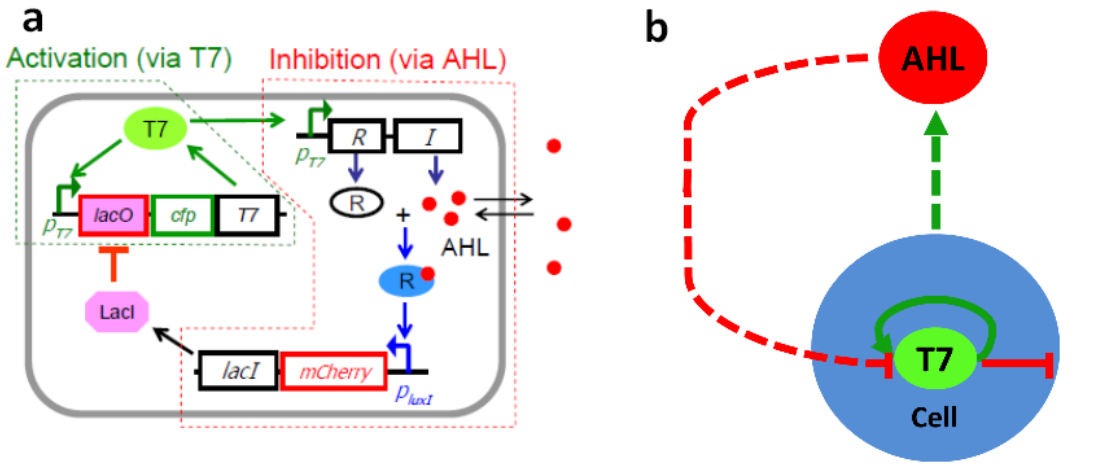

Figure 20: Schematic of the gene circuit used to realize pattern formation. a) The positive feedback is mediated by T7 RNA polymerase (T7). T7 leads to the activation of a diffusible signal (AHL, red dots), which serves as an inhibitor by controlling the expression of a Lac repressor (LacI). CFP and mCherry are co-expressed with T7 and LacI, respectively, as readouts of the programmed circuit dynamics. b) The circuit described in a) follows a design logic of short-range activation in which T7 activates itself and its own inhibitor, AHL, and long-range inhibition in which AHL inhibits T7. Physically, this short-range activation and long-range inhibition occurs because T7's cell-mediated diffusion occurs at a much slower rate than AHL's diffusion.

The basic logic of our circuit (Figure 20b) was the same as the Turing mechanism: AHL serves as the fast-diffusing inhibitor to realize long-range inhibition. In contrast, transport of T7 RNAP is mediated by cell movement, which is orders-of-magnitude slower than AHL diffusion. This realizes local activation. By design, however, our circuit is distinct from the classical Turing mechanism in two aspects. First, the cell-mediated T7 RNAP transport is more appropriately described as advection, instead of Fickian diffusion. Second, expression of T7 RNAP induces metabolic burden and inhibits growth of its host cell, which can enhance nonlinearity in the system [73] and facilitate pattern formation.

3.3.2 Materials and methods

3.3.2.1 Liquid Medium

The 2xYT medium was made following the protocol in [136]: 16 g tryptone (Difco Laboratories), 10 g yeast extract (Difco Laboratories), and 5 g NaCl, were added to 1 L deionized H_2O. The 2xYT medium was then buffered to pH=6.5 with KOH (EMD Chemicals) solution in 20.92 g/L MOPS (OmniPur, ≥99.9%).

3.3.2.2 Plasmids and cell strains

The entire circuit consisted of two plasmids: pTuLac2 CMR2 and pSCT7mut7. pTuLac2 CMR2 was constructed from the parent plasmids pLuxRI, pLuxmCherry, and pET15bLCFPT7. pLuxmCherry and pET15bLCFPT7 were used as templates for polymerase chain reactions (PCRs) which produced two DNA segments containing the

pLux promoter upstream of mCherry and LacI, respectively. The two segments were joined using overlapping PCR. The 5′ primer used to amplify the pLux promoter and mCherry contained an overhanging 16-base pair region constituting the pT7 promoter in the reverse orientation relative to the pLux promoter. The resulting PCR segment had EcoRI and AatII overhangs at the 5′ and 3′ ends, respectively. Both the PCR segment and pLuxRI were digested with EcoRI and AatII and ligated to yield pTuLac2 with kanamycin resistance and a p15A origin of replication (ori). The Kan^r gene was then removed and replaced with a Cm^r gene by digesting pTuLac2 and pLuxGFPuv (Cm^r) with SpeI and AatII and ligating the appropriate segments together. The resulting plasmid was named pTuLac2 CMR2.

pSCT7mut7 was constructed using pSC-CFPT7 as a parent plasmid which contained CFP under the control of the pT7 promoter and Lac operator. T7 RNAP was amplified via PCR from pAR1219. NheI and XhoI restriction sites were placed at the 5′ and 3′ ends of the PCR fragment, respectively. This DNA segment and pSC-CFPT7 were each digested with NheI and XhoI and ligated together, yielding pSCT7mut7. During the cloning process, a point mutation occurred in the T7 RNAP coding region, changing the 764^{th} amino acid from asparagine (Asn) to aspartate (Asp). Subsequent sequence analysis of several clones from later generations of cultures containing the plasmid revealed that after the cloning step, pSCT7mut7 remained genetically stable. The

primers used for each of the cloning steps can be found in Table 1. For all liquid and solid phase experiments, the plasmids were harbored in MC4100 (*lacI-*) cells.

Table 1: Primers used

Amplified Region	Direction	Sequence (5′→ 3′)
Reverse pT7-pLux-mCherry	Forward	ATTGAGAATTCTATAGTGAGTCGTATTATC ATGA GTCACACTATTGTATCGCTGGGAAT
Reverse pT7-pLux-mCherry	Reverse	ACATAGCCAGTAACTCGAGGCTAGCTAGT CAAGCTTTTACTTGTACAGCTCGTCC
LacI	Forward	ACTAGCTAGCCTCGAGTTACTGGCTATGTG ATAGCGCCCGGAAGAGAGTC
LacI	Reverse	ATTGCGACGTCCCTCGCCGAAAATGACCC AGA
T7 lysozyme	Forward	ACTAAGACGTCCGCCCAGTCCTGCTC
T7 lysozyme	Reverse	ACGGAGCTAGCGGAAAGGAGGAAAGAAA TAATGGCTC

3.3.3 Liquid phase characterization

The first step towards testing the circuit's behavior was to characterize it in the liquid phase. Although such characterization does not necessarily map to the circuit's behavior in the solid phase, it did at the very least give me a rough estimate of the circuit's dynamic range. These analyses can be split into two categories: parts characterization in which separate components of the circuit were tested for functionality and system characterization in which the whole circuit was tested for functionality.

3.3.3.1 Parts characterization

Before the full system was analyzed, it was necessary to confirm that both the activator and inhibitor modules were working properly separately. To verify their functionality, pTuLac2 CMR2 and pSCT7mut7 were transformed separately into BL21 DE3 Gold and DH5α pro cells, respectively. On its chromosome, the BL21 DE3 Gold strain contains a gene cassette which expresses T7 RNAP under the control of the *pLac* promoter. In addition, it also constitutively expresses LacI. For a diagram of the full testing construct, see Figure 21a. The BL21 DE3 Gold cells transformed with pTuLac2 CMR2 were grown up in 17 3-mL M9 cultures containing 50 μg/ml chloramphenicol, all originating from a single colony, at 30 °C for 16 hrs. Each culture contained varying amounts of both exogenously added AHL and Isopropyl β-D-1-thiogalactopyranoside (IPTG, a small molecule inhibitor of LacI protein). The mCherry expression from the cultures was then quantified in a Victor3 multi-well fluorimeter. The results from the experiment can be seen in Figure 21b. Here, the x- and y-axes represent the amounts of AHL and IPTG added, respectively. The corresponding color on the contour map indicates the resulting mCherry expression levels (a control strain not carrying a plasmid was used to subtract the background signal). As one can see, the system's mCherry expression increases with both increasing IPTG and AHL concentrations.

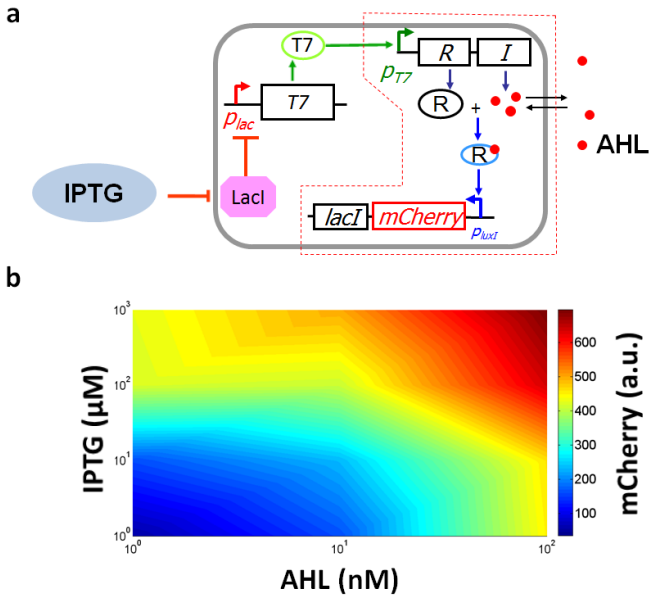

Figure 21: Testing of the inhibitor module. a) The gene construct utilized to test functionality of the inhibitor module. pTuLac2 CMR2 was placed in BL21 DE3 cells, which have T7 RNAP expression under the control of the *pLac* promoter as well as constitutive LacI expression. b) Profile of mCherry expression for varying concentrations of AHL and IPTG exogenously added to cultures derived from the same single colony.

These results indicated 1) that the inhibitor module's gene expression cascade is driven by T7 RNAP and 2) that the inhibitor module's gene expression is limited by AHL level. The first conclusion can be drawn since T7 RNAP expression is effectively activated by IPTG (cultures induced with 1000 μM IPTG showed a ~40-fold increase in mCherry intensity relative to those with no induction). Meanwhile, AHL is concluded to be the limiting reactant in the gene expression cascade since at each concentration of IPTG added, an increasing AHL concentration results in increased mCherry expression. This point is particularly important from a computational perspective since the modeling framework utilized (see Chapter 5) assumes that the inhibitor module's

activity in the solid phase can be modeled as a lumped term critically dependent on AHL.

Similarly, pSCT7mut7 was tested separately in DH5α pro (Invitrogen; Carlsbad, CA), a strain which constitutively expresses high levels of LacI (see Figure 22a for a diagram of the construct). A single colony of the transformed strain was inoculated in LB medium and grown overnight at 37 °C. The culture was then diluted 100-fold in 3-mL cultures containing M9 medium, 50 μg/ml kanamycin, and a varying concentration of IPTG. After 10 hours of cell growth, the absorbance (at a 600 nm wavelength) and CFP expression was quantified using the plate reader (a control DH5α pro strain not containing a plasmid was used to subtract background CFP signal). As Figure 22b illustrates, CFP expression increased significantly for cultures containing higher concentrations of IPTG (namely, 100 μM and 1000 μM). This result indicated that the activator module's gene expression was indeed repressed by LacI. Together with the inhibitor module results, these data indicated that both parts of the circuit were working as designed.

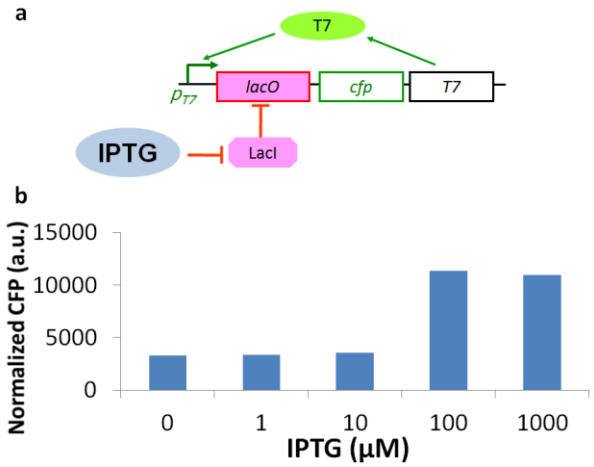

Figure 22: Testing of the activator module. a) The gene construct utilized to test functionality of the activator module. pSCT7mut7 was placed in DH5α pro cells, which constitutively express high levels of LacI. b) CFP expression normalized with cell density for varying concentrations of IPTG exogenously added to cultures derived from the same single colony after 10 hours of cell growth at 37 °C.

Furthermore, these preliminary experiments allowed for the estimation of some critical parameters. For example, for the experiment characterizing pTuLac2 CMR2, it is evident that the dynamic range of LacI synthesis is ~40-fold. In addition, for the experiment characterizing pSCT7mut7, the dynamic range of T7 RNAP inhibition by LacI is ~3-fold.

3.3.3.2 System characterization

Once it was clear that the parts were working as designed, I moved on to characterize the entire gene circuit's behavior. This was done during a summer internship at Los Alamos National Laboratory. There, I, along with a colleague, Dr. Kumkum Ganguly, conducted the following experiment: MC4100 cells derived from a single colony containing the gene circuit were grown in LB culture with 50 μg/ml

chloramphenicol and 50 μg/ml kanamycin added for 18 hours in LB at 340 RPM (due to the thin air at the high altitude) at 37°C. These cultures were diluted 100-fold into 2xYT medium (buffered at pH=6.5) with the appropriate antibiotics added and grown for 24 hours at 340 RPM at 30°C. At intermittent time points, flow samples were extracted from the culture, and an Amnis ImageStream flow system was used to analyze the samples. This system was identical to a conventional flow cytometry system with the additional capability of taking high-resolution fluorescent and brightfield images of cells flowing down the stream. Using these images, I then processed the data by averaging the fluorescent intensity values across the entire cell area for thousands of cell images using the ImageStream software.

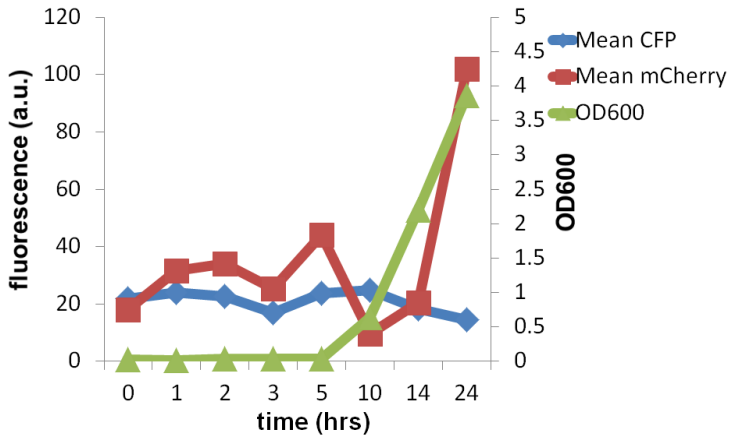

Figure 23: Mean CFP, mean mCherry, and OD600 measurements for various time points of cellular growth of a representative sample.

The circuit did indeed yield interesting temporal dynamics which were dependent on cell growth. As is evident in Figure 23, the circuit underwent many changes in mCherry and CFP expression levels over the course of cell growth. These

changes involved an increase in mCherry during lag phase, followed by a decrease in exponential phase, and finally a very large increase upon entering stationary phase. Correspondingly, CFP levels were constantly decreasing with the exception of the short time when mCherry was decreasing. These dynamics were intuitive when one examines the design of the gene circuit. When mCherry is high (t=2-3 hrs and t=24 hrs), CFP was decreasing because the protein co-expressed with mCherry (LacI) inhibits transcription of CFP (co-expressed with T7 RNAP). Likewise, when mCherry is low (t=10 hrs), CFP production increases. Note that there seemed to be a bit of a time-delay in these dynamics since at t=5 hrs, CFP production increases while mCherry still increases. This trend is likely due to the high stability of the mCherry protein.

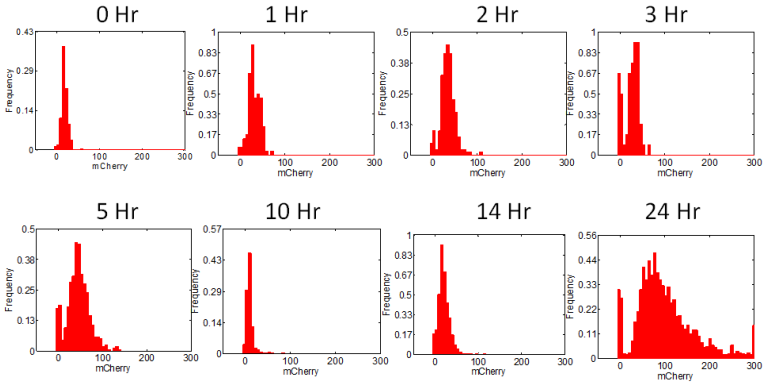

Figure 24: mCherry distributions for various time points of cellular growth of a representative sample.

While these population-level dynamics are certainly important to understand, we also wanted to understand the dynamics of the gene circuit on the single-cell level. As is evident in Figure 24 and Figure 25, the distribution of both fluorescent proteins

among the cell population is always bimodal. Furthermore, interesting, evolving correlations were found between the abundance of the two fluorescent proteins within the cell population (Figure 26). In addition, the modes and the fractions of cells surrounding each mode evolve as well. These phenomena can only be understood in the context of stochasticity. Such data indicated to us that a stochastic gene expression model would likely be appropriate for this particular gene circuit.

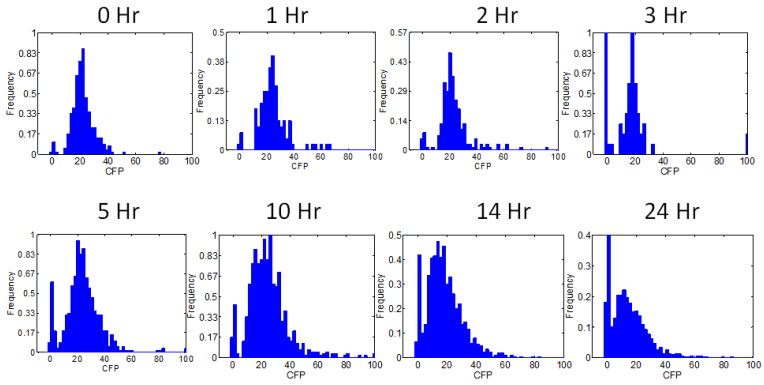

Figure 25: CFP distributions for various time points of cellular growth of a representative sample.

Most importantly, this type of system characterization suggested that when the parts were integrated together in the form the entire gene circuit, they seemed to interact in a manner consistent with the design logic. Considering the design to be a success (or so we thought), we moved on to solid phase characterization of the synthetic system.

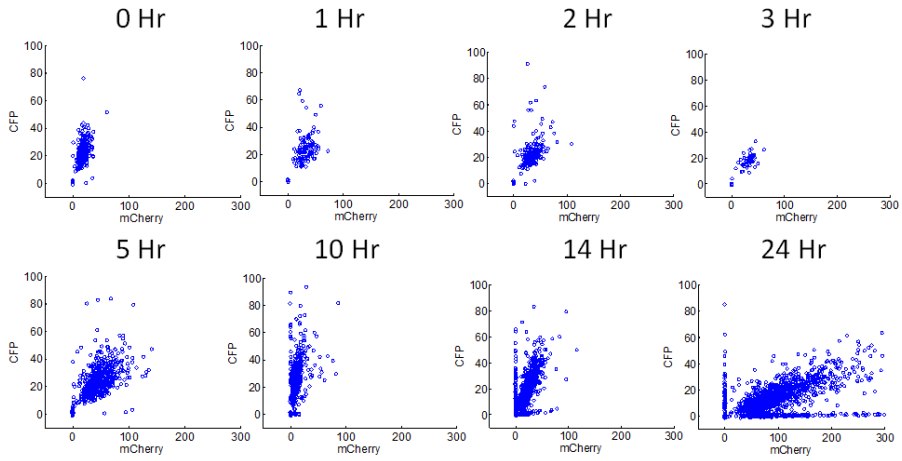

Figure 26: Scatter plot relating CFP and mCherry for various time points of cellular growth of a representative sample.

3.3.4 Solid phase characterization

Experimentation using a microchannel device confirmed the ability of the circuit to give rise to transient spots of high activator expression within a microcolony of growing *E. coli* containing the gene circuit. Overnight M9 cultures of MC4100 cells containing the gene circuit were prepared and grown to exponential phase (Absorbance~ 0.15-0.20). These cultures were then diluted 50000-fold in 0.13% 2xYT (pH=6.5) soft agar and 100 μl of the mixture was then added to a single channel on a 6-channel μ-Slide VI (Ibidi, Munich, Germany) of dimensions 17 mm by 3.8 mm by 0.4 mm with no laminar flow. A time-lapse movie was then prepared by imaging the daughter cells of initially sparse cells growing at 30 °C over 21 hrs and monitoring CFP levels (see Figure 27a for stationary frames of a typical time-lapse movie).

As is evident from Figure 27b, the spatiotemporal dynamics of both cell growth and CFP (reflecting intracellular activator concentration) reveal that the high CFP region

expands with the growth of the colony and is confined to the core region of the colony. However, the CFP intensity towards the center eventually decreases over time, finally converging to around the same level present at the periphery of the microcolony. We initially thought that this level is indicative of that of the true steady state. Thus, we thought that our study could be an examination of the transient pattern formation process in which the temporal dynamics of the colony core and colony front took different trajectories on their way to steady state (Figure 27b).

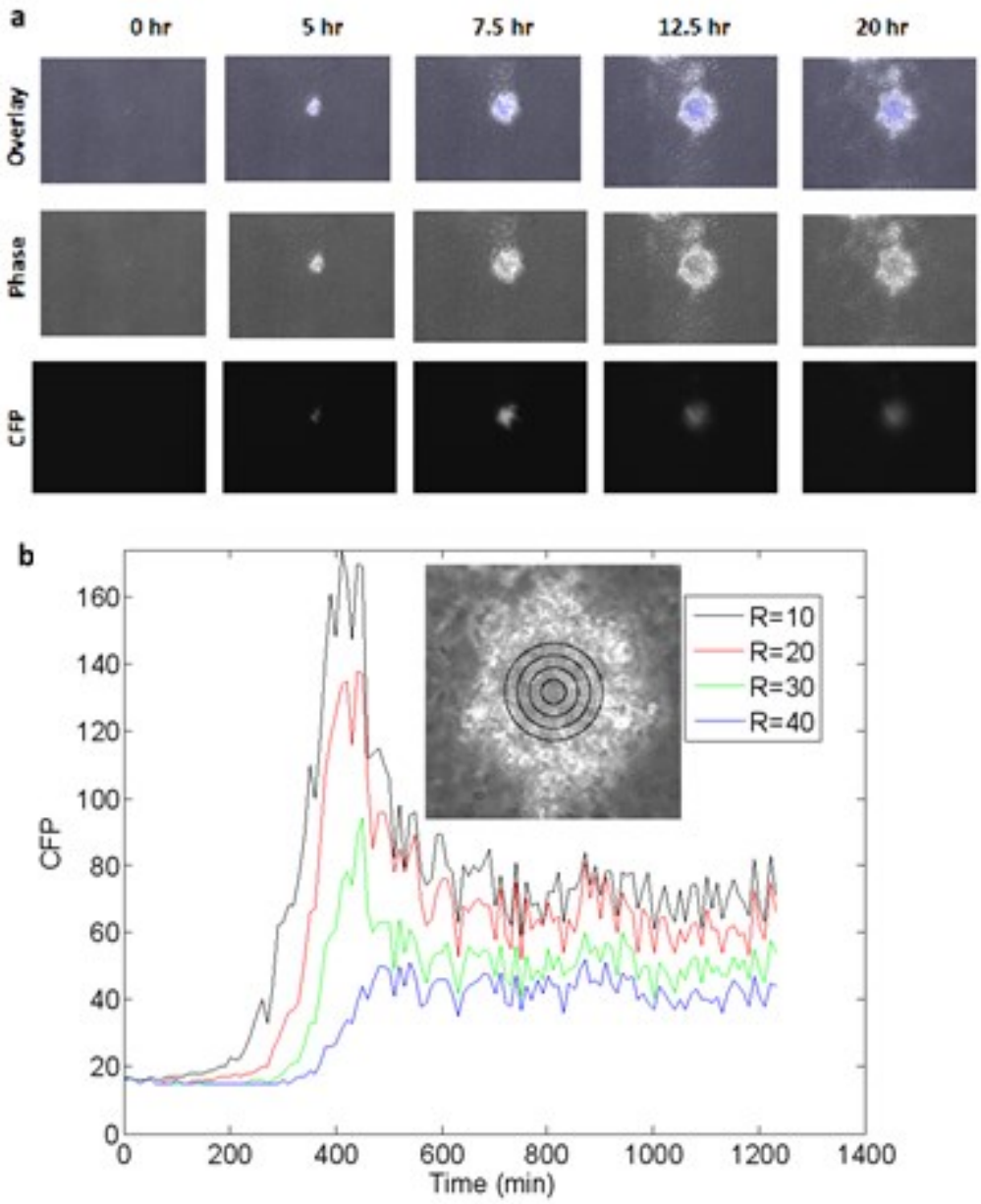

Figure 27: Experimental pattern formation. a) A representative time-lapse movie was taken after initial 1:50000 dilution of an M9 liquid culture of MC4100 cells containing the gene circuit (see Figure 20) in 0.13% 2xYT (pH=6.5) agar. The cells were grown up in a microchannel at 30°C for 21 hrs and imaged using a fluorescent microscope. The middle and bottom panels display the phase and CFP channels of various frames extracted from the time-lapse movie. The top panel displays the overlay of the phase and CFP images. b) Comparison of the evolution of CFP expression for various spatial locations within the microcolony in a). The average CFP levels are calculated

along concentric circles of varying radii centered at the origin of the cell microcolony over the course of 21 hours. The image displayed in the inset is a phase image of the microcolony at the final time with the various concentric circles used to measure spatial variability of CFP expression overlayed in black.

3.3.5 Conclusions regarding circuit design

Several problems were encountered in our further examination of the patterns formed in this manner. Specifically, mCherry never seemed to be activated significantly in the solid phase in this implementation (data not shown). In addition, further analysis of the parts characterization suggested that likely the activation module was not sensitive enough to LacI repression from the inhibition module in this setup. We came to this conclusion given that the activation module characterization experiment (Figure 22) suggested the sensitivity of the activation module to LacI repression to be only ~3-fold. In addition, from the solid-phase data, it seemed that the dynamic range of CFP signal was only ~2-fold from the maximum to steady state value in the microcolony core. Second, it was difficult to discern if differential CFP expression between the core and the rest of the microcolony was due to an actual pattern in intracellular fluorescence or was merely the result of higher cell density in the core region (this problem was later solved using confocal microscopy, but at the time was a critical concern of ours). Finally, in the microchannel device, we observed great variability in the spatiotemporal dynamics from microcolony to microcolony, replicate to replicate, and experiment to experiment. Again, this problem was later solved (via the use of multiwell chambers), but at the time led us to reconsider our gene circuit design.

3.4 Gene circuit 2.0

Given the problems we were encountering with the initial circuit design, we decided to move ahead with the construction of a beta version of the gene circuit. As discussed earlier, perhaps our biggest concern was that the activation module seemed to be insensitive to LacI inhibition at the transcriptional level. An alternative method for inhibition of T7 RNAP was to sequester T7 RNAP using the protein inhibitor T7 lysozyme. Specifically, T7 lysozyme can form a complex with T7 RNAP, rendering it unable to activate further transcription of itself. The perceived advantages of this design were two-fold: 1) the binding of T7 RNAP to T7 lysozyme was known to be very tight and effective [137, 138] and 2) protein inhibition via sequestration had given rise to a desirable, ultrasensitive response in gene expression in a previous system [139]. With these advantages in mind, I went ahead with the construction of a second version of the gene circuit.

3.4.1 Design

This gene circuit was exactly the same as the previous gene circuit with the exception that T7 lysoyzme was cloned in the place of LacI. The new circuit diagram is displayed in Figure 28. The plasmid harboring the new inhibition module of the gene circuit was constructed on a single plasmid using the following steps: T7 lysozyme was amplified from pLysS (Novagen; Madison, WI) using PCR with a 5′ primer containing an AatII overhang and a 3′ primer containing an NheI overhang (all primers used in this

study can be found in Table 1). Upon digestion of pTuLac2 CMR2 (see 3.3.2.2) and the PCR product with NheI and AatII, a ligation reaction was performed to yield the final plasmid, pTuLys2 CMR2.

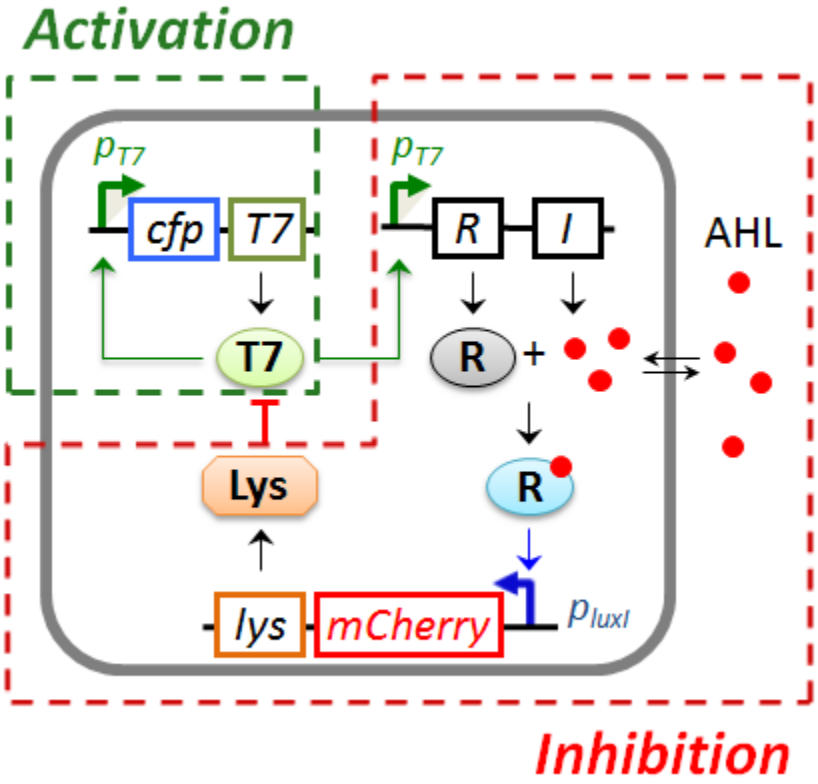

Figure 28: Full circuit diagram. The activation module (green dashed box) is mediated by a mutant T7 RNA polymerase (T7), which activates itself by binding its own promoter. T7 leads to the activation of the protein LuxR (R) and a diffusible signal (AHL, red dots). AHL can diffuse freely inside and outside the cell wall. When enough intracellular AHL accumulates, AHL binds R efficiently, giving rise to a transcriptional activator complex. This complex activates expression of T7 lysozyme (Lys), which inhibits T7. Thus, the quorum-sensing mediated expression of the T7 inhibitor, Lys, constitutes the inhibition module (red dashed box). CFP and mCherry are co-expressed with T7 and Lys, respectively, as readouts of the programmed circuit dynamics.

3.4.2 Validation of T7 lysozyme's inhibition of the activation module

3.4.2.1 The use of two versions of the activation module

Before going ahead with the cloning process described in 3.4.1, I first verified T7 lysozyme's inhibition of the activation module. Since the potential design issues were not confined to the inhibition module, two activation module plasmids were used in this dose-response experiment. The first activation module was the one described previously which was harbored on the plasmid pSC7mut7. The second activation module was previously characterized [73] and harbored on the plasmid pET15bLCFPT7.

This plasmid implemented the same logic displayed in Figure 28 but had two critical differences from the first activation module. First, pET15bLCFPT7 is a higher-copy plasmid than pSCT7mut7, meaning that more copies of the plasmid will be replicated within a cell. Thus, everything else being constant (i.e., synthesis and degradation rates, half-activation concentrations, etc.), more copies of the proteins encoded on the plasmid (including T7 RNAP) would be produced on pET15bLCFPT7 than on pSCT7mut7. We viewed this feature positively since it seemed that mCherry was not getting sufficiently activated by the activation module (3.3.4). Although having a higher-copy number did not guarantee that this would solve the problem, if indeed T7 RNAP synthesis was boosted on the higher-copy plasmid and T7 RNAP was the limiting step in mCherry production, then mCherry synthesis would be increased using pET15bLCFPT7.

Second, pET15bLCFPT7 had a different version of the T7 RNAP than was present on SCT7mut7. As mentioned previously, SCT7mut7 contained a mutation in T7 RNAP (764 Asn→Asp). The literature indicated that this mutation was located in the pinky specificity loop subdomain involved in promoter binding [140]. Knowing that previous attempts at cloning yielded other T7 RNAP mutants with mutations in DNA binding domains, we hypothesized that the strength of the T7 RNAP positive feedback loop was too strong with wild-type T7 RNAP, resulting in toxic levels of T7 RNAP (and possibly other downstream genes) in the cell. This growth constraint likely resulted in evolutionary selection of a mutant T7 RNAP which gave rise to a weaker positive feedback loop. Similarly, when cloning wild-type T7 RNAP into pET15bLCFPT7, Dr. Cheemeng Tan of the You lab, independently identified a different T7 RNAP mutant carrying a different mutation: a single deletion at the 186th base pair. However, the gene was still expressed as functional T7 RNAP, which likely resulted from a programmed translational frameshift [73]. I hypothesize that such a deletion likely occurred due to the same evolutionary pressures evident in my cloning process. In any case, we thought that at the very least, the use of the two plasmids would give us two different conditions (each with their own copy numbers and mutant T7 RNAP properties) with which to test for T7 lysozyme inhibition of the activation module. The idea here was that two conditions were better than one.

3.4.2.2 The experiment

Both activation modules were tested for inhibition in response to T7 lysozyme. Each test was conducted by comparing the CFP expression of cells in liquid culture containing the corresponding activation module plasmid (Figure 28, green dashed box) in a BL21 DE3 cell chassis with or without the pLysS plasmid in response to a varying input of IPTG concentration. The BL21 DE3 cell chassis expresses T7 RNAP from a lacUV5 promoter, which is inducible by IPTG. The pLysS plasmid constitutively expresses T7 lysozyme.

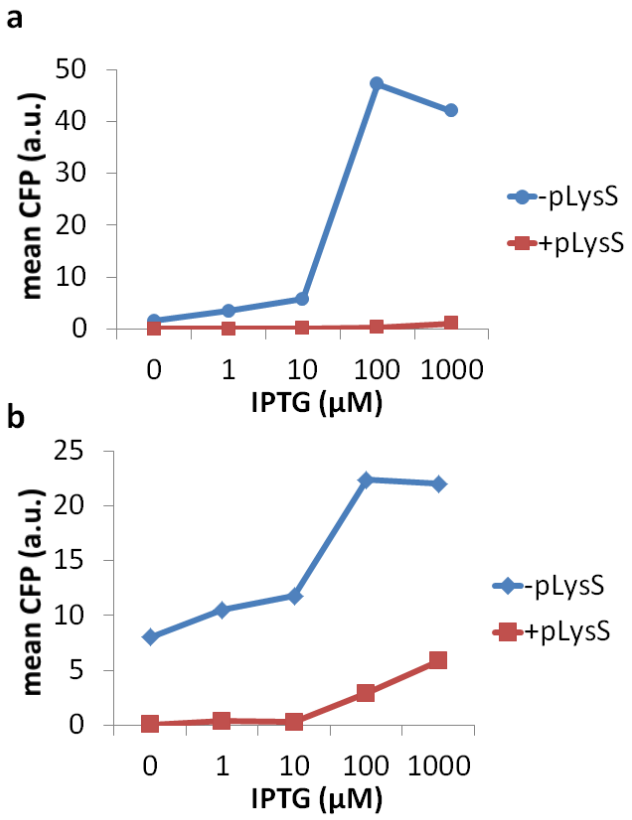

Figure 29: Test for lysozyme inhibition of two activation modules. For each activation module version, pET15bLCFPT7 (a) and pSCT7mut7 (b), two 3-ml overnight LB

cultures derived from two single BL21 DE3 colonies transformed with the corresponding activation module plasmid and with or without pLysS were prepared. Those cultures each were diluted 1:100 in 5 3-mL 2xYT (pH = 6.5) cultures supplemented with 0, 1, 10, 100, and 1000 μM IPTG, respectively, in addition to 50 μg/ml chloramphenicol and 75 μg/ml carbenicillin. The resulting cultures were incubated at 30 °C. After 8 hrs of incubation, the cultures were diluted 1:10 in PBS, and 1 μl diluted sample was applied to a 1% agarose PBS slab on a microscope slide. Cells were imaged using a Leica DM16000B fluorescence microscope with a mercury excitation lamp at 100X objective in both the phase and CFP channels. For the CFP measurements, the excitation filter was set to 436/20, and the emission filter was set to 480/40. Average CFP intensities over cell area were obtained for cells spanning three separate frames for each culture condition using a custom MATLAB algorithm described previously [73]. The mean CFP levels of the cells are displayed for varying IPTG concentration with (red) and without (blue) pLysS. For each cell included in the data analysis, background was subtracted based on the mean intensity of several hundred BL21 DE3 untransformed cells prepared in the same manner.

For each activation module, at each IPTG concentration, the mean CFP expression level of the cells containing pLysS is dramatically lower than that of the cells without the plasmid (Figure 29). This result indicated that the T7 lysozyme expressed from the pLysS plasmid is indeed decreasing T7 RNAP expression as designed. Furthermore, this effect was observed across a large span of IPTG induction levels, indicating that inhibition of the activation module occurs over a wide range of gene expression levels. This result is again consistent with the circuit design.

3.4.3 Replacement of the activation module and cell chassis

However, the inhibition by T7 lysozyme appeared to be more effective for the pET15bLCFPT7 activation module (Figure 29) than for the pSCT7mut7 activation module. For instance, for IPTG levels of 0, 1, and 10 μM, no leaky expression of CFP was identified above background fluorescence levels for pET15bLCFPT7, whereas some

leaky expression was identified for pSCT7mut7. In addition, at 100 and 1000 μM concentrations of IPTG, the ratios between CFP expression without pLysS and with pLysS for pET15bLCFPT7 were 152 and 38, respectively, whereas the same ratios for pSCT7mut7 were 8 and 3.76, respectively. These results indicated that the dynamic range of T7 RNAP's gene expression in response to T7 lysozyme inhibition was significantly greater for pET15bLCFPT7 than for pSCT7mut7. Furthermore, additional characterization of pET15bLCFPT7 (e.g., demonstration of activation by T7 RNAP and IPTG induction, the Hill coefficient, etc.) was conducted previously, eliminating the need for more preliminary experiments [73]. These advantages led to the replacement of pSCT7mut7 with pET15bLCFPT7 as the activation module.

From this point forward, the full gene circuit consisted of MC4100Z1 cells transformed with pET15bLCFPT7 (carrying the activation module) and pTuLys2 CMR2 (carrying the inhibition module). MC4100Z1 was chosen as the cell chassis over the previously used MC4100 because the Z1 component integrated into the chromosome expressed high levels of LacI. In this manner, the addition of IPTG could potentially be used to tune the synthesis rate of T7 RNAP, which still contained a *lac* operator upstream in pET15bLCFPT7. Thus, the flexibility of tuning T7 RNAP synthesis via the exogenous addition of IPTG without changing the cell background (MC4100 is genetically identical to MC4100Z1 with the exception of the presence of Z1) was viewed as a positive feature, and MC4100 was replaced with MC4100Z1.

3.4.4 Solid phase characterization using microchannels

At this point, with sufficient characterization of the gene circuit in the liquid phase, I decided to characterize the latest version of the gene circuit in the solid phase. I did this by observing the growth and gene-expression spatiotemporal dynamics of microcolonies containing the gene circuit in the same microchannel device described earlier (see 3.3.3). Here, varying amounts of agar were added to 2xYT (buffered at pH=6.5) liquid medium and appropriate antibiotics and IPTG were added. With these conditions, I ran into many of the problems I saw before in terms of variability from colony to colony, replicate to replicate, and experiment to experiment. However, whatever the condition and specific dynamics, there seemed to be spatial clustering of differential expression of mCherry and CFP throughout each of the microcolonies (Figure 30).

This observation was encouraging since it meant 1) that mCherry expression was now detectable in the solid phase and 2) that different spatial locations seemed to have different gene expression dynamics (the hallmark of pattern formation). These were two properties that we were hoping to achieve. With this success, the final problem I had to solve was dealing with system variability. This was done by changing the reactor type from a microchannel device to a multiwell chamber.

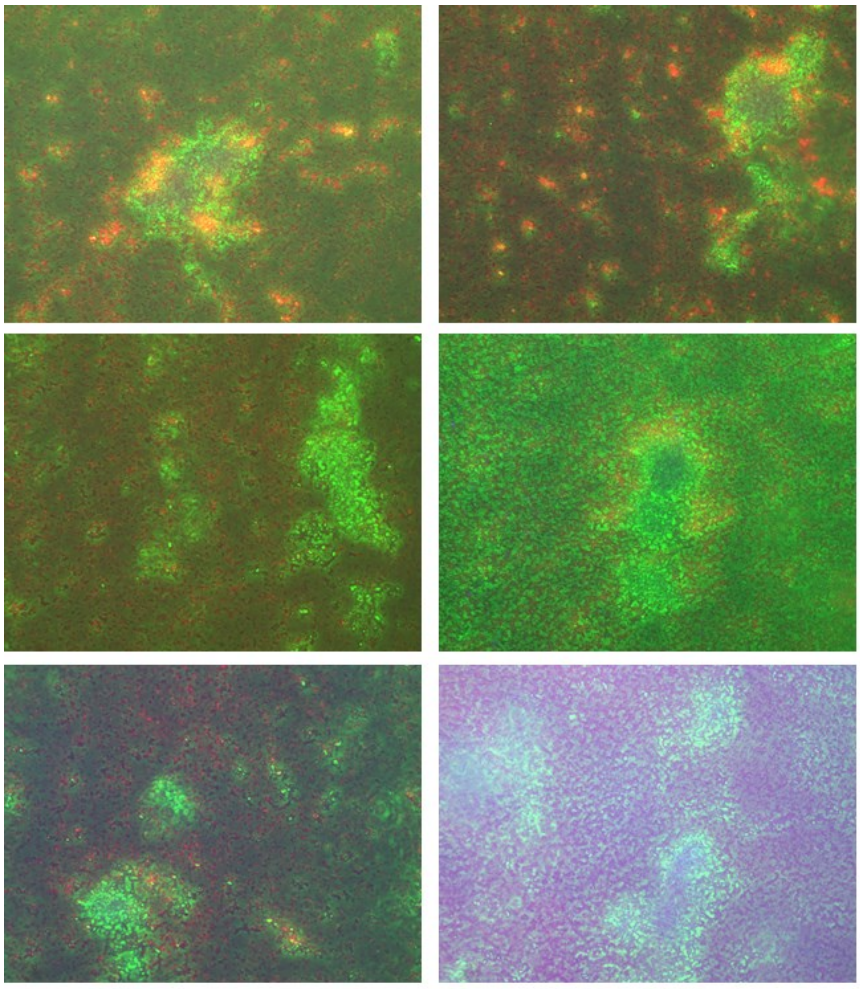

Figure 30: Montage of patterns obtained using microchannels. Raw 1.7 mm X 1.4 mm composite images of patterns obtained for cells in microchannels, derived from three different single cell colonies, spanning three independent experiments. Here, green represents the phase channel; red represents the RFP channel; and blue represents the CFP channel. Each pattern was imaged after 26-28 hours of incubation.

3.4.5 Solid phase characterization using multiwell chambers

3.4.5.1 The rationale for choosing the multiwell chambers

As discussed in 3.4.4, the goal was to reduce variability within the system. Two of the main hypothesized contributions to the variability with the microchannel device

were 1) varying distance from the microchannel reservoirs and 2) varying preferential locations for cell growth. The first problem occurred because the reservoirs contained thicker layers of agar than the microchannel. As a consequence, more cells were present in the reservoir, resulting in higher AHL in those regions. Thus, the closer a cell resided towards the edge of the reservoir, the more likely it was to have higher mCherry expression. This led to variability in cell behavior depending on the distance from the residing cell to the reservoir. In addition, this distance-dependent variability was not quantitatively consistent from sample to sample. Second, cells seemed to grow differentially well in different spatial locations. Obviously, some of that variability resulted from different gene expression dynamics that were derived from a given colony's distance from the reservoir. However, even for similar distances, there was widespread variability in cell growth, especially when comparing the edges (which cells seemed to attach to preferentially) with open locations.

I believed that the multiwell chambers would reduce such variability. The first source of variability would be eliminated by adding small soft agar droplets to the chambers and encapsulating the droplets on both sides with two glass coverslips. In this manner, the thickness of the agar would be relatively uniform, leading to an approximately equal probability of cell seeding across the droplet as well as a homogenous AHL spatial distribution. In addition, by using a small droplet that did not

reach the edges of the well chamber, I thought that I could avoid potential preferential clustering of microcolonies in the x-y direction.

3.4.5.2 The multiwell chambers

Five-µl droplets of .13% agar in 2xYT (buffered at pH=6.5) containing very dilute cells carrying the gene circuit were placed at the center of each of the 8 wells on the CultureWell™ multiwell chambered coverslip (Grace Bio-Labs, Bend, OR). For a schematic of the dimensions of the device, see Figure 31.

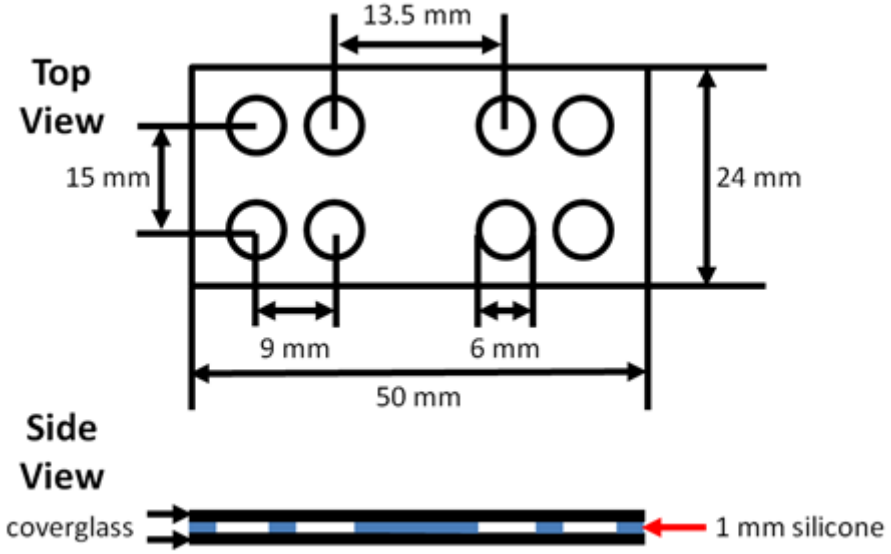

Figure 31: Schematic depicting the dimensions of the CultureWell™ multiwell chambered coverslip used in the experiment. Note that another coverglass was placed on top of the multiwall chambered coverslip (side view) to engulf the soft agar droplets. In addition, a silicone flap in the x-direction was excised using a razor blade.

3.4.5.3 Early experiments using multiwell chambers

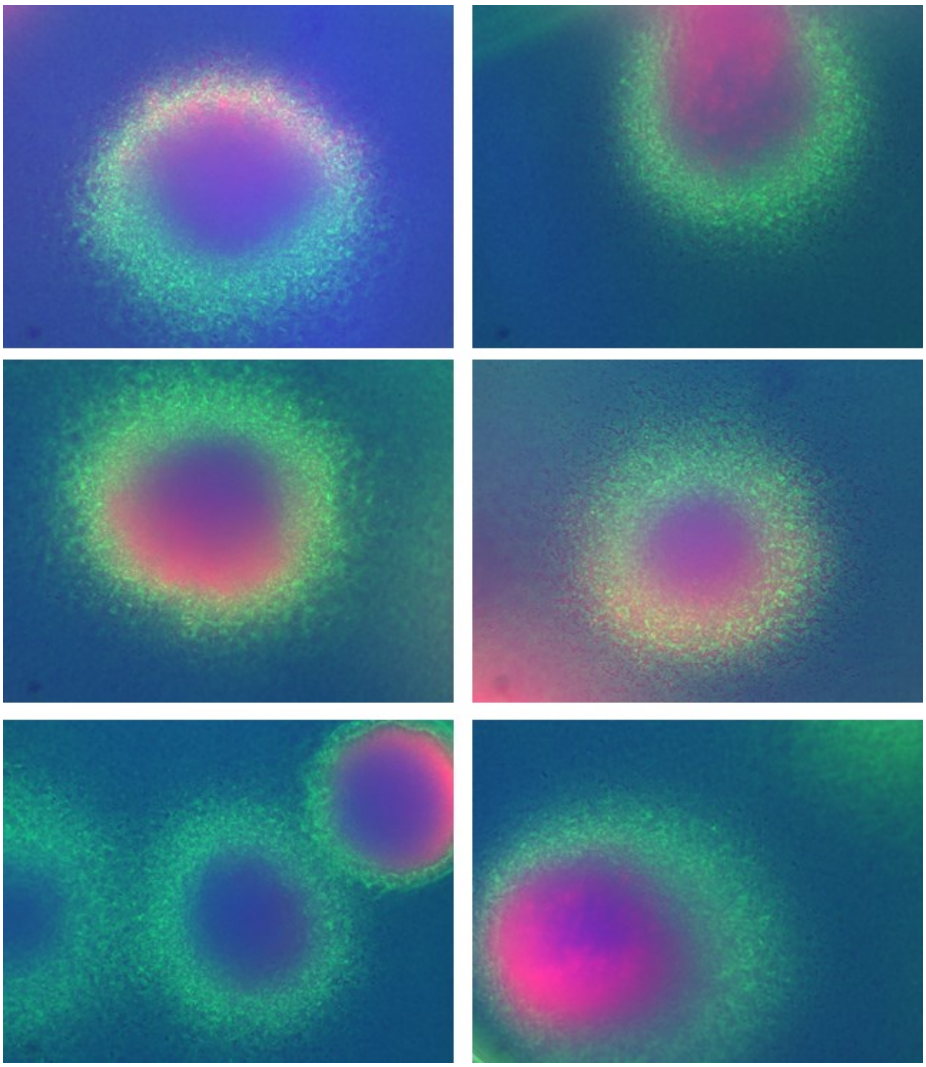

Figure 32: Montage of patterns obtained using microwell chambers. Raw 1.7 mm X 1.4 mm composite images of patterns obtained for cells in microwell chambers, derived from two different single cell colonies. The color scheme is as described in Figure 30. Each pattern was imaged after 28.5 hours of incubation.

In my first experiment using these conditions, I was able to observe very regular cell growth and relatively consistent gene expression dynamics from microcolony to microcolony and well to well, which indicated that much of the variability present in the

microchannel device had been eliminated. For a collage of such patterns, see Figure 32. In further experiments, I noticed that for very low initial dilutions of cells (approximately 1-4 per droplet), a pattern consisting of high CFP and high mCherry in the core and high mCherry in a ring configuration on the outer edge of the microcolony emerged (Figure 33).

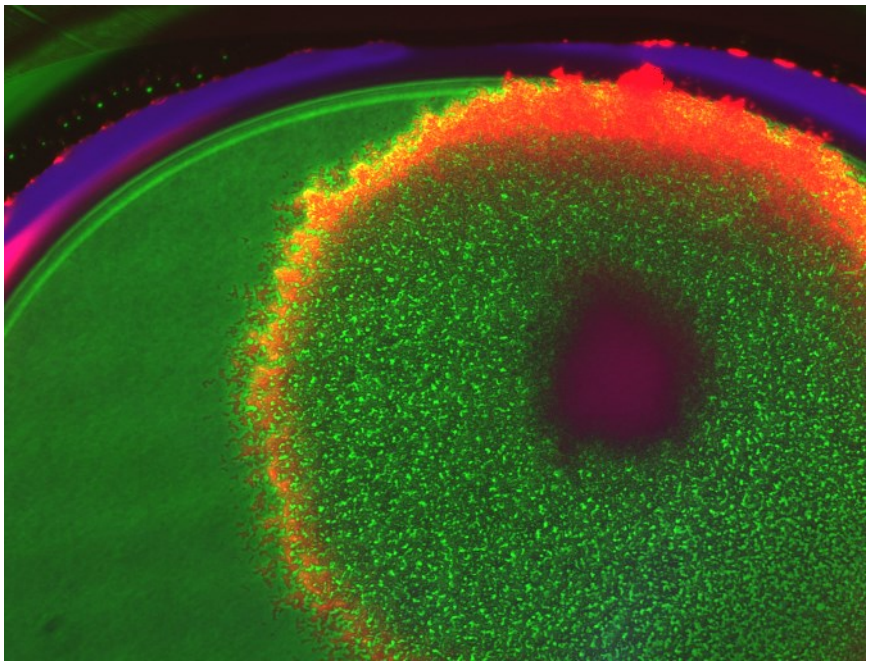

Figure 33: A pattern emerged at a very low dilution of cells in the microwell chamber. The pattern consisted of high CFP and mCherry in the core and high mCherry at the colony edge in the form of a ring.

3.5 General design principles for self-organized pattern formation

In 3.2, I discussed the value of the debugging process in the development of synthetic biological systems. One of the important takeaways from this process was improved design goals. Here, I believe that a few of my improved design goals can be

generally applicable to any engineer hoping to implement pattern formation via a synthetic biological system. Upon reflection, the first requirement of pattern formation is to ensure that the system is indeed capable of achieving different, distinguishable cell states. Luckily, I was able to achieve these different cell states with my first implementation of the gene circuit (Figure 26). While these states need not be stable, it is desirable if the states occur simultaneously within a single population so as to ensure that the cell state does not merely change temporally but also has the capability of changing in the spatial domain.

Once this first requirement is met, the system can theoretically give rise to patterns. However, one can maximize that capability by ensuring that the system is ultrasensitive to dynamic changes in gene expression. In my system, I did this by moving from Gene Circuit 1.0 to Gene Circuit 2.0. Specifically, T7 lysozyme replaced LacI in order to obtain greater sensitivity of the activation module to inhibition. In addition, greater protein production from the inhibition module was achieved by driving the inhibition module with an activation module containing a stronger T7 RNAP positive feedback loop. In this manner, the system's behavior was acutely sensitive to circuit dynamics. Furthermore, transitions between cell states can be driven by differences in global gene expression dependent on the configuration of growing cells as well as gene circuit dynamics (Chapter 5).

Finally, in addition to these design goals for the gene circuit, it is also important for any engineer attempting to implement pattern formation to achieve reproducible and predictable cell growth from experiment to experiment. This difficult problem is often underappreciated in theoretical studies on pattern formation but must be solved by any biological engineer tackling pattern formation. Without reproducible and predictable cell growth, one cannot quantitatively characterize patterns. Without such quantitation, it is very challenging, if not impossible, to obtain regular, symmetric patterns (3.4.4 and 3.4.5), to formulate a mechanism driving the pattern formation process (Chapter 5), and to extrapolate pattern trends in response to experimentally tunable parameters, such as initial morphogen levels and domain size (Chapter 6).

4. Robust demonstration of self-organized pattern formation using engineered bacteria

Upon further tuning of the experimental conditions, I developed a protocol for implementing reproducible and robust self-organized pattern formation using bacteria containing the latest version of the gene circuit (3.4). The system, while successful in its implementation of self-organized pattern formation, did not behave as we initially envisioned. First, pattern emergence was tightly coupled with cell growth. Second, the pattern was not defined by the length scale of the AHL (morphogen) gradient. Both of these features are often overlooked and underappreciated in Turing and other models of self-organized pattern formation. In this manner, the motivation for exploring the dynamics of our synthetic pattern-forming system changed according. The work described in this chapter has been submitted for publication: Payne S, Li B, Schaeffer D, You L. "Temporal control of self-organized pattern formation without morphogen gradients in engineered bacteria." Manuscript under review in *Molecular Systems Biology*.

4.1 Motivation

Many mechanisms have been proposed to explain natural pattern formation processes, such as slime mold aggregation [28, 29], feather branching [30], and tissue stratification [31, 32]. Regardless of the specifics, the majority of these mechanisms invoke morphogen gradients, which are either predefined [141, 142] or generated as part of the patterning process [121, 122, 143]. However, using our synthetic system, I can

demonstrate the generation of robust, self-organized ring patterns of gene expression in the absence of an apparent morphogen gradient. Interestingly, our modeling and experimental tests show that the temporal dynamics of the global morphogen concentration serve as a timing mechanism to trigger formation and maintenance of these ring patterns, which are readily tunable by experimentally controllable environmental factors. This mechanism represents a novel mode of pattern formation that has implications for understanding natural developmental processes.

4.2 Overview of the gene circuit

Our circuit (Figure 28 and Figure 34a) consists of a mutant T7 RNA polymerase (T7 RNAP) [73] activating its own expression via a T7 promoter carrying a *lac* operator. T7 RNAP also activates expression of LuxR and LuxI. LuxI mediates synthesis of acyl-homoserine lactone (AHL), which can diffuse across the cell wall. When enough AHL accumulates in cell culture, intracellular AHL binds to and activates LuxR, which induces expression of T7 lysozyme. Lysozyme can inhibit T7 RNAP by forming a complex with it and preventing it from binding its cognate promoter (Figure 29). To report the circuit dynamics, a cyan fluorescent protein (CFP) is co-expressed with T7 RNAP, and an mCherry protein is co-expressed with T7 lysozyme. The circuit can thus be divided into two modules: an activation module consisting of the T7 RNAP positive-feedback loop and an inhibition module consisting of quorum-sensing-mediated lysozyme expression. Its logic resembles that of the classical Turing mechanism [122,

143]: activation is local since T7 RNAP is confined in the cells, whereas inhibition is global due to fast diffusion of AHL.

However, our circuit differs from the classical Turing mechanism in two critical aspects. First, in contrast to the Turing mechanism, which utilizes two diffusible morphogens, our circuit only contains a single morphogen: the AHL molecule. T7 RNAP transport is cell-mediated and thus not driven by Fickian diffusion, which is assumed to take place in most reaction-diffusion models describing pattern formation. While underappreciated in theoretical studies, this mechanism of activator transport is likely common in natural developmental processes, such as stripe formation and limb bud outgrowth [128, 144-146]. Second, circuit activation induces a metabolic burden on the growth of its host cell. This metabolic burden is critical for enhancing the nonlinearity in the system [73] and exhibiting microcolony size control, which in turn facilitate robust pattern formation. Therefore, our circuit defines a tight coupling between intracellular gene expression, signal diffusion, and modulation of cell growth and motility. This coupling is often neglected in variants of Turing models invoked to explain self-organized pattern formation; yet, it is likely critical for diverse natural developmental processes, ranging from limb bud outgrowth [147] to somitogenesis [148] to tissue stratification [31].

4.3 Experimental demonstration of pattern formation

To explore the spatiotemporal dynamics of our system experimentally, we used a microchannel device (Figure 31) to culture microcolonies initiated from individual *E. coli* cells programmed by our gene circuit. Briefly, we added serially diluted overnight culture to molten soft agar containing growth medium supplemented with the appropriate antibiotics and 1000 μM IPTG (see Figure 35 for more details). Five-μl droplets of the agar containing about 1-4 *E. coli* cells were then placed into wells of the microchannel device. We then observed the growth and gene expression of the expanding microcolonies in each well at 30 °C.

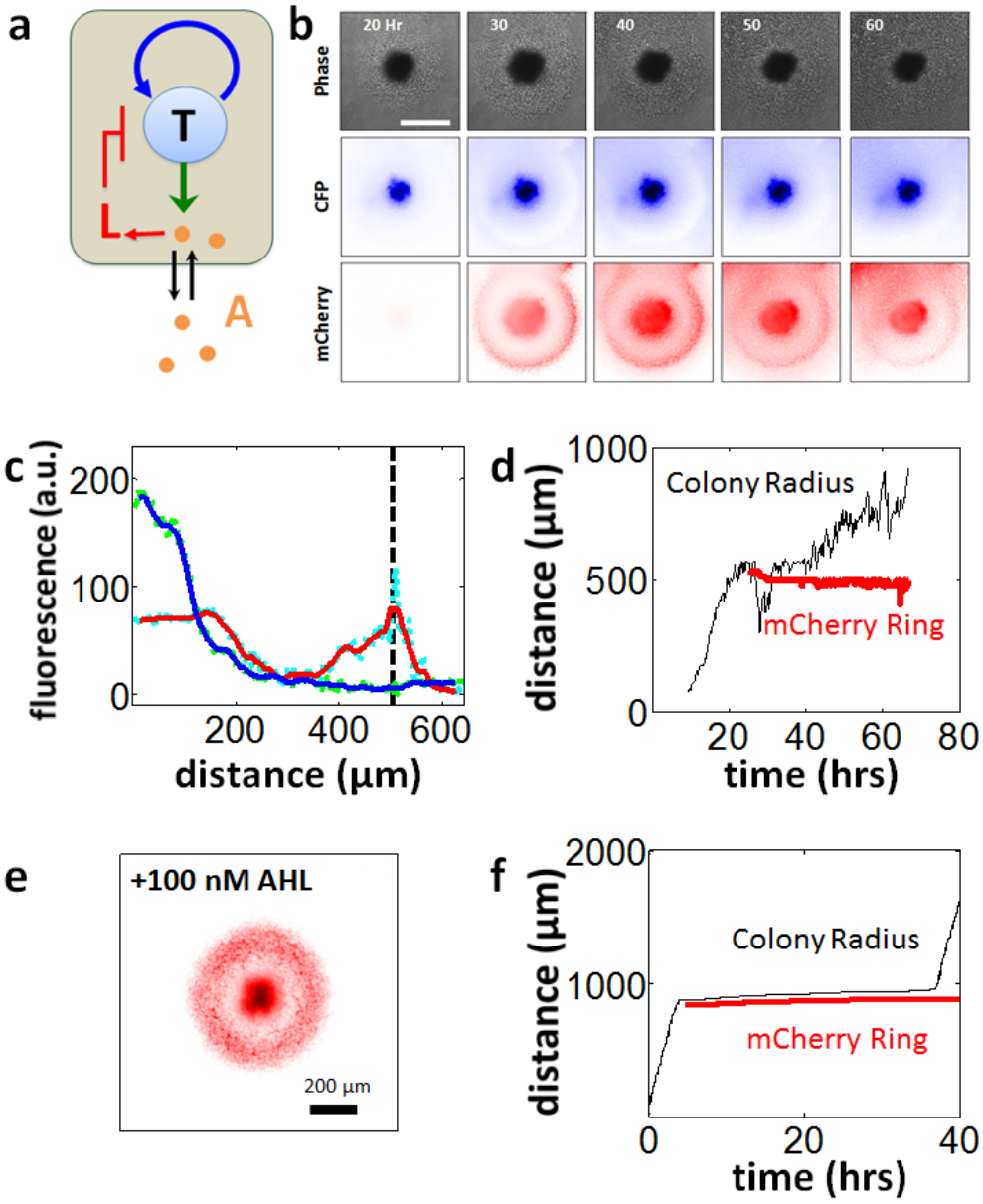

Figure 34: Self-organized pattern formation in engineered bacteria. a) Circuit logic. Our circuit consists of an activator T7 RNAP (T) activating itself and a diffusible signal, AHL (A). AHL can lead to repression of the activator by inducing T7 lysozyme (L) (see Figure 28 for a more detailed circuit diagram). b) The engineered bacteria developed a self-organized ring pattern. Images of a 1.2 mm X 1.2 mm field after 20, 30, 40, 50, and 60 hours of incubation (as labeled). The microcolony was imaged using a Leica DM16000B fluorescence microscope with a mercury excitation lamp at 5X objective in the phase (1st row), CFP (2nd row), and RFP (3rd row) channels. For the CFP

and RFP images, the color scheme is defined by the darkest blue and darkest red representing saturation in the CFP and RFP channels, respectively, and white representing background levels. The phase images are raw images; the white scale bar on the 20-hour phase image indicates a length scale of 500 μm. c) CFP (green dots) and mCherry (cyan dots) at the 30th hour at varying radial distance from the center. The solid blue and red lines are the running averages of the CFP and mCherry intensities, respectively. The black dashed line indicates the radial distance at which the running average of mCherry intensity is maximal outside of the core. This distance is defined as the mCherry ring radius plotted versus time in d). Intensity values were calculated as the average intensity values across all angles at fixed radii about the microcolony core center. Each of these intensity values had background signal subtracted. This processing was carried out using a custom MATLAB algorithm. d) mCherry ring radius (red line) and colony radius (black line) over time. The mCherry ring radius was calculated as described in c). The colony radius was calculated as the distance from the center of the microcolony core to the microcolony edge averaged across angles spanning π/6 to π/4. Both computations were performed using a custom MATLAB algorithm. e) mCherry image in the presence of 100 nM AHL. An mCherry bullseye pattern, albeit smaller pattern, still occurs after initial exogenous addition of 100 nM AHL. These data suggest that an AHL morphogen gradient is not necessary to obtain the mCherry bullseye pattern. The image is prepared as described in b) row 3. f) mCherry ring radius (red line) and colony radius (black line) over time. The base parameter set for the 1D simulation is listed in Table 2. See Chapter 5 for details. The y-axis is distance from Δ=0. Processing of the simulated data was done in the same way as for the experimental data in d).

Figure 34b shows growth and gene expression dynamics in a representative microcolony, which gives rise to a self-organized pattern with a length scale of ~500 μm. The pattern consisted of a CFP core and an mCherry ring (Figure 34b-c), whose formation appeared to be tightly coupled with colony expansion. Prior to 30 hours of incubation, CFP slowly accumulated in the microcolony interior before mCherry underwent a switch-like transition from a low state to a high state in a ring pattern in less than 5 hours. Initiation of the mCherry ring was concurrent with a pause in colony expansion (Figure 34d). Though colony expansion resumed after ~20 hours, the ring size

was maintained (Figure 34d) for ~35 hours (until the end of the experiment). During this time, the intensity of the ring gradually decreased (Figure 34b), suggesting that formation of the ring resulted from transient circuit dynamics. As indicated by additional results acquired under similar conditions, the dominant features of the self-organized patterns were robust and reproducible (Figure 36).

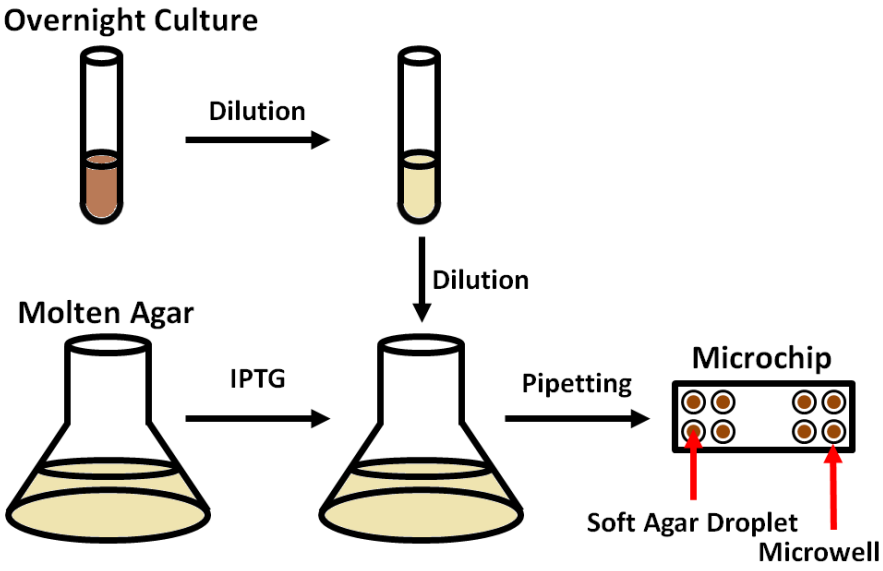

Figure 35: Experimental setup for pattern formation demonstration. The experimental results displayed in Figure 34 were obtained after using the following protocol: A 3-ml LB culture derived from a single colony of MC4100Z1 containing the full gene circuit is grown for 12 hrs at 37 °C. Molten agar is prepared by microwaving 0.07% w/v agar in 2xYT (pH=6.5) liquid medium. While this solution is cooling, the cell culture is diluted to ~0.2 Absorbance as measured by the Victor3 multi-well fluorimeter (Perkin Elmer, Waltham, MA) (600 nm absorbance filter, 0.1 sec). Using 0.2 Absorbance as a baseline, cultures were diluted another 3000-fold. Meanwhile, the molten agar was supplemented with 50 μg/ml chloramphenicol, 75 μg/ml carbenicillin, and 1000 μM IPTG. Then, the diluted culture was again diluted 500-fold into the molten agar. Eight 5-μl droplets of the cells mixed with the soft agar were then placed at the center of each of the 8 wells on the CultureWell™ multiwell chambered coverslip (Grace Bio-Labs, Bend, OR).

These results were counterintuitive considering the kinetic properties of the "morphogen" AHL. It is a small molecule with an estimated diffusivity of 0.4 cm^2/hr [19]. On the time scale of our experiments (~50hrs), the diffusion length scale is ~9 cm, which is about 2 orders of magnitude greater than that of our observed patterns. However, at the very early stage, AHL may form a transient gradient that could be critical for forming the pattern. To test this notion, we cultured cells in the presence of an initial AHL concentration of 100 nM, which eliminated the possibility of a significant and steep early gradient. Even under this condition, the microcolony was able to generate a similar (albeit smaller) pattern, confirming the ability of the system to generate patterns without an AHL gradient (Figure 34e).

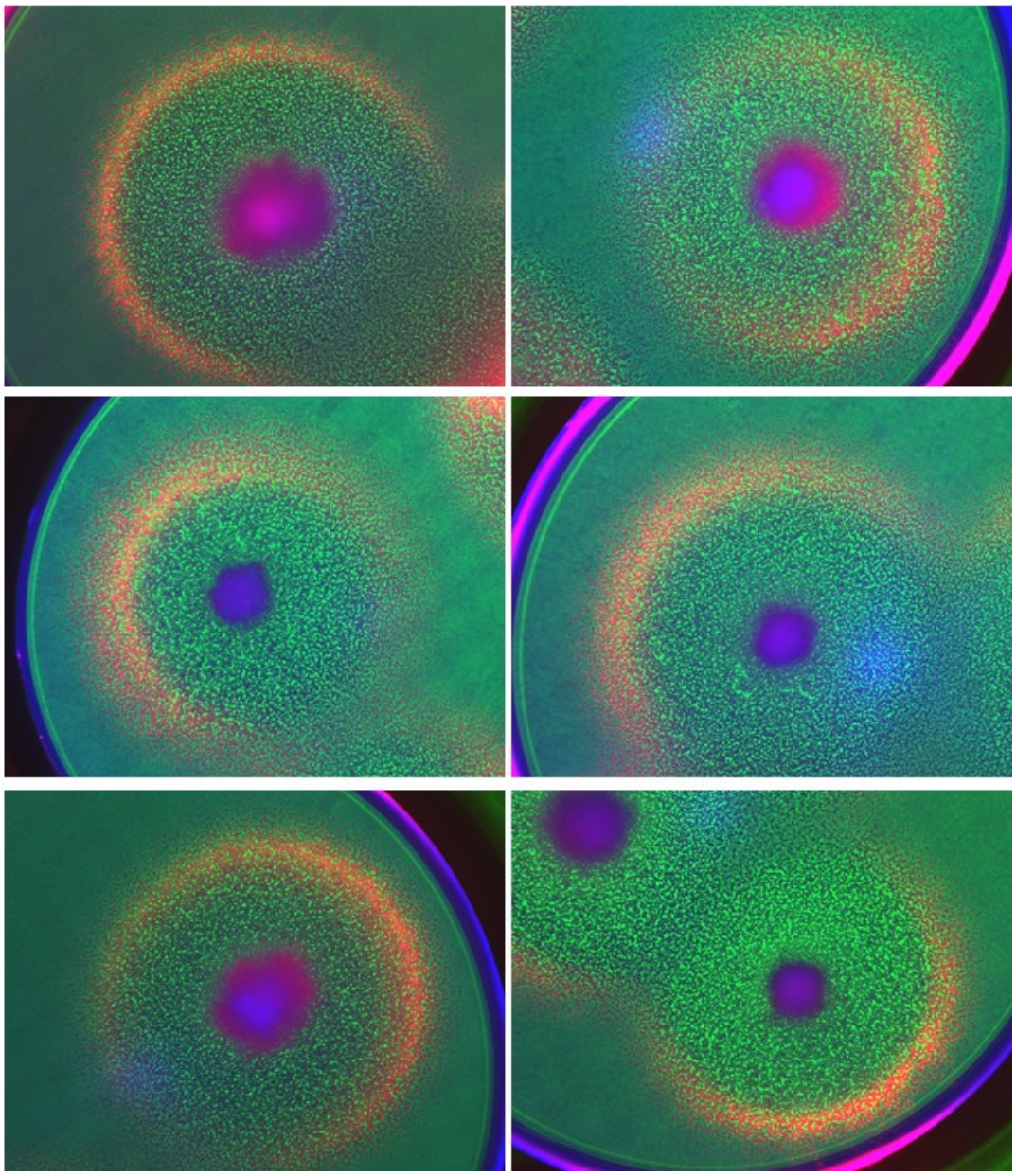

Figure 36: Raw 1.7 mm X 1.4 mm composite images of patterns obtained for the base-case condition described in Figure 35 derived from six different single cell colonies, spanning five independent experiments. The color scheme is as described in Figure 30. Each pattern was imaged after 35-37 hours of incubation.

5. Development of the mechanism and mathematical modeling

To help resolve the fact that pattern formation occurred despite a spatially uniform morphogen distribution, we developed an agent-based model [149, 150] to simulate the circuit-mediated spatiotemporal dynamics. The modeling was done jointly between me and my colleague, Bochong Li. The work described in this chapter has been submitted for publication: Payne S, Li B, Schaeffer D, You L. "Temporal control of self-organized pattern formation without morphogen gradients in engineered bacteria." Manuscript under review in *Molecular Systems Biology*.

5.1 Mechanism Summary

Briefly, we modeled the cells as agents within which production and degradation of T7 RNAP, T7 lysozyme, and AHL take place. AHL degradation also takes place outside of the cell. We assume that cells undergo a random walk on a 1-Dimensional (1D) spatial domain, where their growth and movement is sensitive to a metabolic burden induced by T7 RNAP and T7 lysozyme. Due to very fast diffusion of AHL, we assume that its concentration is uniform across the entire spatial domain. In addition, we also assume that a cell's global gene expression decreases with increasing distance from the microcolony edge via a variant of the Hill function. Through mathematical modeling, we have shown that spatial-dependent global gene expression is essential in generating the patterns we observe. Although many theoretical mechanisms can account for this spatial-dependent global gene expression, contact inhibition [151] and

mechanical stress [152] provide likely explanations. In addition, a possible contributing factor is that a cell's metabolic capacity increases with local nutrient concentration. This hypothesis is consistent with experimental evidence and the literature [153, 154].

Starting from 10 cells per spatial unit Δ, spanning Δ=1-10, our model can reproduce the observed self-organized patterns (Figure 34f, Figure 37a-c, Figure 38) using biologically feasible parameters (see Table 2). In particular, the simulation demonstrates several salient pattern features, including an initial confined T7 RNAP core, a T7 lysozyme ring with robust size over time, and the tight coupling between microcolony expansion and initiation and maintenance of the lysozyme ring (Figure 34f).

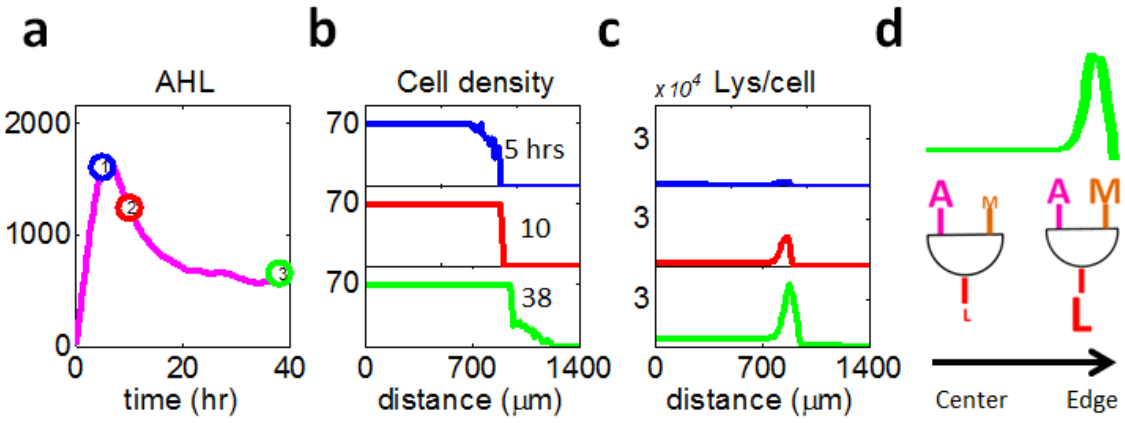

Figure 37: Proposed mechanism for ring formation and maintenance. a) AHL dynamics drive ring formation in the base case simulation. A single AHL temporal pulse gives rise to a single T7 lysozyme ring. Here, the y-axis corresponds to the number of AHL molecules per spatial unit Δ. These dynamics are derived from the same simulation analyzed in Figure 34f with the same base parameter set listed in Table 2. b) Cell density dynamics for the base case simulation. Cell density is plotted as the number of cells per Δ for time points 1-3 of a) (corresponding to 5, 10, and 38 hours) from top to bottom. After AHL exceeds the ring-forming threshold, T7

lysozyme accumulates at the edge of the microcolony (c). Lysozyme induces a metabolic burden on cells at the edge of the microcolony, leading to a stunting of cell growth for several hours (top two panels). Once AHL decreases over time (since T7 lysozyme decreases AHL production), lysozyme's metabolic burden on the cells decreases at the very edge of expansion front, eventually leading to resumed cell growth (bottom panel). c) Lysozyme dynamics for the base case simulation. T7 lysozyme is plotted as the number of T7 lysozyme molecules per cell for time points 1-3 of a) (corresponding to 5, 10, and 38 hours) from top to bottom. As AHL increases over time, T7 lysozyme accumulates at the edge of the spatial domain (top two panels). Eventually, lysozyme level decreases on the very edge of the microcolony (bottom panel), giving rise to microcolony growth resumption (b, bottom panel), while the position of the ring is maintained. d) Lysozyme ring arises due to differential metabolic capacity throughout the microcolony. In the simulations, it is assumed that metabolic capacity (total protein synthesis) increases with decreasing distance from the microcolony edge. Thus, T7 lysozyme production can be viewed as an AND gate, where both high AHL (A) and high metabolic capacity (M) are necessary to trigger lysozyme production. In this manner, at a time when A is uniformly high throughout the entire spatial domain, high A and low M give rise to low lysozyme levels towards the center of the microcolony. However, at the microcolony's edge, high A and high M give rise to high lysozyme levels (green line).

Importantly, the simulation confirms the notion that robust pattern formation does not require an AHL gradient. Instead, it underscores the critical interplay between cell growth and gene expression, which converts temporal information regarding the history of cell growth into spatial patterns (Figure 37 and Figure 38). Initially, AHL concentration is low due to diffusion-mediated dilution spanning the entire spatial domain. Thus, the early circuit dynamics are dominated by T7 RNAP positive-feedback.

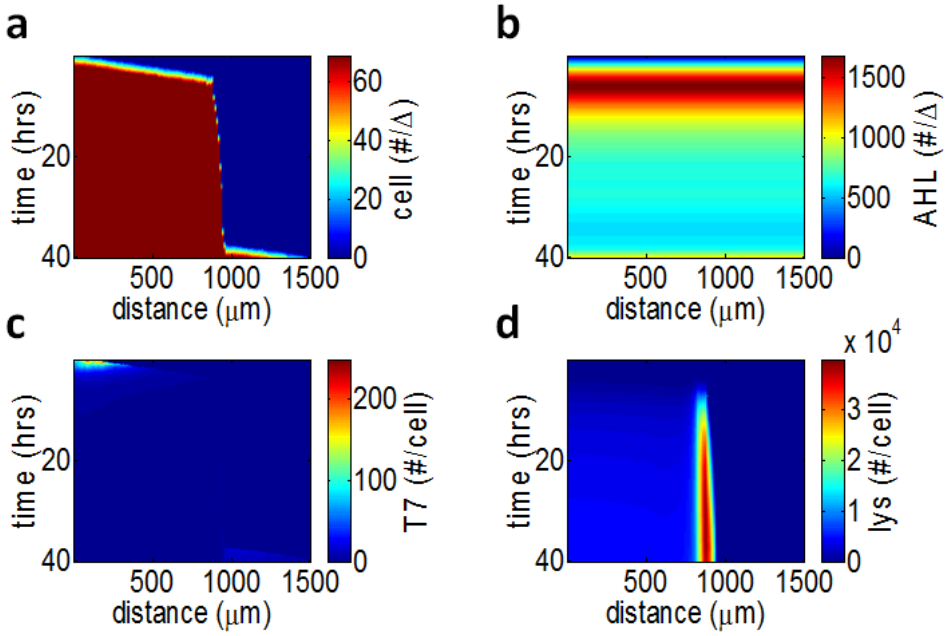

Figure 38: Simulated spatiotemporal dynamics of key species for the base case. a)-d) Heat maps displaying cell density (a), AHL (b), T7 RNAP (c), and T7 lysozyme (d) for varying distance (x-axis) over time (y-axis) for the simulation shown in Figure 37 (the base case). The intensity values for a)-b) represent cell and AHL numbers per spatial grid Δ, respectively, across a 1-dimensional (1D) spatial domain spanning length 300 Δ (3000 μm). The intensity values for c)-d) represent the number of T7 RNAP and T7 lysozyme molecules per cell, respectively, across the 1D spatial domain.

The high T7 RNAP in the microcolony interior eventually gives rise to faster production of AHL, leading to a uniform elevation of AHL concentration throughout the entire spatial domain. Once AHL accumulates to a critical threshold level, it can activate T7 lysozyme production. This activation occurs on the colony edge, where the metabolic capacity of the cell is high, leading to an mCherry ring (Figure 37c-d). Towards the microcolony center, however, low metabolic capacity results in low lysozyme production and mCherry expression. Thus, lysozyme synthesis can be viewed as the

result of an AND logic gate: specifically, synthesis only occurs as the result of both high AHL and high metabolic capacity. This logic gate results in low mCherry in the microcolony interior and high mCherry at the microcolony edge at a uniformly high AHL concentration. These mCherry dynamics are confirmed by confocal imaging (Figure 39), where we observe that the apparent mCherry core from fluorescence microscopy (Figure 34b) indeed is the result of another mCherry ring pattern occurring in the z-direction in the microcolony core. On the x-y plane where subsequent growth outside of the core is observed, a single mCherry ring forms on the microcolony edge as the model predicts. At the ring, expression of lysozyme causes significant growth inhibition and a pause of colony expansion (Figure 34d,f, Figure 37b, Figure 38). Consequently, growth inhibition leads to a reduced dilution rate of lysozyme, reinforcing its accumulation. Thus, the interplay between expression of lysozyme and growth inhibition creates a local positive feedback, which facilitates the maintenance of the ring pattern.

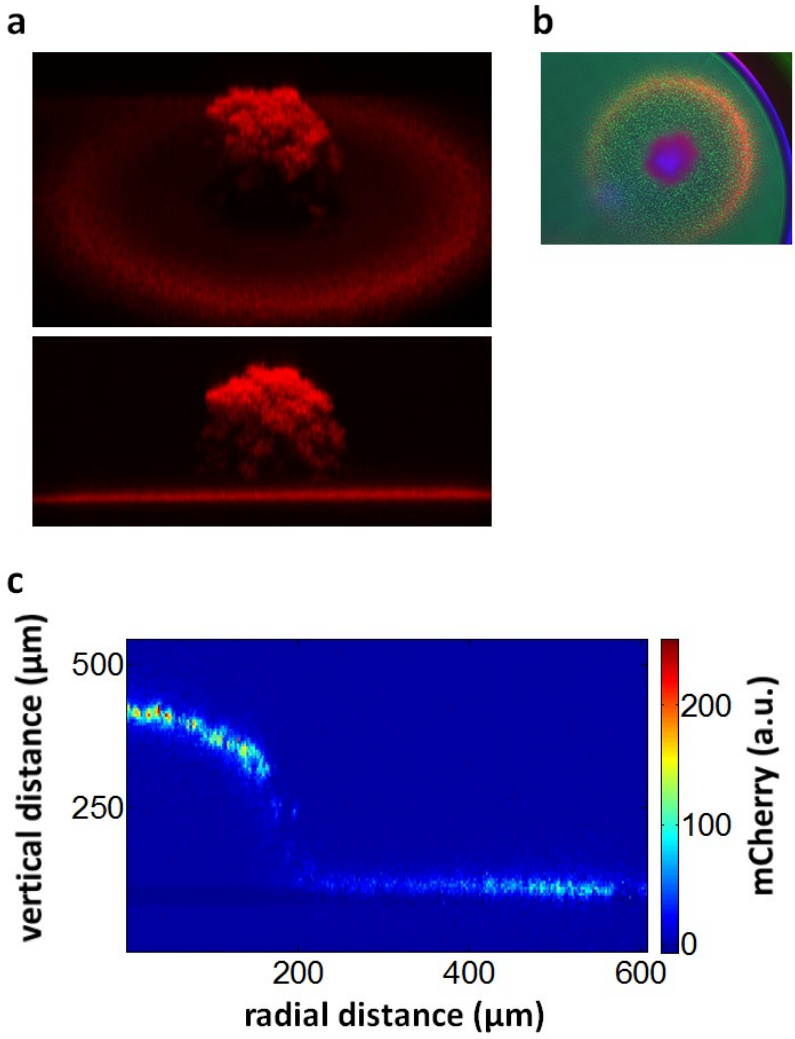

Figure 39: 3-Dimensional (3D) confocal image of a typical base-case mCherry pattern. a) Tilted (top) and side (bottom) views of a 3D reconstruction of the mCherry pattern based on a series of z-slice images 5.21 μm in depth spanning x- and y-dimensions of length 1214 μm taken by a Zeiss LSM 780 upright confocal microscope. The pattern was excited at a 561 nm wavelength, and the emission filter used collected wavelengths between 576 and 696 nm. The pattern was obtained for the base-case condition described in Figure 35. The 3D reconstruction was done using MetaMorph. b) Raw 1.7 mm X 1.4 mm composite fluorescent image of the pattern displayed in a). The color scheme is as described in Figure 30. c) Heat map displaying mCherry intensity in both the vertical (y-axis) and radial (x-axis) directions as derived from the confocal microscope image reconstructed in a). The radial intensity values are the average intensity values across angles spanning 3π/4 to 7π/4. Processing was carried out using a custom MATLAB code.

Over time, AHL concentration gradually decreases due to reduced T7 RNAP strength (Figure 37a). As a result, lysozyme decays on the colony's very edge and thus lysozyme-induced metabolic burden is alleviated, leading to the resumption of cell growth and colony expansion. Now, AHL concentration is too low to trigger expression of mCherry at the colony expansion front. As a result, the ring radius is maintained over time at its initial position in a manner that is decoupled from further colony expansion.

5.2 The mathematical model

We model the experimental pattern formation system with an agent-based-model in one spatial dimension. The main goal of this simplified model is to demonstrate the generic feasibility of pattern formation through a timing mechanism controlled by a uniformly distributed morphogen (i.e., AHL). The model captures the key aspects of the experimental system: interactions between major circuit components, as well as cell proliferation and movement.

In our model, cells are treated as individual agents within which intracellular reactions, namely the production and degradation of T7 RNAP and T7 lysozyme, as well as the production of AHL, take place. Whereas the T7 RNAP and T7 lysozyme proteins are confined to their cell of origin, AHL freely diffuses across the cell membrane, and its degradation occurs both inside and outside the cell. We assume that metabolic activity decreases as the distance between the host cell and the edge of the colony increases [155], and we model this spatial dependence by means of a steep Hill function. More

precisely, only a boundary layer of cells located close to the edge of the colony can efficiently synthesize proteins. T7 RNAP enhances its own production through a positive-feedback loop, and activates the production of AHL. AHL then induces lysozyme expression, which in turn inhibits T7 RNAP production. T7 RNAP and lysozyme are known to bind and form the T-L complex (denoted hereafter as P), and the corresponding reversible first order kinetics takes place on a very fast time scale [137]. Additionally, T-L complex can inhibit T7 and AHL synthesis on the transcriptional level as described in [140]. In summary, the chemical reactions are captured by the following differential equations:

$$T7\ RNAP\ (T): \quad \frac{dT}{dt} = \left(\frac{K_P}{P + K_P}\right)\left(\frac{k_T T}{T + K_T}\right) - d_T T - k_{TL}\mathrm{TL} + d_P \mathrm{P},$$

$$Lysozyme\ (L): \quad \frac{dL}{dt} = \frac{k_L A^m}{A^m + K_A^m} - d_L L - k_{TL}\mathrm{TL} + d_P \mathrm{P},$$

$$T - L\ Complex\ (P): \quad \frac{dP}{dt} = k_{TL}\mathrm{TL} - d_P \mathrm{P},$$

$$AHL\ (A): \quad \frac{dA}{dt} = D_A \Delta \mathrm{A} + \left(\frac{K_P}{P + K_P}\right)\left(\frac{C k_A T}{T + K_T}\right) - d_A A$$

where

$$k_T = \phi(r)k_{T_0},\ k_A = \phi(r)k_{A_0},\ k_L = \phi(r)k_{L_0},$$

$$\phi(r) = \frac{\left(\frac{1}{r}\right)^\gamma}{\left(\frac{1}{r}\right)^\gamma + \left(\frac{1}{K_\phi}\right)^\gamma} + \phi_0,$$

and r is the distance between the cell where the reactions take place and the edge of the "cell colony" (the position of the cell furthest from the left end of the 1D grid). Based on the fast diffusion of AHL, we assume instantaneous diffusion of AHL by setting $D_A = \infty$. Furthermore, the T-L complex is treated as a quasi-stationary field based on its fast reaction dynamics.

The simulation is performed on a 1D grid of length L, with grid elements of length Δ=10 μm. As explained above, the 1D framework is based on the radial symmetry of the experimental system, and the computational domain should be interpreted as a radial section of the expanding colony with the leftmost grid element corresponding to its center. Here, we impose the assumption that all cells within the same grid element have identical intracellular contents (i.e., they harbor identical T and L concentrations). Consequently, the equations for T and L are solved locally in each grid element, provided that at least one cell is present. On the other hand, the equation for A is solved over the entire spatial domain. T and L have units of #/cell. A has units of #/Δ. As an initial condition, one hundred seeding cells are placed uniformly throughout the 10

leftmost grid elements at a concentration of 10 cells per element. Each seeding cell initially contains 100 T7 RNAP molecules and 1 lysozyme molecule.

The simulation of cell dynamics is built upon a previously established framework [149, 150], and is carried out based on a set of rules chosen empirically to capture the proliferation and jump dynamics of the cells. For each time step Δt = 1 min, one of two potential actions can be taken for each grid element that harbors at least one cell: division or movement, chosen randomly with equal probability. If division is the chosen event, a new cell is generated with probability

$$1 - exp\left[-\left(\frac{c}{(\frac{L}{L+K_{Lg}})(\frac{T}{T+K_{Tg}})\theta_g}\right)\right],$$

increasing the cell number from c to c+1 in the respective grid element. Consequently, the intracellular contents summed up over c cells (before division) are distributed equally among (c+1) cells. If movement is the chosen event, one cell inside the grid element moves with probability

$$1 - exp\left[-\left(\frac{C}{(\frac{L^{h_L}}{L^{h_L} + K_{Lm}^{h_L}})(\frac{T^{h_T}}{T^{h_T} + K_{Tm}^{h_T}})\theta_m}\right)\right]$$

into one of the two adjacent grid elements. If both adjacent grid elements have fewer cells than the central element, the moving cell chooses one of the two elements to move

into with equal probability; if only one adjacent element has fewer cells, the moving cell moves into that element; if neither element has fewer cells, no jump takes place. The cells in the leftmost grid element can only jump to the right. As long as a jump occurs, the cell number in the original grid element is reduced by one. Consequently, the total number of each intracellular molecular species summed over the c cells (before movement) in the destination grid element and the moving cell is divided equally among the (c+1) cells (after movement) in the destination grid element; the intracellular contents (T and L per cell) of the remaining (c-1) cells in the original grid element are unchanged. Note that both the division and jump probabilities decrease with increasing intracellular lysozyme and T7 RNAP concentration. θ_m and θ_g are parameters controlling the baseline motility and growth potentials.

5.3 Implications

To constrain our model, we use literature values where available (see references in Table 2), and choose the remaining parameters (within a reasonable range) in such a way that the simulated dynamics capture the salient features of the experimentally observed system. We expect that the critical role played by the uniformly distributed morphogen can be coupled to a wide array of intracellular and intercellular chemical and physical interactions to generate sophisticated yet controllable patterns. The exact pattern may depend on the specifics of the chemical and physical interactions, yet the

controllability of the pattern actuated through the uniformly distributed morphogen is generally applicable and not restricted to our specific circuit.

Table 2: Definition of model parameters and base parameters

Parameter	Description	Basal Value
k_{T0}	Synthesis rate of T7 RNAP	20 #/(cell·min)
K_T	Half-activation threshold of T7 RNAP	10 #/cell [73]
d_T	Decay rate of T7 RNAP	$5*10^{-3}$ /min [73]†
k_{A0}	Synthesis rate of AHL	32 #/(cell·min)
K_A	Half-activation threshold of AHL	20 nM [63]††
d_A	Decay rate of AHL	$5*10^{-3}$ /min [47]
k_{L0}	Synthesis rate of T7 lysozyme	95 #/(cell·min)
K_P	Half-inhibition threshold of T-L complex	50 #/cell
K_{TL}	Dissociation constant for T-L complex	0.02 # [137]
d_L	Decay rate of T7 lysozyme	$2.4*10^{-4}$ /min
D_a	Diffusivity of AHL	$6.7*10^5$ μm ^{2}/min
θ_g	Cell division probability parameter	767
θ_m	Cell movement probability parameter	$2*10^4$
m	Hill coefficient of AHL binding to the *pluxI* promoter	2
K_ϕ	Half-activation distance for synthesis	6.5Δ
ϕ_0	Basal synthesis	0.1
γ	Hill coefficient for distance dependency	5
h_L	Hill coefficient for T7 lysozyme burden	10
h_T	Hill coefficient for T7 RNAP burden	2
K_{Lg}	Half-inhibition level of T7 lysozyme on growth	$5*10^4$
K_{Tg}	Half-inhibition level of T7 RNAP on growth	$1.4*10^4$
K_{Lm}	Half-inhibition level of T7 lysozyme on motility	620

K_{Tm}	Half-inhibition level of T7 RNAP on motility	3

[†]- The value used in this publication was 0.003 1/min. Our value is within 2-fold.

[††]- The value measured in this publication was 10 nM. Our value is within 2-fold.

6. Pattern modulation by tuning external parameters

An open question in developmental biology is the exact mechanism by which pattern sizes are controlled by genetic and environmental factors. In our system, the critical determinant of pattern size is the timing of AHL accumulation, rather than its spatial gradient, which is negligible within the small dimensions of the microcolony. This timing can be modulated by changing the domain size or by simply adding exogenous AHL (Figure 40a). The negative-feedback loop mediated by the inhibition module has the potential to generate one or more AHL pulses. Indeed, the base-case circuit dynamics result in a single pulse of AHL, which triggers ring initiation when the AHL threshold is exceeded. The initial addition of exogenous AHL to the droplet is expected to decrease the time necessary to reach the AHL threshold and thus leads to earlier formation of a smaller ring (Figure 40a). In contrast, an increase in the domain size is expected to prolong the time necessary for AHL to reach the threshold due to greater spatial dilution, leading to later formation of a larger ring (Figure 40a). The work described in this chapter has been submitted for publication: Payne S, Li B, Schaeffer D, You L. "Temporal control of self-organized pattern formation without morphogen gradients in engineered bacteria." Manuscript under review in *Molecular Systems Biology*.

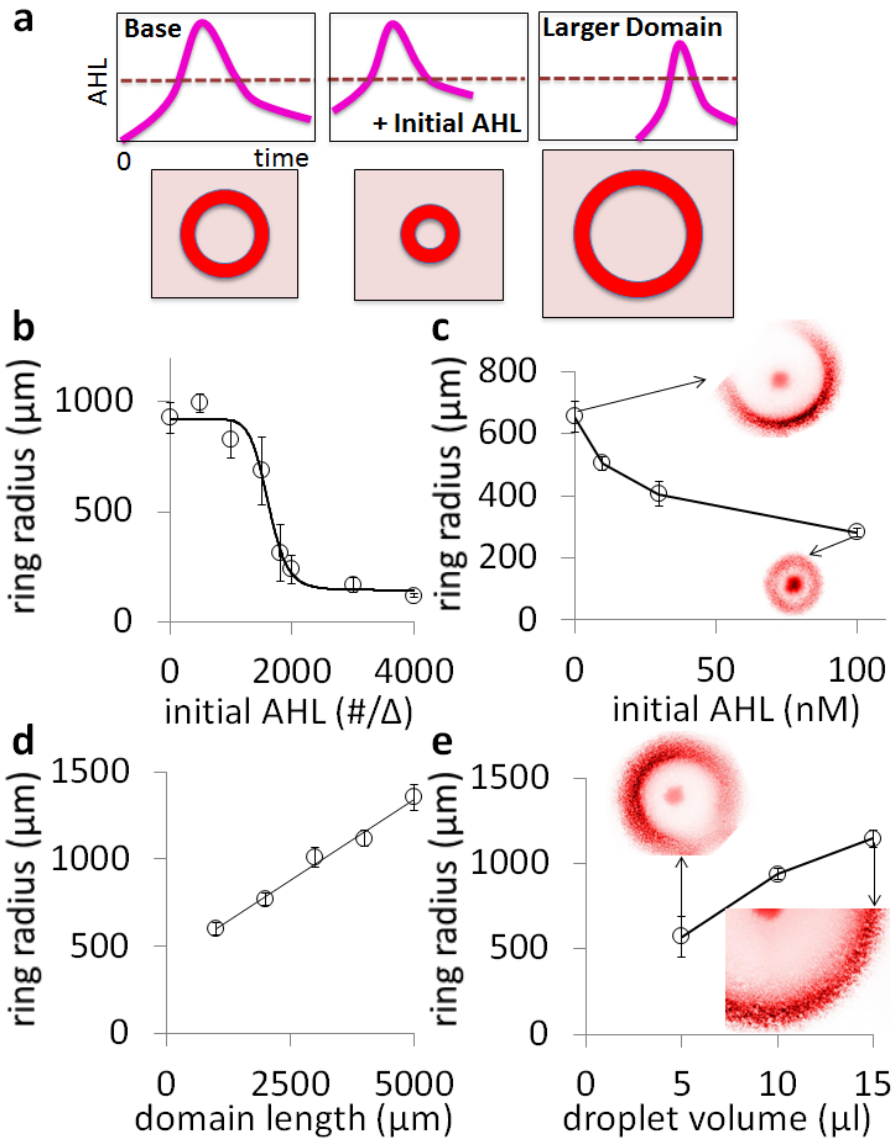

Figure 40: Simulated and measured modulation of pattern formation by environmental factors. a) Modulation of patterns by perturbing AHL temporal dynamics. The base case occurs when a single pulse of AHL exceeds a threshold necessary to trigger ring formation (left, e.g., as in Figure 34 and Figure 37). Adding exogenous AHL allows AHL to exceed the threshold concentration faster, leading to the formation of a smaller ring (center). Increasing the domain size slows down AHL accumulation due to increased spatial dilution, leading to the formation of a larger ring (right). b) Simulated dependence of ring radius on initial, exogenously added AHL concentration. Average mCherry ring radii obtained at 25 hours and 13.3 hours for 1D simulations of microcolonies growing from initial AHL concentrations of 0-

1200 molecules per Δ and 1500-4000 molecules per Δ. For each replicate, the time chosen for data analysis corresponds to the time at which only the first mCherry ring radius has emerged. All of the mCherry ring radii were calculated in the same manner as described in Figure 34. The error bars represent standard error among ten replicates. The black curve indicates a best-fit Hill function calculated using a custom MATLAB code. c) Measured dependence of ring radius on initial, exogenously added AHL concentration. Average mCherry ring radii obtained for microcolonies growing from an initial AHL concentration of 0, 10, 30, and 100 nM AHL, respectively. These values were obtained from replicates at 24-hour time points for 10, 30, and 100 nM AHL and from replicates at 36-hour time points for 0 nM AHL (no mCherry rings emerged for this condition at the 24-hour time point). All of the mCherry ring radii were calculated in the same manner as described in Figure 34. The error bars for 0, 10, 30 and 100 nM AHL represent standard error among 7, 10, 9, and 5 replicates, respectively. Cropped representative mCherry images to scale of microcolonies growing in the absence (top middle panel) or presence (bottom right panel) of an initial AHL concentration of 100 nM at 24-hour and 36-hour time points, respectively, are shown. The color scheme is defined as in Figure 34. d) Simulated dependence of ring radius on the domain size. Average mCherry ring radii obtained at 25 hours for 1D simulations of microcolonies growing in domain lengths spanning 100 to 500 Δ (1000 to 5000 μm). All of the mCherry ring radii were calculated in the same manner as described in Figure 34. The error bars represent standard error among ten replicates. The black curve indicates a best-fit linear function calculated using Microsoft Excel. e) Measured dependence of ring radius on the droplet size. Average mCherry ring radii obtained for microcolonies growing in 5-μl, 10-μl, and 15-μl droplets, respectively. These values were obtained from replicates at 36-hour time points for 5-μl and 10-μl droplets and from replicates at 48-hour time points for 15-μl droplets (only one mCherry ring emerged for this condition at the 36-hour time point). All of the mCherry ring radii were calculated in the same manner as described in Figure 34. The error bars for 5-, 10-, and 15-μl droplets represent standard error among 3, 6, and 6 replicates, respectively. Cropped representative mCherry images of microcolonies to scale growing in 5-μl (top left panel) and 15-μl droplets (bottom right panel) at 36-hour and 48-hour time points, respectively, are shown. The color scheme is defined as in Figure 34.

6.1 Modulation of ring size by initial AHL concentration and domain size perturbations

We carried out further simulations and experiments to test these notions. Indeed, our simulations predict that the ring size decreases with increasing initial AHL concentration (Figure 40b and Figure 41). This prediction was consistent with our experimental observation: the mCherry ring radius decreased from 655 μm to 282 μm as we increased the initial AHL concentration from 0 to 100 nM (Figure 40c). Similarly, our simulations predict that the ring size increases with domain size (Figure 40d, Figure 42, Figure 43). Our experiments confirmed this prediction: mCherry ring radius increased from 572 μm to 1145 μm as we increased the droplet size from 5 μl to 15 μl (Figure 40e).

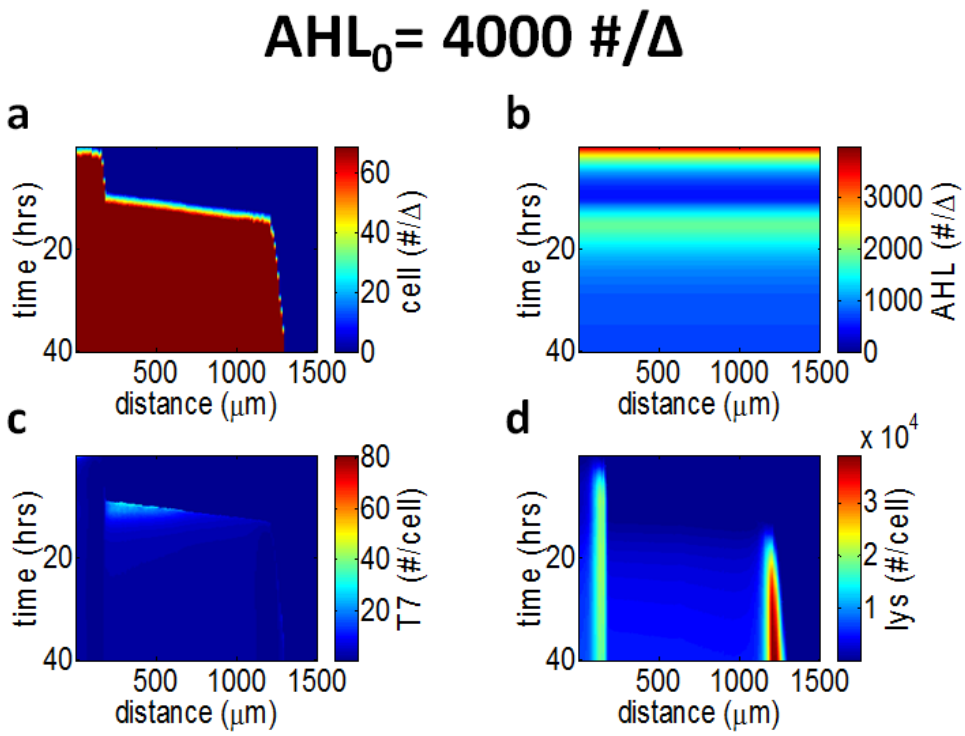

Figure 41: Simulated spatiotemporal dynamics of key species for an initial AHL concentration of 4000 molecules/Δ. a)-d) Heat maps displaying cell density (a), AHL

(b), T7 RNAP (c), and T7 lysozyme (d) for varying distance (x-axis) over time (y-axis) for a typical simulation with an initial AHL concentration of 4000 molecules/Δ. Units are as described in Figure 38, and the simulation took place across a 1-dimensional (1D) spatial domain spanning length 300 Δ (3000 μm).

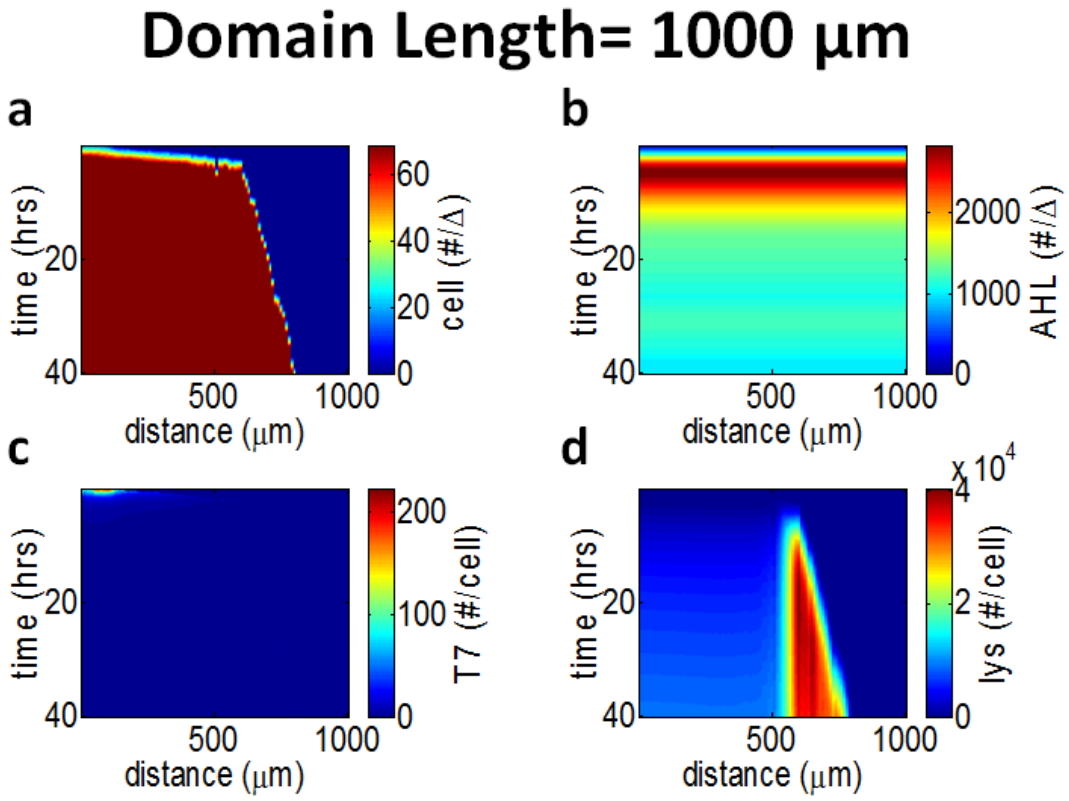

Figure 42: Simulated spatiotemporal dynamics of key species for a domain size of 100 Δ (1000 μm). a)-d) Heat maps displaying cell density (a), AHL (b), T7 RNAP (c), and T7 lysozyme (d) for varying distance (x-axis) over time (y-axis) for a typical simulation with a 1-dimensional (1D) spatial domain spanning length 100 Δ (1000 μm). Units are as described in Figure 38.

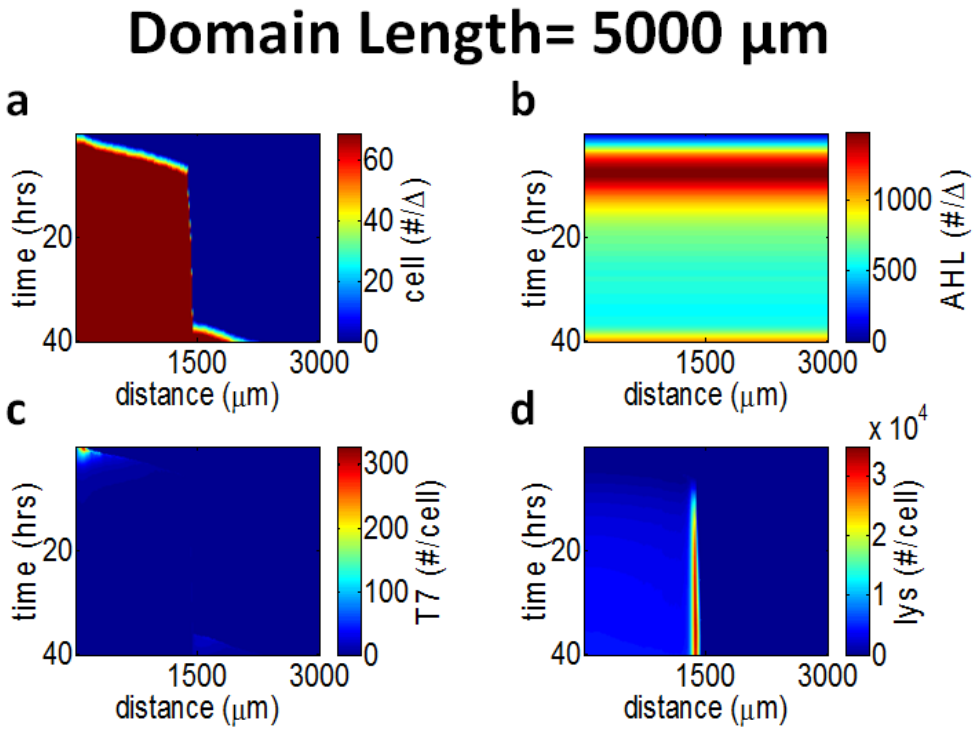

Figure 43: Simulated spatiotemporal dynamics of key species for a domain size of 500 Δ (5000 µm). a)-d) Heat maps displaying cell density (a), AHL (b), T7 RNAP (c), and T7 lysozyme (d) for varying distance (x-axis) over time (y-axis) for a typical simulation with a 1-dimensional (1D) spatial domain spanning length 500 Δ (5000 µm). Units are as described in Figure 38.

6.2 Realization of a double-ring pattern

In addition, our simulations indicate that our system can generate a double-ring pattern when the AHL threshold necessary to initiate ring formation is exceeded twice during two discrete time intervals (Figure 44a-b). Multiple rings were obtained within a reasonable time frame most easily for very high initial AHL concentrations which exceeded the ring-forming threshold from the start of colony formation (Figure 44a-b and Figure 45). Again, this prediction was validated experimentally. A double-ring

pattern was observed after 48 hours of incubation for a single microcolony in a 5-μl droplet when supplied with an initial AHL concentration of 100 nM (Figure 44c-d). Note that in both the simulated and experimental cases for which a double ring occurs, the rings emerge sequentially with one ring first occurring at a smaller radius, followed by a second ring occurring at a larger radius (Figure 44b,d and Figure 45**)**. Here, the first ring corresponds to the initial time interval in which AHL exceeds the ring-forming threshold, and the second ring corresponds to the second time interval in which AHL exceeds the ring-forming threshold (Figure 44a-b and Figure 45).

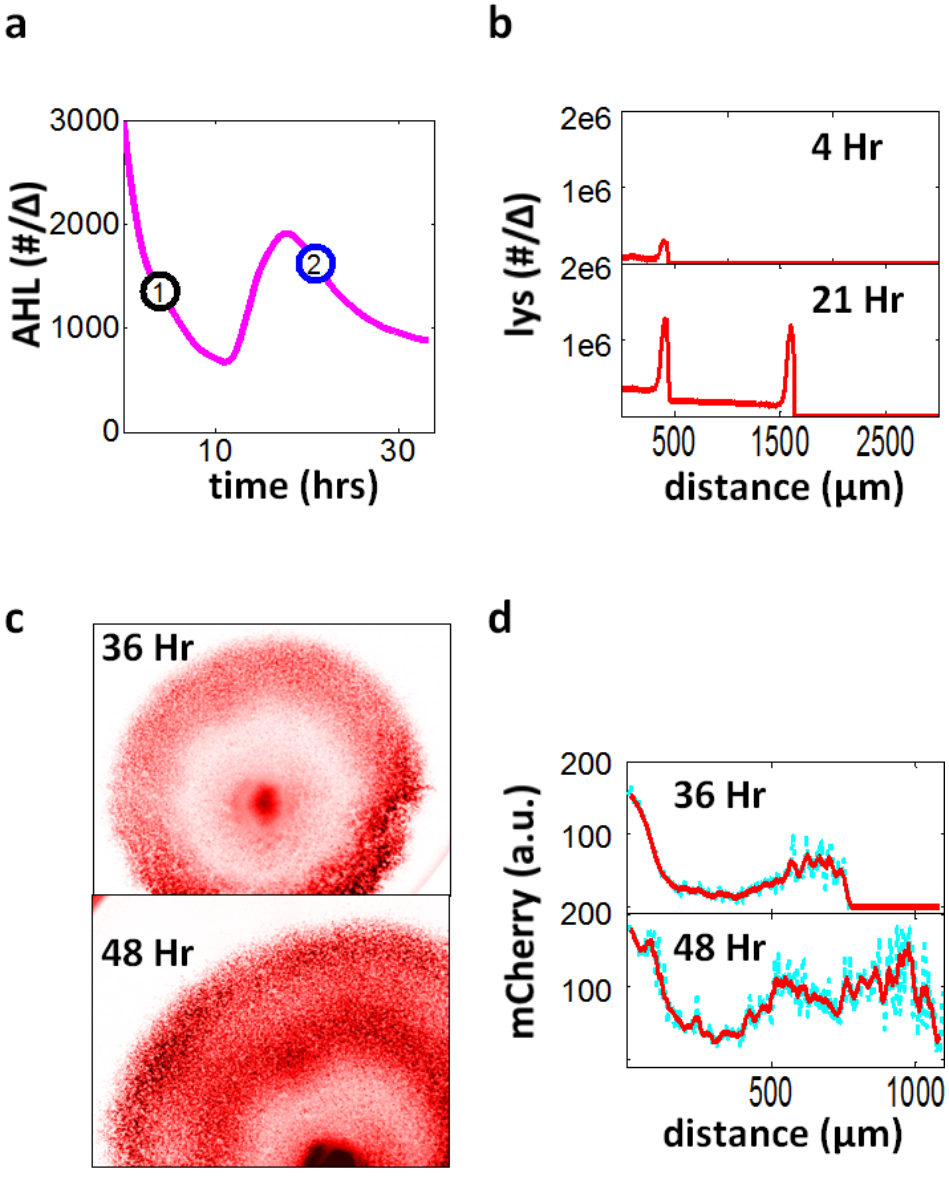

Figure 44: Predicted and measured double-ring formation. a) Simulated AHL dynamics for the double-ring case. AHL in molecules per Δ over time for the double-ring case simulation. Here, the simulation is implemented with the parameters listed in Table 2. The initial AHL concentration in the simulation is 3000 molecules per Δ. AHL crosses the threshold necessary for ring formation at two discrete time periods. b) mCherry intensity (red line) at varying radii for time points 1 and 2 in a). The line plots indicate T7 lysozyme in molecules per Δ for the two time points indicated in a) (4-hour and 21-hour time points, respectively). A single ring forms at ~50 Δ (~500 μm) for the 4-hour time point. This ring is also maintained for the 21-hour time point.

However, after a second instance of crossing the AHL threshold necessary for ring formation, another ring at ~150 Δ (~1500 μm) emerges at the 21-hour time point. c) An experimentally obtained mCherry double-ring pattern. These images were obtained after culturing a single microcolony for 36 (top) and 48 (bottom) hours at an initial AHL concentration of 100 nM. The color scheme is as described in Figure 34. d) mCherry intensity (cyan dots) at varying radii for the images in c). The solid red line is the running average at varying radii. mCherry was calculated as described in Figure 34 across angles spanning 5π/6 to 3π/2 for the 36-hour time point and across angles spanning π to 7π/6 for the 48-hour time point.

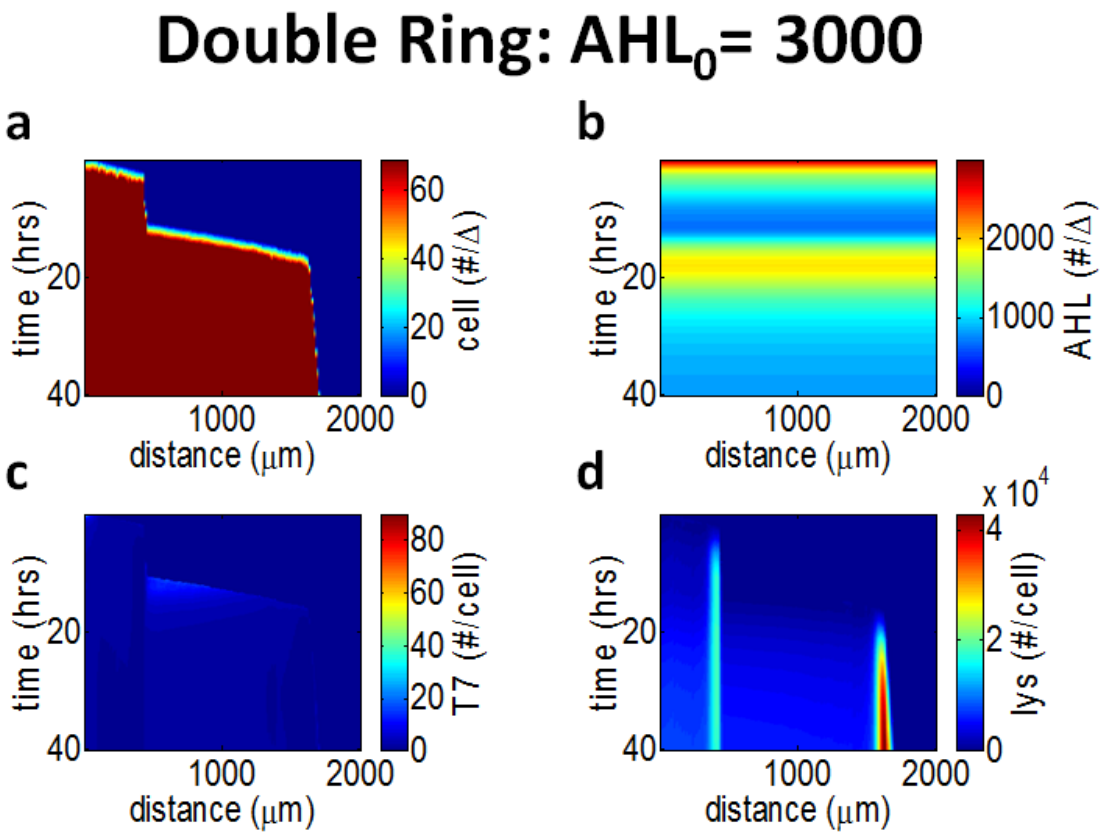

Figure 45: Simulated spatiotemporal dynamics of key species for the double-ring case (an initial AHL concentration of 3000 molecules/Δ). a)-d) Heat maps displaying cell density (a), AHL (b), T7 RNAP (c), and T7 lysozyme (d) for varying distance (x-axis) over time (y-axis) for the simulation showed in Figure 44 with an initial AHL concentration of 3000 molecules/Δ. Units are as described in Figure 38, and the simulation took place across a 1-dimensional (1D) spatial domain spanning length 300 Δ (3000 μm).

6.3 Experimental Setup

For Figure 34, Figure 40c, and Figure 44, overnight LB cultures of our engineered cells supplemented with 75 μg/ml carbenicillin and 50 μg/ml chloramphenicol were prepared and diluted to ~1-4 cells in 5 μl of 0.07% 2xYT (pH=6.5) soft agar. The soft agar was supplemented with the same concentration of antibiotics and 1000 μM IPTG. Eight 5-μl aliquots of the soft agar mix were placed into 8 1-mm deep, 6-mm diameter wells of a CultureWell™ multiwell chambered coverslip (Grace Bio-Labs; Bend, OR, USA; Item #103380), and a glass coverslip was applied to the top (see Figure 31 and Figure 35).

For Figure 40e, the same process was done for 5-μl, 10-μl, and 15-μl soft agar droplets with ~1-4 cells per droplet. However, four aliquots of soft agar mix were placed into 4 1-mm deep, 9-mm diameter wells of a CultureWell™ multiwell chambered coverslip (Grace Bio-Labs; Bend, OR, USA; Item #103340).

6.4 Data Processing

For the experimental data presented in Figure 34, Figure 40, and Figure 44, the RFP imaging was done with the excitation filter was set to 546/12, and the emission filter was set to 605/75. The CFP imaging was done with the excitation filter was set to 436/20, and the emission filter was set to 480/40. The exposure levels were chosen independently for each image to avoid saturation, except in the case of Figure 34, where the exposure settings were kept constant.

An edge detection algorithm was used to segment the core of the microcolony based on the phase image. The center of the microcolony was then calculated as the centroid of the microcolony core. For Figure 34, the intensity values were calculated by averaging across all angles spanning 0 to 2π after subtracting for background. For Figure 40 and Figure 44, the intensity values were then calculated by averaging across all angles of a sector at fixed radii after subtracting for background. mCherry ring radius was defined as the radius corresponding to the maximum running average of mCherry. Sectors were chosen to avoid edges of the droplet and interference from other microcolonies growing in the same well.

For Figure 40e, some microcolonies were so large such that a microcolony core did not appear within the frame of the image. In these cases, another algorithm was used to quantify mCherry ring radius. The algorithm calculated the running average of mCherry across the whole image, excluding edges of the droplet. Then, the maximum running average of mCherry was indexed by location for each horizontal row in the image. A function relating this location to vertical distance was fitted to an equation for a perfect circle. Based on this best-fit function, the mCherry ring radius was extrapolated.

All of these data analyses were conducted using custom code in MATLAB. In addition, single microcolonies per well were excluded from the data analysis process since their dynamics were significantly different in that the mCherry rings emerged later

and were of larger size than other samples under the same condition. Furthermore, microcolonies were initially excluded from being imaged if they rested too close to the edge of the droplet or were too close in proximity to another microcolony. In total, for Figure 40c, seven, ten, nine, and five samples were analyzed for the 0, 10, 30, and 100 nM AHL data points, respectively. For Figure 40e, three, six, and six samples were analyzed for the 5-μl, 10-μl, and 15-μl droplet data points, respectively.

All of the processing of the simulation results was done in the same manner described above for the experimental data. However, all molecule and cell numbers were taken directly from the 1D spatial domain as opposed to being averaged across angles.

7. Significance and Future Directions

As mentioned in Chapter 1, synthetic biological systems can be used for two purposes. First, synthetic biological systems can help us better understand how natural biological systems function. Second, synthetic biological systems can be the basis for various practical applications. Our pattern-forming system also has this dual significance. The system illustrates novel and underappreciated design principles present in natural pattern-forming biological systems, while having the potential for future applications in the generation of patterned biomaterials.

7.1 Significance to natural biological systems

7.1.1 Morphogen as a temporal cue

Our analysis has established a novel mechanism for forming self-organized patterns: Instead of providing a spatial cue, the morphogen serves as a timing cue to initiate pattern formation. Thus, the pattern length scale is decoupled from that of the morphogen. These properties are fundamentally different from recent examples of synthetic pattern-forming circuits [33, 36, 156], where the length scale of the pattern was determined by the length scale of the morphogen gradient. Our mechanism suggests a new way to view the role of morphogens involved in natural pattern-formation processes.

Most past studies have focused on elucidating how morphogen gradients are generated and interpreted to realize precise patterns [157-159]. However, a recent study

suggests that pattern formation in early sea urchin development does not require the participation of a morphogen [160]. In addition, the role of mechanical forces has become increasingly appreciated in diverse pattern-forming biological systems [161-163]. Even when apparent morphogens are identified [121], their specific role in forming the resulting patterns has not been definitively established [159]. Furthermore, a recent study has shown that a flat spatial distribution of the morphogen Bicoid can still give rise to well-defined head gap gene domains in *Drosophila* embryogenesis [164, 165]. Taken together, these studies and our results suggest that the common view of a spatial morphogen gradient being the central driver of pattern formation may be biased and underestimate the contribution of the temporal morphogen dynamics, as well as that of other cellular processes, such as cell growth and movement.

7.1.2 Relevance to the chalone hypothesis

In addition, the role of AHL in our system is analogous to that of secreted negative feedback factors ("chalones") that are involved in tissue development [166]. This concept, proposed 5 decades ago, explains organ size control as the result of slow accumulation of the chalone as cells proliferate. Once an organ reaches its target size, chalones accumulate to high enough concentrations to inhibit further organ growth [167]. While recent studies have identified candidate factors that fulfill the classical definition of the chalone [32, 166, 168], the specifics of how their local activity translates to organ size regulation is an open question [168]. By utilizing a synthetic system in

which a diffusible signal (AHL) activates synthesis of the growth inhibitor (T7 lysozyme), we have eliminated many confounding factors influencing pattern-formation processes in natural systems. This strategy allowed us to observe that one possible method by which chalones regulate pattern size is through sensing the domain size by a fast-diffusing signal (Figure 40d-e). If so, our mechanism can provide an intuitive explanation for scale invariance observed in many developmental processes.

7.2 Significance in biomaterial applications

Presently, synthetic biology is almost exclusively used in an industrial setting to make bulk products. Metabolic pathways are being engineered in organisms to maximize the production of a certain compound. Whether the final product is a fine chemical, a fuel source, or a fragrant molecule, the goal is to maximize output of that final product in bulk culture. However, I believe that as synthetic biology progresses and we are able to engineer gene circuits more rapidly and reliably, the industry will move towards the production of 3-dimensional (3D) products, or materials that are manufactured completely via biosynthetic processes. In fact, Siluria Technologies (San Francisco, CA) is already attempting to use synthetic biological tools to construct unique nano-structures. Specifically, the company is growing metals and metal oxide crystals on biological templates to produce nanowires and other useful biomaterials (Figure 46).

In such applications, our gene circuit can be viewed as the catalyst for a self-organized biological template. With no outside physical manipulation of the system, our

system can generate complex, 3D spatial gene expression patterns. By putting gene(s) capable of the biosynthesis of various useful compounds downstream of the fluorescent proteins in our gene circuit, one can generate complex biomaterials, where the precise position of synthesized compounds is predefined by the 3D spatial gene expression patterns. Since nature has so generously created an almost endless supply of biosynthesis gene pathways, the possibilities for such a design are virtually limitless. A few of these possibilities are in the process of being explored currently.

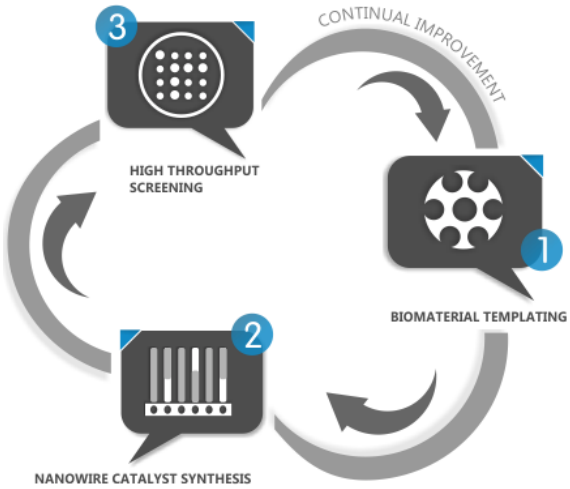

Figure 46: Siluria Technologies' methodology for catalyst development workflow via biological pathways (adapted from http://siluria.com/Technology/Process). 1) Natural growth of biological templates. These templates are utilized as a seed layer for the development of nanowires. 2) After nanowires have been synthesized, the biological template is removed with the addition of excess heat, leaving behind only the desired nanowires. 3) High throughput screening of catalysts is performed. By screening tens of thousands of potential catalysts simultaneously, Siluria Technologies' method is advantageous to traditional approaches used to obtain proper catalysts for nanowires, which can only test one catalyst per reactor in two days.

7.3 Future directions

7.3.1 Inkjet printing

Although this project can potentially be continued in a variety of different directions, we are most excited about the system's potential for the production of future biomaterials (7.2). Before the system can be reliably exploited for these purposes, it is important to have precise control of the initial conditions. Most importantly, we must develop a platform for the precise placement of initial seeding cells. As described in 6.4, throughout my studies, I did not have a platform to achieve this and therefore had to exclude many microcolonies from my analyses which were either too close to the edge of the agar droplet or too close in proximity to other microcolonies to form a fully developed pattern.

However, I, along with my colleague, Will Cao, have been attempting to solve this problem through the use of inkjet printing technology. We have been tuning experimental protocols to achieve robust and reproducible placement of cells on the order of tens of μms. We believe that with further improvements in our methodology, we will be able to integrate this inkjet printing technology with our gene circuit to obtain the formation of the pattern from an initial cell seeded at a precisely defined location in a robust and reproducible manner. Not only will such a platform be beneficial in standardizing the engineering of complex biomaterials but it will also afford us the opportunity to better characterize various pattern properties by reducing variability

from sample to sample and experiment to experiment. Preliminary work on the development of our inkjet printing technology and its integration with our synthetic system is discussed in Appendix A.

7.3.2 Biosynthesis of cadmium sulfide (CdS)

The biosynthesis of cadmium sulfide (CdS) in microbes has been achieved previously by several research groups [169-173]. Interested in the possibility of biologically produced semiconductors, I obtained DH10B pCysDesulf/LacI2/Rock, an *E. coli* strain which had been shown to produce CdS efficiently in a custom liquid medium [170]. After developing a modified experimental protocol and liquid medium recipe (see Appendix B for more details), I was able to demonstrate the formation of a yellow precipitate at the bottom of a culture tube. Such a yellow precipitate is characteristic of the formation of CdS nanoparticles [171]. In conjunction with Kate Marusak and other members of the Zauscher lab, I am currently working on the further characterization of these nanoparticles. As a first step, we hope to produce thin CdS films from a field of these engineered bacteria.

Eventually, we plan to couple CdS biosynthesis with our gene circuit (in conjunction with inkjet printing technology) to give rise to patterned nanostructures (see Appendix B for more details). One can imagine ring, sphere, and other complex 3D structures containing pure, semiconducting nanoparticles in precise locations of high gene expression as determined by the spatial dynamics of our gene circuit. The

possibility of the formation of other precipitates when other precursor metals are placed in the liquid medium with DH10B pCysDesulf/LacI2/Rock is particularly intriguing because it suggests that multiple nanoparticles may be biosynthesized. This possibility of several outputs stemming from high gene expression raises the prospect of the future development of core-shell nanostructures by integrating our gene circuit with various biosynthesis pathways and inputs.

Appendix A: Inkjet printing

A major problem with the experimental setup for the observation of pattern formation was the lack of control over the initial placement of cells. This problem led to the exclusion of patterns formed by microcolonies in close proximity to other microcolonies or the edge of the agar droplets in data analyses (6.4). In addition, from a biomaterials standpoint, this lack of control led to undesired variability in the patterns obtained from droplet to droplet. These issues associated with a lack of control over the initial placement of cells in the agar droplet led us to explore an alternative experimental setup. In this alternative setup, precise placement of cells was accomplished with the aid of inkjet printing technology.

Inkjet printing of constitutively fluorescent cells

Inkjet printing had been used to print chemicals and cells in a variety of biological contexts previously [39, 40, 174-177]. I was seeking a platform that was cheap and relatively easy to set up in our lab. With those requirements in mind, I settled on replicating the platform implemented by Cohen et al. [177]. Briefly, their platform modified an Epson R280 inkjet printer (Nagano, Japan) to print varying concentrations of small molecule inducers on an agar plate containing growing cells. I chose to implement this platform because the printer cost under $300 and only required minimal modifications to be adapted for biological printing. Importantly, the printer had the capability to print on compact discs (CDs), a capability which could be adapted to print

effectively on rigid, agar disks. In our context, we adapted this capability to print on small, square subsections of agar spanning several cm in length. Other than this modification, the only other modifications required were to replace the ink in the inkjet cartridges with grown bacterial cultures. Meanwhile, we did our best to sterilize other components of the printer, including the printer-head, to avoid contamination. Finally, the printer's use of piezoelectric print-heads was critical as the use of thermal jet heads would expose the printed cells to harmfully high temperatures.

The first task that my colleague, Will Cao, and I undertook in testing this new platform was to print constitutively fluorescent cells in a predictable and precise manner. For this task, we chose MC4100 cells containing the ptetmCherry plasmid. These cells were nonmotile to eliminate significant spreading of the microcolonies. Furthermore, ptetmCherry allowed the cells to constitutively express the fluorescent protein mCherry; this allowed us to visualize the cells effectively under the fluorescent microscope.

Our first attempts at achieving predictable and precise microcolony placement had marginal success (Figure 47). However, after tuning the dilution rate of the overnight bacterial culture and experimenting with various software drawing applications, we arrived at a condition which gave rise to regular, predictable, and precise microcolony placement and growth (Figure 48). The protocol for obtaining this so-called base condition consisted of the following: First, cells were grown from a single

colony in LB medium supplemented with 50 μg/ml chloramphenicol for 16 hours at 37 °C. Those cells were diluted to ~.2 Absorbance as measured using the Victor3 multi-well fluorimeter (see Figure 35 legend). The diluted culture was placed in the inkjet cartridges for subsequent printing. Meanwhile, LB medium was supplemented with 0.3% w/v agar and 50 μg/ml chloramphenicol. One-pixel diameter spots were drawn in the GNU Image Manipulation Program (GIMP) and exported to the Epson Print CD program, which was included with the purchase of the printer. After printing cells using this template on a slab of 0.3% agar 1-mm thick, the cells were allowed to grow for 24 hours at 37 °C. The resulting patterns were imaged using a Leica DM16000B fluorescence microscope with a mercury excitation lamp at 5X objective in both the phase and RFP channels as described in 6.4.

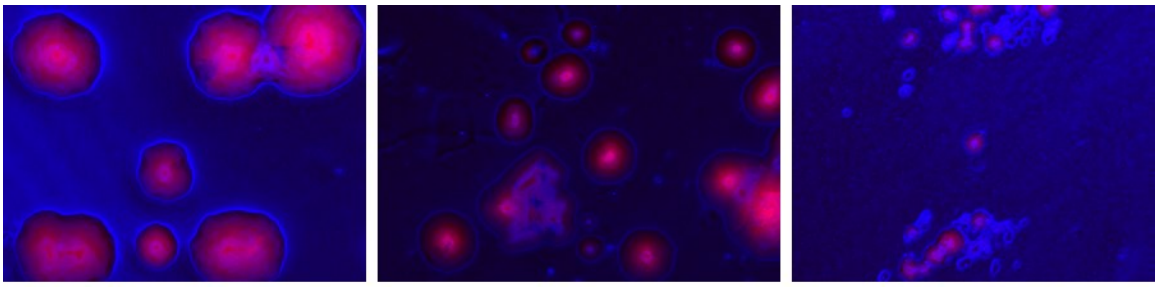

Figure 47: Early attempts at achieving regular microcolony growth at precise, predefined locations. The raw images show cells printed using various protocols after 24 hours of growth on a 1.7 mm X 1.4 mm field. The color scheme is defined as blue representing the phase channel and red representing the RFP channel. The template used here was a grid pattern consisting of 1-mm initial spacing between cells.

With this protocol, we were able to prove that we were able to achieve robust, regular, and reproducible microcolony growth at precisely predefined locations within

~10s of μm resolution using inkjet printing. The next step was to successfully integrate this technology with the pattern-forming capability of our circuit to achieve more precise and reproducible patterns from a growing microcolony of cells containing our gene circuit.

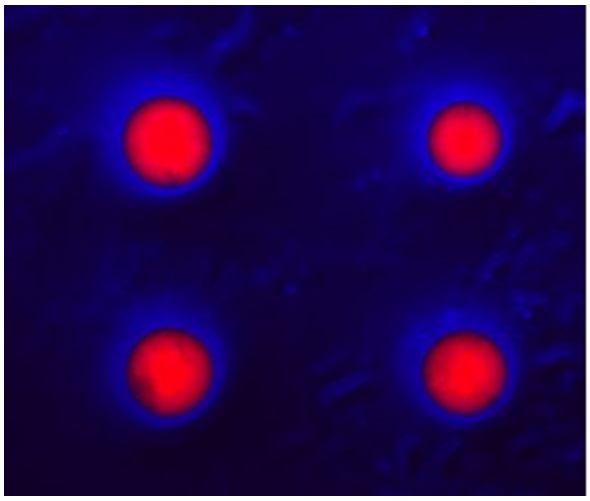

Figure 48: Image of regular, inkjet-printed microcolonies after 24 hours of growth. The protocol and template used is described in the Text. The color scheme is as described in Figure 47. The field spans 1.7 mm X 1.4 mm.

Inkjet printing of pattern-forming cells

Many challenges were encountered when trying to integrate the inkjet printing technology with the pattern-forming gene circuit. The primary challenge involved the fact that inkjet printing had to be done on a rigid agar surface. Preliminary experiments indicated that the lowest agar density required for sufficient printing was 0.3%. However, the pattern-forming cell strain MC4100Z1 pET15bLCFPT7 pTuLys2CMR2 was a nonmotile strain with limited room for colony expansion at 0.3% agar density. For this reason, the two plasmids were transformed into a new, motile strain, MG1655, which

could give rise to substantial colony expansion on the surface of a fluid containing 0.3% agar.

Even though the gene circuit remained unchanged in this new strain, many uncertainties remained. For example, the transcription and translation rates, as well as cell metabolism would be different in the new host. In addition, cell growth and motility were obviously different from the base condition described in Chapter 4. Finally, the circuit's behavior could certainly be different in cells growing on a rigid surface than in cells embedded in the agar. For all of these reasons, validation of the gene circuit's pattern-forming capability needed to be experimentally verified for this new condition.

Upon several rounds of tuning the experimental condition, we finally arrived at a protocol where we again observed mCherry ring formation on the edge of a given microcolony. Briefly, cells were grown from a single colony in LB medium containing 50 μg/ml chloramphenicol and 75 μg/ml carbenicillin for 16 hours at 37 °C. Cells were then diluted to ~.2 Absorbance as described in *Inkjet printing of constitutively fluorescing cells*. These cells were then placed in the inkjet cartridge. Meanwhile, 0.3% agar was prepared in 2xYT medium (buffered at pH=6.5) and supplemented with 50 μg/ml chloramphenicol and 75 μg/ml carbenicillin and 1000 μM IPTG. Then, a template constructed in GIMP containing 5-mm spacing between 1-pixel diameter spots was exported to the Epson CD Printer Program, and cells were printed accordingly. This protocol gave rise to an mCherry ring pattern after 16 hours of cell growth at 30 °C for

several microcolonies (a sample of this pattern is displayed in Figure 49). An interesting feature of such a pattern is that the complex 3D geometry of the core is no longer present for this new condition. In addition, the goal of precise placement of the microcolony has been achieved. Further pattern characterization and tuning of the experimental protocol is being done presently.

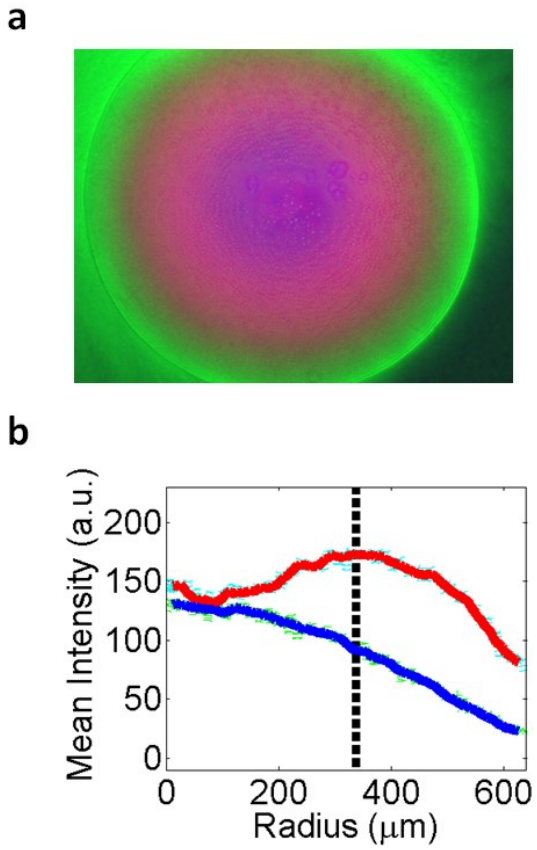

Figure 49: Validation of the pattern-forming capability of cells initially precisely placed using inkjet printing technology. a) Raw fluorescent image of a typical inkjet-printed microcolony of MG1655 cells containing the gene circuit after 16 hours of growth. The color scheme is as described in Figure 30. The protocol and template used is described in the Text. The field spans 1.7 mm X 1.4 mm. b) Quantitative analysis of the mCherry and CFP patterns in the microcolony. Data analysis was completed as described in Figure 34c.

Appendix B: Cadmium sulfide (CdS) production

As discussed in Chapter 7, a goal of synthetic biological pattern formation could be to use it as a template in the fabrication of patterned biomaterials. Although many types of biomaterials could be envisaged, the biomaterial we have focused on fabricating is cadmium sulfide (CdS). The bacterial production of CdS has been verified by many groups [169-173] previously. However, I requested Jay Keasling group's strain, DH10B pCysDesulf/LacI2/Rock, an *E. coli* strain which produced CdS in custom liquid medium [171]. This strain could produce CdS because the plasmid pCysDesulf/LacI2/Rock contains a cysteine desulfhydrase gene, which was involved in the following metabolic pathway:

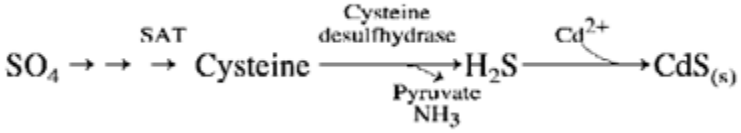

This cysteine desulfhydrase gene is under control of the *plac* promoter, which is inhibited by constitutively expressed LacI. Thus, cysteine desulfhydrase expression is activated by LacI's small molecule inhibitor, IPTG.

The liquid medium in their protocol was quite complex. As such, I created a custom, simpler recipe for optimal CdS production with this strain, which involved several modifications to the M9 recipe listed in 2.2.1.1. First, 75.5492 g of glycerol phosphate disodium salt hydrate (Sigma-Aldrich; St. Louis, MO) was added in place of

64 g of $Na_2HPO_4 \cdot 7H_2O$ and 15 g of KH_2PO_4. Such a replacement provided cells with equimolar concentrations of phosphates, while ridding the culture of inorganic phosphates, which could give rise to cadmium phosphate side products. Second, the medium included 1 mM cysteine. This amino acid is the reactant that cysteine desulfhydrase uses to mediate the production of hydgrogen sulfide, which reacts with cadmium to give rise to CdS. Third, 0.2 mM K_2SO_4 was added. This chemical was added because sulfates are critical in the biological synthesis of excess cysteine. Finally, $CdCl_2$ was added at varying concentrations. Once cysteine is converted into hydrogen sulfide by cysteine desulfyhdrase, the cadmium ions can react to give rise to CdS. Finally, the specific pH was buffered to 7.3, the pH called for in the Keasling group's original paper [171].

Growth Experiments

My colleague from the Zauscher lab, Kate Marusak, and I assessed cell growth by determining cell density in culture tubes through optical density measurements at 600 nm (OD600) using the Victor3 multi-well fluorimeter under aerobic conditions. Initial liquid cultures of the cells were prepared in LB medium supplemented with 75 μg/ml carbenicillin and grown at 37 °C for 16 hours. Then, the cultures were diluted 100-fold in modified M9 medium supplemented with 75 μg/ml carbenicillin and 100 μM IPTG and grown at 37 °C. Measurements were made at seven different $CdCl_2$ concentrations (0 (negative control), 0.01, 0.04, 0.1, 0.2, 0.3, and 0.4 mM) after 21 hours of

growth. As expected, the control culture with no added cadmium showed overall most vigorous growth but did not precipitate CdS. Cell growth was severely stunted at the highest $CdCl_2$ concentration (0.4 mM). A $CdCl_2$ concentration of 0.1 mM caused some growth retardation, but cells grew sufficiently well to generate apparent CdS particles.

Precipitation of CdS

In preliminary experiments, we explored bacterial CdS precipitation as a function of supplemental cysteine, potassium sulfate, and cadmium chloride concentrations, and IPTG addition (Table 3). To this end, we prepared seventeen cultures in modified M9 medium supplemented with carbenicillin and various other components as described in the previous section. The cells did not grow up in the 0.4 mM $CdCl_2$ due to cadmium toxicity. At 0.1 mM $CdCl_2$, yellow precipitates (indicative of CdS precipitates) were seen in Samples 15 and 17. These results led us to conclude that IPTG and supplemental cysteine were necessary for CdS precipitation (Table 3, Figure 50).

Table 3: Matrix of experimental parameters (Cysteine, K_2SO_4, $CdCl_2$, and IPTG addition) and corresponding OD600 mesurements and visual verification of precipitate formation. An X indicates that the reagent was added to the culture medium. For each sample, the overnight culture was diluted 100-fold into fresh medium.

Sample	Cysteine	K_2SO_4	$CdCl_2$ (0.4 mM)	IPTG	Average OD600	Yellow Precipitate?
1					3.2	No
2			X		0.0	No
3	X		X		1.9	No
4		X	X		0.0	No

5			X	X	0.0	No
6		X	X	X	0.0	No
7	X		X	X	0.0	No
8	X	X	X		1.4	No
9	X	X	X	X	0.0	No

Sample	Cysteine	K_2SO_4	$CdCl_2$ (0.1 mM)	IPTG	Average OD600	Yellow Precipitate?
10			X		2.9	No
11	X		X		2.2	No
12		X	X		2.7	No
13			X	X	1.1	No
14		X	X	X	0.7	No
15	X		X	X	2.4	Yes
16	X	X	X		2.7	No
17	X	X	X	X	2.4	Yes

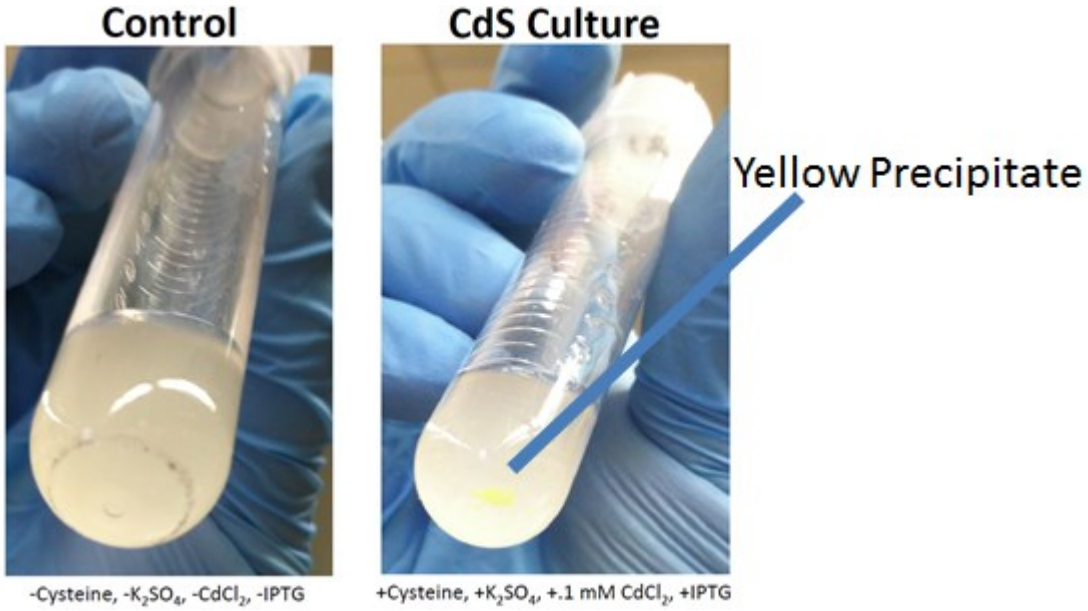

Figure 50: Preliminary demonstration of CdS precipitation. Left image shows Sample 1 (control), and the right image shows Sample 17 with yellow precipitate at the bottom of the test tube.

Transmission Electron Microscopy (TEM)

In addition to visual verification of a yellow precipitate indicative of CdS formation, we also took transmission electron microscope (TEM) images of cell lysates from a culture with the yellow precipitate. The images reveal dark objects varying in size from 10s of nm to 100s of nm (a sample of which is shown in Figure 51). These dark objects represent areas of high electron densities, indicative of heavy nanoparticles. Based on these images, we hypothesize that we have obtained CdS nanoparticles spanning in size from 10s of nm to 100s of nm. Further verification via elemental analysis is necessary to confirm our hypothesis.

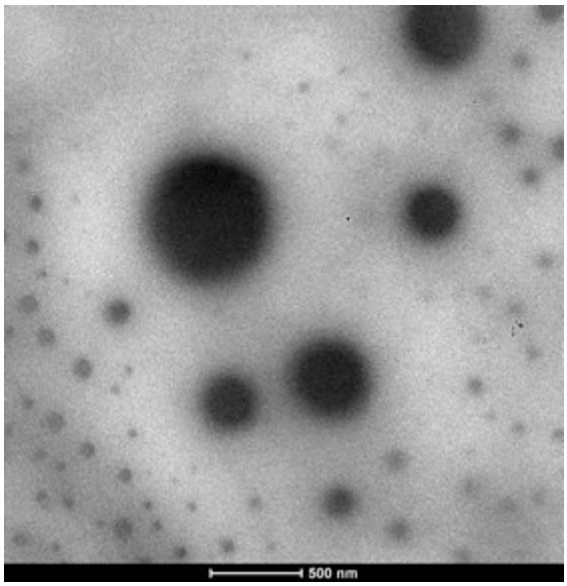

Figure 51: TEM image obtained from lysed cells of a culture with the yellow precipitate.

Future work

Future work will be done to better characterize the properties of these nanoparticles. Most importantly, elemental analysis using an energy-dispersive detector (EDS) is necessary to confirm that the nanoparticles are indeed CdS. In addition, nanoparticle size distribution will be determined by small angle X-ray scattering (SAXS). We will also measure the ratio of cadmium content to sulfur within the particle and use electron diffraction to determine the crystal structure of the particles from bacterially synthesized and chemically synthesized nanoparticles. From these analyses we would like to determine if particle quality is being compromised for the efficiency of bacterial synthesis or if this method could be a similar substitute for chemical synthesis.

Once we have developed an exhaustive method for characterizing the quality and quantity of biologically synthesized nanoparticles, we will identify a base condition for the ideal synthesis of these nanoparticles. This condition will be done in the solid phase such that the resulting nanoparticles can be functionally attached to a substrate. The first step will then be to generate thin films of these nanoparticles after burning off the biological material associated with nanoparticle synthesis. After thin films are developed, inkjet printing technology and our pattern-forming gene circuit will be integrated with bacterial CdS synthesis to make patterned CdS materials.

References

1. Rokas, A., *The origins of multicellularity and the early history of the genetic toolkit for animal development.* Annu Rev Genet, 2008. **42**: p. 235-51.

2. Ispolatov, I., M. Ackermann, and M. Doebeli, *Division of labour and the evolution of multicellularity.* Proc Biol Sci, 2012. **279**(1734): p. 1768-76.

3. LeRoith, D., J. Shemer, and C.T. Roberts, Jr., *Evolutionary origins of intercellular communication systems: implications for mammalian biology.* Horm Res, 1992. **38 Suppl 2**: p. 1-6.

4. Choudhary, S. and C. Schmidt-Dannert, *Applications of quorum sensing in biotechnology.* Appl Microbiol Biotechnol, 2010. **86**(5): p. 1267-79.

5. Elowitz, M.B. and S. Leibler, *A synthetic oscillatory network of transcriptional regulators.* Nature, 2000. **403**(6767): p. 335-8.

6. Gardner, T.S., C.R. Cantor, and J.J. Collins, *Construction of a genetic toggle switch in Escherichia coli.* Nature, 2000. **403**(6767): p. 339-42.

7. Yokobayashi, Y., R. Weiss, and F.H. Arnold, *Directed evolution of a genetic circuit.* Proc Natl Acad Sci U S A, 2002. **99**(26): p. 16587-91.

8. Guet, C.C., et al., *Combinatorial synthesis of genetic networks.* Science, 2002. **296**(5572): p. 1466-70.

9. Chuang, J.S., *Engineering multicellular traits in synthetic microbial populations.* Curr Opin Chem Biol, 2012.

10. Pai, A., et al., *Engineering multicellular systems by cell-cell communication.* Curr Opin Biotechnol, 2009. **20**(4): p. 461-70.

11. Xavier, J.B., *Social interaction in synthetic and natural microbial communities.* Mol Syst Biol, 2011. **7**: p. 483.

12. Tsao, C.-Y., D.N. Quan, and W.E. Bentley, *Development of the quorum sensing biotechnological toolbox.* Current Opinion in Chemical Engineering, 2012. **1**(4): p. 396-402.

13. Shong, J., M.R. Jimenez Diaz, and C.H. Collins, *Towards synthetic microbial consortia for bioprocessing.* Curr Opin Biotechnol, 2012.

14. Waters, C.M. and B.L. Bassler, *Quorum sensing: cell-to-cell communication in bacteria.* Annu Rev Cell Dev Biol, 2005. **21**: p. 319-46.

15. Parsek, M.R. and E.P. Greenberg, *Acyl-homoserine lactone quorum sensing in gram-negative bacteria: a signaling mechanism involved in associations with higher organisms.* Proc Natl Acad Sci U S A, 2000. **97**(16): p. 8789-93.

16. Schaefer, A.L., et al., *A new class of homoserine lactone quorum-sensing signals.* Nature, 2008. **454**(7204): p. 595-9.

17. Hooshangi, S. and W.E. Bentley, *From unicellular properties to multicellular behavior: bacteria quorum sensing circuitry and applications.* Curr Opin Biotechnol, 2008. **19**(6): p. 550-5.

18. Balagadde, F.K., et al., *A synthetic Escherichia coli predator-prey ecosystem.* Mol Syst Biol, 2008. **4**: p. 187.

19. Song, H., et al., *Spatiotemporal modulation of biodiversity in a synthetic chemical-mediated ecosystem.* Nat Chem Biol, 2009. **5**(12): p. 929-35.

20. Shou, W., S. Ram, and J.M. Vilar, *Synthetic cooperation in engineered yeast populations.* Proc Natl Acad Sci U S A, 2007. **104**(6): p. 1877-82.

21. Hu, B., et al., *An environment-sensitive synthetic microbial ecosystem.* PLoS One, 2010. **5**(5): p. e10619.

22. Kim, H.J., et al., *Defined spatial structure stabilizes a synthetic multispecies bacterial community.* Proc Natl Acad Sci U S A, 2008. **105**(47): p. 18188-93.

23. Brenner, K. and F.H. Arnold, *Self-organization, layered structure, and aggregation enhance persistence of a synthetic biofilm consortium.* PLoS One, 2011. **6**(2): p. e16791.

24. Chuang, J.S., O. Rivoire, and S. Leibler, *Simpson's paradox in a synthetic microbial system.* Science, 2009. **323**(5911): p. 272-5.

25. Pai, A., Y. Tanouchi, and L. You, *Optimality and robustness in quorum sensing (QS)-mediated regulation of a costly public good enzyme.* Proc Natl Acad Sci U S A, 2012. **109**(48): p. 19810-5.

26. Pai, A. and L. You, *Optimal tuning of bacterial sensing potential.* Mol Syst Biol, 2009. **5**: p. 286.

27. Sekine, R., et al., *Tunable synthetic phenotypic diversification on Waddington's landscape through autonomous signaling.* Proc Natl Acad Sci U S A, 2011. **108**(44): p. 17969-73.

28. Keller, E.F. and L.A. Segel, *Initiation of slime mold aggregation viewed as an instability.* J Theor Biol, 1970. **26**(3): p. 399-415.

29. Goldbeter, A., *Oscillations and waves of cyclic AMP in Dictyostelium: a prototype for spatio-temporal organization and pulsatile intercellular communication.* Bull Math Biol, 2006. **68**(5): p. 1095-109.

30. Harris, M.P., et al., *Molecular evidence for an activator-inhibitor mechanism in development of embryonic feather branching.* Proc Natl Acad Sci U S A, 2005. **102**(33): p. 11734-9.

31. Chou, C.S., et al., *Spatial dynamics of multistage cell lineages in tissue stratification.* Biophys J, 2010. **99**(10): p. 3145-54.

32. Greco, V., et al., *A two-step mechanism for stem cell activation during hair regeneration.* Cell Stem Cell, 2009. **4**(2): p. 155-69.

33. Basu, S., et al., *A synthetic multicellular system for programmed pattern formation.* Nature, 2005. **434**(7037): p. 1130-4.

34. Matsuda, M., et al., *Synthetic signal propagation through direct cell-cell interaction.* Sci Signal, 2012. **5**(220): p. ra31.

35. Turing, A.M., *The chemical basis of morphogenesis. 1953.* Bull Math Biol, 1990. **52**(1-2): p. 153-97; discussion 119-52.

36. Liu, C., et al., *Sequential establishment of stripe patterns in an expanding cell population.* Science, 2011. **334**(6053): p. 238-41.

37. Saunders, R.E., J.E. Gough, and B. Derby, *Delivery of human fibroblast cells by piezoelectric drop-on-demand inkjet printing.* Biomaterials, 2008. **29**(2): p. 193-203.

38. Xu, T., et al., *Inkjet printing of viable mammalian cells.* Biomaterials, 2005. **26**(1): p. 93-9.

39. Roth, E.A., et al., *Inkjet printing for high-throughput cell patterning.* Biomaterials, 2004. **25**(17): p. 3707-15.

40. Choi, W.S., et al., *Synthetic multicellular cell-to-cell communication in inkjet printed bacterial cell systems.* Biomaterials, 2011. **32**(10): p. 2500-7.

41. Tabor, J.J., et al., *A synthetic genetic edge detection program.* Cell, 2009. **137**(7): p. 1272-81.

42. Tamsir, A., J.J. Tabor, and C.A. Voigt, *Robust multicellular computing using genetically encoded NOR gates and chemical 'wires'.* Nature, 2011. **469**(7329): p. 212-5.

43. Regot, S., et al., *Distributed biological computation with multicellular engineered networks.* Nature, 2011. **469**(7329): p. 207-11.

44. Moon, T.S., et al., *Genetic programs constructed from layered logic gates in single cells.* Nature, 2012. **491**(7423): p. 249-53.

45. Brenner, K., et al., *Engineered bidirectional communication mediates a consensus in a microbial biofilm consortium.* Proc Natl Acad Sci U S A, 2007. **104**(44): p. 17300-4.

46. Levskaya, A., et al., *Synthetic biology: engineering Escherichia coli to see light.* Nature, 2005. **438**(7067): p. 441-2.

47. You, L., et al., *Programmed population control by cell-cell communication and regulated killing.* Nature, 2004. **428**(6985): p. 868-71.

48. Balagadde, F.K., et al., *Long-term monitoring of bacteria undergoing programmed population control in a microchemostat.* Science, 2005. **309**(5731): p. 137-40.

49. Anderson, J.C., et al., *Environmentally controlled invasion of cancer cells by engineered bacteria.* J Mol Biol, 2006. **355**(4): p. 619-27.

50. Xie, Z., et al., *Multi-input RNAi-based logic circuit for identification of specific cancer cells.* Science, 2011. **333**(6047): p. 1307-11.

51. Danino, T., et al., *A synchronized quorum of genetic clocks.* Nature, 2010. **463**(7279): p. 326-30.

52. Prindle, A., et al., *A sensing array of radically coupled genetic 'biopixels'.* Nature, 2012. **481**(7379): p. 39-44.

53. Smyth, A.R., et al., *Garlic as an inhibitor of Pseudomonas aeruginosa quorum sensing in cystic fibrosis--a pilot randomized controlled trial.* Pediatr Pulmonol, 2010. **45**(4): p. 356-62.

54. Kohler, T., et al., *Quorum sensing inhibition selects for virulence and cooperation in Pseudomonas aeruginosa.* PLoS Pathog, 2010. **6**(5): p. e1000883.

55. Roy, V., B.L. Adams, and W.E. Bentley, *Developing next generation antimicrobials by intercepting AI-2 mediated quorum sensing.* Enzyme Microb Technol, 2011. **49**(2): p. 113-23.

56. Gamby, S., et al., *Altering the Communication Networks of Multispecies Microbial Systems Using a Diverse Toolbox of AI-2 Analogues.* ACS Chem Biol, 2012.

57. Chen, G., et al., *A strategy for antagonizing quorum sensing.* Mol Cell, 2011. **42**(2): p. 199-209.

58. Roy, V., et al., *Cross species quorum quenching using a native AI-2 processing enzyme.* ACS Chem Biol, 2010. **5**(2): p. 223-32.

59. Saeidi, N., et al., *Engineering microbes to sense and eradicate Pseudomonas aeruginosa, a human pathogen.* Mol Syst Biol, 2011. **7**: p. 521.

60. Hong, S.H., et al., *Synthetic quorum-sensing circuit to control consortial biofilm formation and dispersal in a microfluidic device.* Nat Commun, 2012. **3**: p. 613.

61. Duan, F. and J.C. March, *Engineered bacterial communication prevents Vibrio cholerae virulence in an infant mouse model.* Proc Natl Acad Sci U S A, 2010. **107**(25): p. 11260-4.

62. Romero, P.A. and F.H. Arnold, *Exploring protein fitness landscapes by directed evolution.* Nat Rev Mol Cell Biol, 2009. **10**(12): p. 866-76.

63. Collins, C.H., J.R. Leadbetter, and F.H. Arnold, *Dual selection enhances the signaling specificity of a variant of the quorum-sensing transcriptional activator LuxR.* Nat Biotechnol, 2006. **24**(6): p. 708-12.

64. Kambam, P.K., et al., *Directed evolution of LuxI for enhanced OHHL production.* Biotechnol Bioeng, 2008. **101**(2): p. 263-72.

65. Gross, A., G. Rodel, and K. Ostermann, *Application of the yeast pheromone system for controlled cell-cell communication and signal amplification.* Lett Appl Microbiol, 2011. **52**(5): p. 521-6.

66. Bulter, T., et al., *Design of artificial cell-cell communication using gene and metabolic networks.* Proc Natl Acad Sci U S A, 2004. **101**(8): p. 2299-304.

67. Chen, M.T. and R. Weiss, *Artificial cell-cell communication in yeast Saccharomyces cerevisiae using signaling elements from Arabidopsis thaliana.* Nat Biotechnol, 2005. **23**(12): p. 1551-5.

68. Weber, W., et al., *Engineered Streptomyces quorum-sensing components enable inducible siRNA-mediated translation control in mammalian cells and adjustable transcription control in mice.* J Gene Med, 2005. **7**(4): p. 518-25.

69. Wang, W.D., et al., *Construction of an artificial intercellular communication network using the nitric oxide signaling elements in mammalian cells.* Exp Cell Res, 2008. **314**(4): p. 699-706.

70. Weber, W., et al., *A synthetic metabolite-based mammalian inter-cell signaling system.* Mol Biosyst, 2009. **5**(7): p. 757-63.

71. Bacchus, W., et al., *Synthetic two-way communication between mammalian cells.* Nat Biotechnol, 2012. **30**(10): p. 991-6.

72. Weber, W., M. Daoud-El Baba, and M. Fussenegger, *Synthetic ecosystems based on airborne inter- and intrakingdom communication.* Proc Natl Acad Sci U S A, 2007. **104**(25): p. 10435-40.

73. Tan, C., P. Marguet, and L. You, *Emergent bistability by a growth-modulating positive feedback circuit.* Nat Chem Biol, 2009. **5**(11): p. 842-8.

74. Marguet, P., et al., *Oscillations by minimal bacterial suicide circuits reveal hidden facets of host-circuit physiology.* PLoS One, 2010. **5**(7): p. e11909.

75. Elowitz, M.B., et al., *Stochastic gene expression in a single cell.* Science, 2002. **297**(5584): p. 1183-6.

76. Eldar, A. and M.B. Elowitz, *Functional roles for noise in genetic circuits.* Nature, 2010. **467**(7312): p. 167-73.

77. Munsky, B., G. Neuert, and A. van Oudenaarden, *Using gene expression noise to understand gene regulation.* Science, 2012. **336**(6078): p. 183-7.

78. Falkowski, P.G., T. Fenchel, and E.F. Delong, *The microbial engines that drive Earth's biogeochemical cycles.* Science, 2008. **320**(5879): p. 1034-9.

79. Strom, S.L., *Microbial ecology of ocean biogeochemistry: a community perspective.* Science, 2008. **320**(5879): p. 1043-5.

80. Muyzer, G. and A.J. Stams, *The ecology and biotechnology of sulphate-reducing bacteria.* Nat Rev Microbiol, 2008. **6**(6): p. 441-54.

81. Jia, W., et al., *Gut microbiota: a potential new territory for drug targeting.* Nat Rev Drug Discov, 2008. **7**(2): p. 123-9.

82. Dethlefsen, L., M. McFall-Ngai, and D.A. Relman, *An ecological and evolutionary perspective on human-microbe mutualism and disease.* Nature, 2007. **449**(7164): p. 811-8.

83. Brenner, K., L. You, and F.H. Arnold, *Engineering microbial consortia: a new frontier in synthetic biology.* Trends Biotechnol, 2008. **26**(9): p. 483-9.

84. Peet, R., *The measurement of species diversity.* Annual Review of Ecology and Systematics, 1974. **5**: p. 285-307.

85. Jessup, C.M., et al., *Big questions, small worlds: microbial model systems in ecology.* Trends Ecol Evol, 2004. **19**(4): p. 189-97.

86. Loreau, M., et al., *Biodiversity and ecosystem functioning: current knowledge and future challenges.* Science, 2001. **294**(5543): p. 804-8.

87. Ley, R.E., D.A. Peterson, and J.I. Gordon, *Ecological and evolutionary forces shaping microbial diversity in the human intestine.* Cell, 2006. **124**(4): p. 837-48.

88. Dykhuizen, D.E., *Santa Rosalia revisited: why are there so many species of bacteria?* Antonie Van Leeuwenhoek, 1998. **73**(1): p. 25-33.

89. Staley, J.T. and A.-L. Reysenbach, eds. *Biodiversity of Microbial Life: Foundation of Earth's Biosphere*. 2001, Wiley-Liss.

90. Ward, D.M., et al., *A natural view of microbial biodiversity within hot spring cyanobacterial mat communities.* Microbiol Mol Biol Rev, 1998. **62**(4): p. 1353-70.

91. Horner-Devine, M.C., K.M. Carney, and B.J. Bohannan, *An ecological perspective on bacterial biodiversity.* Proc Biol Sci, 2004. **271**(1535): p. 113-22.

92. Tilman, D., *The ecological consequences of changes in biodiversity: a search for general principles.* Ecology, 1999. **80**(5): p. 1455-1474.

93. Chesson, P. and J.J. Kuang, *The interaction between predation and competition.* Nature, 2008. **456**: p. 235-238.

94. Martin, M.O., *Predatory prokaryotes: an emerging research opportunity.* J Mol Microbiol Biotechnol, 2002. **4**(5): p. 467-77.

95. Jurkevitch, E., *Predatory behaviors in bacteria - diversity and transitions.* Microbe, 2007. **2**(2): p. 67-73.

96. Guerrero, R., et al., *Predatory prokaryotes: predation and primary consumption evolved in bacteria.* Proc Natl Acad Sci U S A, 1986. **83**: p. 2138-42.

97. Esteve, I., et al., *Comparison of techniques to determine the abundance of predatory bacteria attacking chromatiaceae.* FEMS Microbial Ecology, 1992. **86**: p. 205-211.

98. Lambert, C., et al., *Bdellovibrio: growth and development during the predatory cycle.* Curr Opin Microbiol, 2006. **9**(6): p. 639-44.

99. Reichenbach, T., M. Mobilia, and E. Frey, *Mobility promotes and jeopardizes biodiversity in rock-paper-scissors games.* Nature, 2007. **448**(7157): p. 1046-9.

100. Kerr, B., et al., *Local dispersal promotes biodiversity in a real-life game of rock-paper-scissors.* Nature, 2002. **418**(6894): p. 171-4.

101. Hart, B.A. and S.A. Zahler, *Lytic enzyme produced by Myxococcus xanthus.* J Bacteriol, 1966. **92**(6): p. 1632-7.

102. Berleman, J.E., et al., *Rippling is a predatory behavior in Myxococcus xanthus.* J Bacteriol, 2006. **188**(16): p. 5888-95.

103. Pham, V.D., et al., *Mutations affecting predation ability of the soil bacterium Myxococcus xanthus.* Microbiology, 2005. **151**(Pt 6): p. 1865-74.

104. Keller, L. and M.G. Surette, *Communication in bacteria: an ecological and evolutionary perspective.* Nat Rev Microbiol, 2006. **4**(4): p. 249-58.

105. Battin, T.J., et al., *Microbial landscapes: new paths to biofilm research.* Nat Rev Microbiol, 2007. **5**(1): p. 76-81.

106. Pohnert, G., M. Steinke, and R. Tollrian, *Chemical cues, defence metabolites and the shaping of pelagic interspecific interactions.* Trends Ecol Evol, 2007. **22**(4): p. 198-204.

107. Dicke, M. and M.W. Sabelis, *Infochemical terminology: based on cost-benefit analysis rather than origin of compounds?* Functional Ecology, 1988. **2**: p. 131-139.

108. Ianora, M., et al., *New trends in marine chemical ecology.* Estuaries and Coasts, 2006. **29**(4): p. 531-551.

109. Whittaker, R.H. and P.P. Feeny, *Allelochemicals: chemical interactions between species.* Science, 1971. **171**: p. 757-770.

110. Weissburg, M.J., et al., *Ecological consequences of chemically mediated prey perception.* J Chem Ecol, 2002. **28**(10): p. 1953-70.

111. Shiner, E.K., K.P. Rumbaugh, and S.C. Williams, *Inter-kingdom signaling: deciphering the language of acyl homoserine lactones.* FEMS Microbiol Rev, 2005. **29**(5): p. 935-47.

112. Tilman, D. and P. and Kareiva, *Spatial Ecology*1997, Princeton: Princeton University Press.

113. Rosenzweig, M.L., *Species Diversity in Space and Time*1995, Cambridge: Cambridge University Press.

114. Stolp, H., *Microbial Ecology: Organisms, habitats, activities*1988, Cambridge: Cambridge University Press.

115. Durrett, R. and S. Levin, *Spatial aspects of interspecific competition.* Theor Popul Biol, 1998. **53**(1): p. 30-43.

116. Hastings, A., *Spatial heterogeneity and the stability of predator-prey systems.* Theor Popul Biol, 1977. **12**(1): p. 37-48.

117. Sambrook, J. and D.W. Russell, *Molecular Cloning: A laboratory manual*. The third Edition ed2001: Cold Spring Harbor Laboratory Press.

118. Rasband, W.S., *ImageJ*, 1997-2008, U. S. National Institutes of Health, Bethesda, Maryland, USA, http://rsb.info.nih.gov/ij/.

119. Zeller, R., J. Lopez-Rios, and A. Zuniga, *Vertebrate limb bud development: moving towards integrative analysis of organogenesis.* Nat Rev Genet, 2009. **10**(12): p. 845-58.

120. Yu, M., et al., *The morphogenesis of feathers.* Nature, 2002. **420**(6913): p. 308-12.

121. Sick, S., et al., *WNT and DKK determine hair follicle spacing through a reaction-diffusion mechanism.* Science, 2006. **314**(5804): p. 1447-50.

122. Turing, A.M., *The Chemical Basis of Morphogenesis.* Philosophical Transactions of the Royal Society of London Series B-Biological Sciences, 1952. **237**(641): p. 37-72.

123. Hentschel, H.G., et al., *Dynamical mechanisms for skeletal pattern formation in the vertebrate limb.* Proc Biol Sci, 2004. **271**(1549): p. 1713-22.

124. Kiskowski, M.A., et al., *Interplay between activator-inhibitor coupling and cell-matrix adhesion in a cellular automaton model for chondrogenic patterning.* Dev Biol, 2004. **271**(2): p. 372-87.

125. Miura, T. and P.K. Maini, *Speed of pattern appearance in reaction-diffusion models: implications in the pattern formation of limb bud mesenchyme cells.* Bull Math Biol, 2004. **66**(4): p. 627-49.

126. Murray, J.D. and M.R. Myerscough, *Pigmentation pattern formation on snakes.* J Theor Biol, 1991. **149**(3): p. 339-60.

127. Nakamasu, A., et al., *Interactions between zebrafish pigment cells responsible for the generation of Turing patterns.* Proc Natl Acad Sci U S A, 2009. **106**(21): p. 8429-34.

128. Painter, K.J., P.K. Maini, and H.G. Othmer, *Stripe formation in juvenile Pomacanthus explained by a generalized turing mechanism with chemotaxis.* Proc Natl Acad Sci U S A, 1999. **96**(10): p. 5549-54.

129. Meinhardt, H., *Models of biological pattern formation: from elementary steps to the organization of embryonic axes.* Curr Top Dev Biol, 2008. **81**: p. 1-63.

130. Benazet, J.D., et al., *A self-regulatory system of interlinked signaling feedback loops controls mouse limb patterning.* Science, 2009. **323**(5917): p. 1050-3.

131. Towers, M., et al., *Integration of growth and specification in chick wing digit-patterning.* Nature, 2008. **452**(7189): p. 882-6.

132. Scherz, P.J., et al., *Extended exposure to Sonic hedgehog is required for patterning the posterior digits of the vertebrate limb.* Dev Biol, 2007. **308**(2): p. 343-54.

133. Kerszberg, M. and L. Wolpert, *Specifying positional information in the embryo: looking beyond morphogens.* Cell, 2007. **130**(2): p. 205-9.

134. Nagahara, H., et al., *Spatiotemporal pattern in somitogenesis: a non-Turing scenario with wave propagation.* Phys Rev E Stat Nonlin Soft Matter Phys, 2009. **80**(2 Pt 1): p. 021906.

135. Pourquie, O., *The segmentation clock: converting embryonic time into spatial pattern.* Science, 2003. **301**(5631): p. 328-30.

136. Sambrook, J. and D.W. Russell, *Molecular cloning : a laboratory manual*. 3rd ed2001, Cold Spring Harbor, N.Y.: Cold Spring Harbor Laboratory Press.

137. Kumar, A. and S.S. Patel, *Inhibition of T7 RNA polymerase: transcription initiation and transition from initiation to elongation are inhibited by T7 lysozyme via a ternary complex with RNA polymerase and promoter DNA.* Biochemistry, 1997. **36**(45): p. 13954-62.

138. Studier, F.W., *Use of bacteriophage T7 lysozyme to improve an inducible T7 expression system.* J Mol Biol, 1991. **219**(1): p. 37-44.

139. Buchler, N.E. and F.R. Cross, *Protein sequestration generates a flexible ultrasensitive response in a genetic network.* Mol Syst Biol, 2009. **5**: p. 272.

140. Jeruzalmi, D. and T.A. Steitz, *Structure of T7 RNA polymerase complexed to the transcriptional inhibitor T7 lysozyme.* EMBO J, 1998. **17**(14): p. 4101-13.

141. Wolpert, L., *Positional information and the spatial pattern of cellular differentiation.* J Theor Biol, 1969. **25**(1): p. 1-47.

142. Casal, J., G. Struhl, and P.A. Lawrence, *Developmental compartments and planar polarity in Drosophila.* Curr Biol, 2002. **12**(14): p. 1189-98.

143. Meinhardt, H. and A. Gierer, *Applications of a theory of biological pattern formation based on lateral inhibition.* J Cell Sci, 1974. **15**(2): p. 321-46.

144. Chisholm, R.H., B.D. Hughes, and K.A. Landman, *Building a morphogen gradient without diffusion in a growing tissue.* PLoS One, 2010. **5**(9).

145. Pfeiffer, S., et al., *The progeny of wingless-expressing cells deliver the signal at a distance in Drosophila embryos.* Curr Biol, 2000. **10**(6): p. 321-4.

146. Ibanes, M., et al., *Cell lineage transport: a mechanism for molecular gradient formation.* Mol Syst Biol, 2006. **2**: p. 57.

147. Verheyden, J.M. and X. Sun, *An Fgf/Gremlin inhibitory feedback loop triggers termination of limb bud outgrowth.* Nature, 2008. **454**(7204): p. 638-41.

148. Cooke, J. and E.C. Zeeman, *A clock and wavefront model for control of the number of repeated structures during animal morphogenesis.* J Theor Biol, 1976. **58**(2): p. 455-76.

149. Ferreira, S.C., Jr., M.L. Martins, and M.J. Vilela, *Reaction-diffusion model for the growth of avascular tumor.* Phys Rev E Stat Nonlin Soft Matter Phys, 2002. **65**(2 Pt 1): p. 021907.

150. Mallet, D.G. and L.G. De Pillis, *A cellular automata model of tumor-immune system interactions.* J Theor Biol, 2006. **239**(3): p. 334-50.

151. Morse, R.P., et al., *Structural basis of toxicity and immunity in contact-dependent growth inhibition (CDI) systems.* Proc Natl Acad Sci U S A, 2012. **109**(52): p. 21480-5.

152. Jozefczuk, S., et al., *Metabolomic and transcriptomic stress response of Escherichia coli.* Mol Syst Biol, 2010. **6**: p. 364.

153. Klumpp, S., Z. Zhang, and T. Hwa, *Growth rate-dependent global effects on gene expression in bacteria.* Cell, 2009. **139**(7): p. 1366-75.

154. Scott, M., et al., *Interdependence of cell growth and gene expression: origins and consequences.* Science, 2010. **330**(6007): p. 1099-102.

155. Mcmichael, J.C., *Bacterial Differentiation within Moraxella-Bovis Colonies Growing at the Interface of the Agar Medium with the Petri Dish.* Journal of General Microbiology, 1992. **138**: p. 2687-2695.

156. Sohka, T., et al., *An externally tunable bacterial band-pass filter.* Proc Natl Acad Sci U S A, 2009. **106**(25): p. 10135-40.

157. Koch, A.J. and H. Meinhardt, *Biological Pattern-Formation - from Basic Mechanisms to Complex Structures.* Reviews of Modern Physics, 1994. **66**(4): p. 1481-1507.

158. Rogers, K.W. and A.F. Schier, *Morphogen gradients: from generation to interpretation.* Annu Rev Cell Dev Biol, 2011. **27**: p. 377-407.

159. Maini, P.K., R.E. Baker, and C.M. Chuong, *Developmental biology. The Turing model comes of molecular age.* Science, 2006. **314**(5804): p. 1397-8.

160. Smith, J., C. Theodoris, and E.H. Davidson, *A gene regulatory network subcircuit drives a dynamic pattern of gene expression.* Science, 2007. **318**(5851): p. 794-7.

161. Bosveld, F., et al., *Mechanical control of morphogenesis by Fat/Dachsous/Four-jointed planar cell polarity pathway.* Science, 2012. **336**(6082): p. 724-7.

162. Asally, M., et al., *Localized cell death focuses mechanical forces during 3D patterning in a biofilm.* Proc Natl Acad Sci U S A, 2012. **109**(46): p. 18891-6.

163. Gibson, W.T., et al., *Control of the mitotic cleavage plane by local epithelial topology.* Cell, 2011. **144**(3): p. 427-38.

164. Chen, H., et al., *A system of repressor gradients spatially organizes the boundaries of Bicoid-dependent target genes.* Cell, 2012. **149**(3): p. 618-29.

165. Roth, S. and J. Lynch, *Does the Bicoid Gradient Matter?* Cell, 2012. **149**(3): p. 511-512.

166. Lander, A.D., et al., *Cell lineages and the logic of proliferative control.* PLoS Biol, 2009. **7**(1): p. e15.

167. Bullough, W.S., *The control of mitotic activity in adult mammalian tissues.* Biol Rev Camb Philos Soc, 1962. **37**: p. 307-42.

168. Gamer, L.W., J. Nove, and V. Rosen, *Return of the chalones.* Developmental cell, 2003. **4**(2): p. 143-4.

169. Wang, C.L., et al., *Metabolic engineering of an aerobic sulfate reduction pathway and its application to precipitation of cadmium on the cell surface.* Appl Environ Microbiol, 2000. **66**(10): p. 4497-502.

170. Wang, C.L., D.S. Clark, and J.D. Keasling, *Analysis of an engineered sulfate reduction pathway and cadmium precipitation on the cell surface.* Biotechnol Bioeng, 2001. **75**(3): p. 285-91.

171. Wang, C.L., et al., *Aerobic sulfide production and cadmium precipitation by Escherichia coli expressing the Treponema denticola cysteine desulfhydrase gene.* Appl Microbiol Biotechnol, 2001. **56**(3-4): p. 425-30.

172. Pandian, S.R., et al., *Biologically synthesized fluorescent CdS NPs encapsulated by PHB.* Enzyme Microb Technol, 2011. **48**(4-5): p. 319-25.

173. Mi, C., et al., *Biosynthesis and characterization of CdS quantum dots in genetically engineered Escherichia coli.* J Biotechnol, 2011. **153**(3-4): p. 125-32.

174. Nakamura, M., et al., *Biocompatible inkjet printing technique for designed seeding of individual living cells.* Tissue Eng, 2005. **11**(11-12): p. 1658-66.

175. Merrin, J., S. Leibler, and J.S. Chuang, *Printing multistrain bacterial patterns with a piezoelectric inkjet printer.* PLoS One, 2007. **2**(7): p. e663.

176. Pepper, M.E., et al., *Design and implementation of a two-dimensional inkjet bioprinter.* Conf Proc IEEE Eng Med Biol Soc, 2009. **2009**: p. 6001-5.

177. Cohen, D.J., R.C. Morfino, and M.M. Maharbiz, *A modified consumer inkjet for spatiotemporal control of gene expression.* PLoS One, 2009. **4**(9): p. e7086.

Biography

Stephen Thomas Payne was born in Pittsburgh, Pennsylvania on April 1, 1986 to William and Natalie Payne. He was an inquisitive child, who enjoyed playing hockey, was a movie enthusiastic, and loved watching the hometown Penguins and Steelers. After graduating from Fox Chapel Area High School in Pittsburgh, he attended the Massachusetts Institute of Technology. There, he was a part of the Institute's inaugural biological engineering graduating class in June of 2008 and was a proud member of the Institute's Varsity Ice Hockey team. He spent his first summer at MIT at the Registry of Standard Biological Parts and became an eager disciple of computer-scientist-turned-synthetic-biologist Tom Knight and synthetic biology leader Drew Endy. Stephen went on to excel as a member of MIT's 2006 iGEM team, which won the First Place award for 'Best System' and the Third Place award for 'Best Presentation' among 40 teams from around the world for reengineering E. coli to smell like banana and wintergreen. Stephen went on to attend Duke University's PhD program in the Department of Biomedical Engineering in the fall of 2008. His interest in synthetic biology led him to pursue his degree as a member of Lingchong You's lab. There, when he was not playing hockey for the Varsity Ice Hockey team, he spent most of his time genetically engineering bacteria to form self-organized patterns in space, culminating in the paper "Temporal control of self-organized pattern formation without morphogen gradients in engineered bacteria." For a complete list of publications and honors, see below:

Papers

Payne S, Li B, Schaeffer D, You L. "Temporal control of self-organized pattern formation without morphogen gradients in engineered bacteria." Manuscript under review in *Molecular Systems Biology*, April 2013.

Song H, **Payne S**, Gray M, You L (2009). "Spatiotemporal modulation of biodiversity in a synthetic chemical-mediated ecosystem." *Nature Chemical Biology* **5**(12): 929-935.

McCunney RJ, Morfeld P, **Payne S** (2009). "What component of coal causes Coal Workers' Pneumoconiosis? *J. Occup. Environ. Med.* **51**(4): 462-471.

Reviews

Song H, **Payne S**, Tan C, You L (2011). "Programming microbial population dynamics by engineered cell-cell communication." *Biotechnology Journal* **6**(7): 837-849.

Book Chapters

Payne S, You L. "Engineered cell-cell communication and its applications." *Productive Biofilms*. Ed. K Muffler and R Ulber. *Advances in Biochemical Engineering/Biotechnology*. Manuscript submitted for publication, February 2013.

Payne S, Smith RP, You L. "Quantitative analysis of the spatiotemporal dynamics of a synthetic predator-prey ecosystem." *Synthetic Gene Networks*. Ed. W Weber and M Fussenegger. *Methods in Molecular Biology.* (New York: Humana Press, 2012). Vol. 813, Part 4, p. 315-330.

Honors

Department of Homeland Security Graduate Fellowship, September 2009- August 2012.

Kewaunee Event 2012 Poster Award, April 19, 2012.

Biomedical Engineering Departmental Award for Excellence as a Teaching Assistant, May 2009.

NIH Center for Biomolecular and Tissue Engineering Fellowship, September 2008- August 2009.